2018

Circulation in the Lau Basin and Havre Trough

Elizabeth Gabrielle Simons

FLORIDA STATE UNIVERSITY

COLLEGE OF ARTS AND SCIENCES

CIRCULATION IN THE LAU BASIN AND HAVRE TROUGH

By

ELIZABETH G. SIMONS

A Dissertation submitted to the
Geophysical Fluid Dynamics Institute
in partial fulfillment of the
requirements for the degree of
Doctor of Philosophy

2018

Elizabeth G. Simons defended this dissertation on March 30, 2018.
The members of the supervisory committee were:

Kevin Speer

Professor Directing Dissertation

Nick Cogan

University Representative

Bill Dewar

Committee Member

Philip Sura

Committee Member

The Graduate School has verified and approved the above-named committee members, and certifies that the dissertation has been approved in accordance with university requirements.

To my mom, Florence Cohen Simons, one of the smartest people I'll ever know.

ACKNOWLEDGMENTS

I would like to acknowledge the support of CCS-2 and CNLS at Los Alamos National Laboratories during the course of this project. I would also like to acknowledge several individuals who have helped me both morally and scientifically over the course of my graduate career: my spouse, Joe; Dr. Ruby Krishnamurti, who provided countless cups of coffee and absolutely astounding conversation; my dad, Larry; and of course my advisor, Kevin Speer who put up with a lot from me.

TABLE OF CONTENTS

LIST OF FIGURES

ABSTRACT

The ridge systems that frame the Lau Basin and Havre Trough, located east of Fiji and north of New Zealand, separating a large counterclockwise gyre at the surface into two smaller gyres at depth. A strong deep western boundary current (DWBC) has been observed flowing northward, following the Tonga and Kermadec Trench systems, transporting bottom water to the North Pacific. Though circulation has been described to some degree around the Lau Basin and the Havre Trough, these sub-basins have largely been ignored, presumed to act as a barrier to flow and separating the western South Pacific from the eastern South Pacific. An analysis of float data from several sources as well as traditional ship-board hydrographic data reveal a DWBC within the Lau Basin and Havre Trough that is fed by westward flowing jets from breaks within the ridge system. A simple analytical model predicts the large-scale dynamics observed in the basin, and indicates that the topographic structure of the ridge modulates the flow patterns. Sources of water into the Lau Basin and Havre Trough indicate intermediate water sources from the eastern South Pacific, while deep water sources originate to the west. This leads to a revised view of the role of the Lau Basin and Havre Trough with respect to circulation in the South Pacific

CHAPTER 1

INTRODUCTION TO CIRCULATION IN THE SOUTH PACIFIC OCEAN

Large scale circulation in the South Pacific Ocean is dominated by a large anticyclonic gyre and several western boundary currents. This was first clearly illustrated in Reid (1986), using available hydrographic data to calculate geostrophic velocities for the entirety of the South Pacific (Figure 1.1). Though there was extremely limited data, due to the large expanse of the South Pacific making traditional hydrographic data gathering expensive and inefficient, a strong picture of circulation emerged. Subsequent studies using float data [**?**, Davis, 2005] have agreed within reason with the large scale circulation patterns outlined by Reid's work.

Below the upper 500m of the water column differences between the float data and the traditional hydrographic data become noticeable. Some of the differences with Reid's basin wide picture are highlighted in Gray & Riser (2014) particularly below 1000db (Figure 1.2 and 1.3). Two distinct anticyclonic gyres appear in the South Pacific. The main, large gyre situated east of New Zealand is the same, but there is a smaller gyre that gets 'pinched' off of the main feature at that depth and is squashed into a smaller region bordered on the west by New Zealand and the east by the southern edge of continental Australia and Tasmania.

There are several surface and upper column western boundary currents found within in the South Pacific. Some of these are the southward flowing East Australian Current (EAC), that separates from the coast around 30∘S forming the Tasman Front. The Tasman Front is an eddy filled, jet-like structure that moves east to join with the northern tip of the north island of New Zealand. Once attached to the north island this becomes the East Auckland Current (EAUC), a short, southward flowing western boundary current confined to the north island. The EAUC then flows around Chatham Rise and either rejoins the Antarctic Circum-

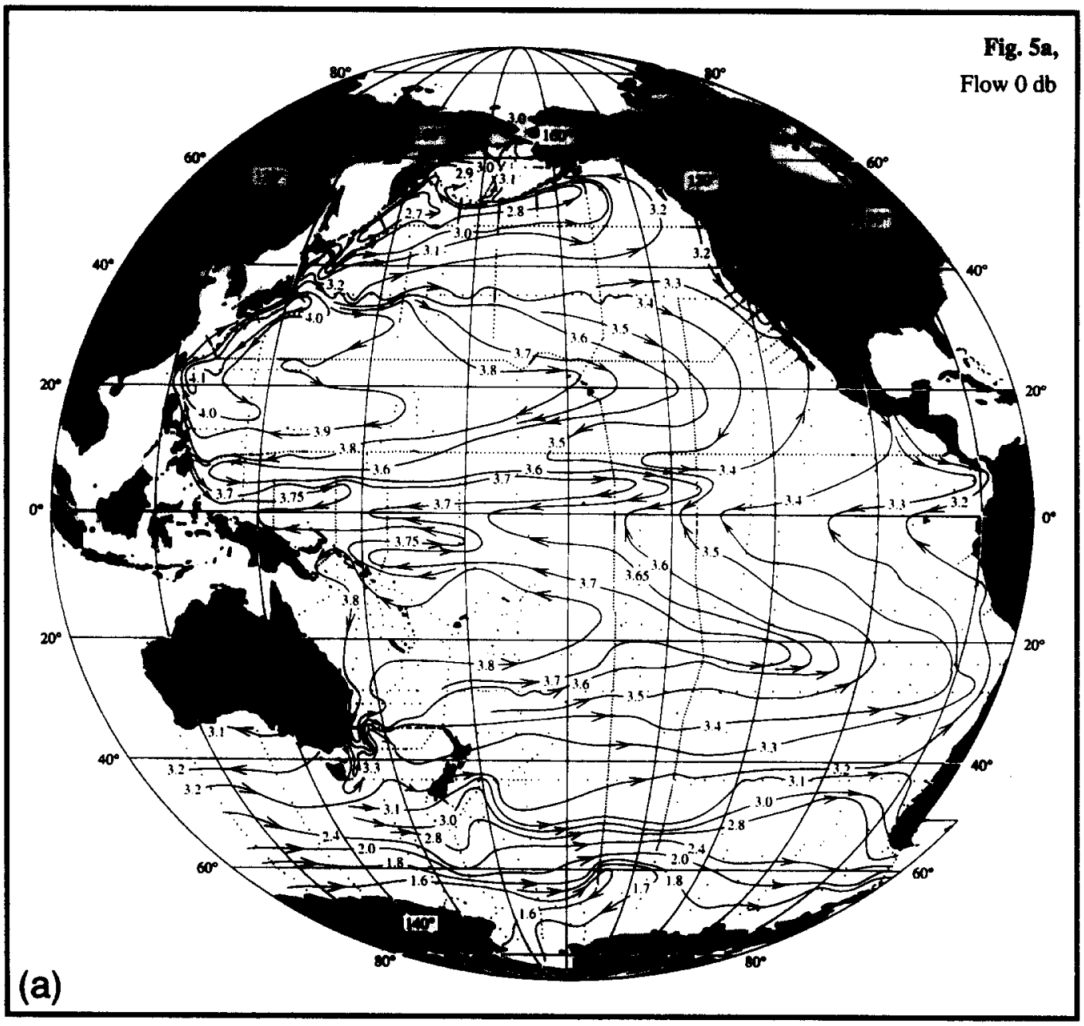

Fig. 5. (a) Adjusted steric height at 0 db (10 m^2s^{-2} or 10 Jkg^{-1}).

Figure 1.1: Upper water circulation patterns for the Pacific Ocean, north and south. Below the equator note the basin wide, counterclockwise rotation with a boundary along Australia. From Reid (1986), original caption included.

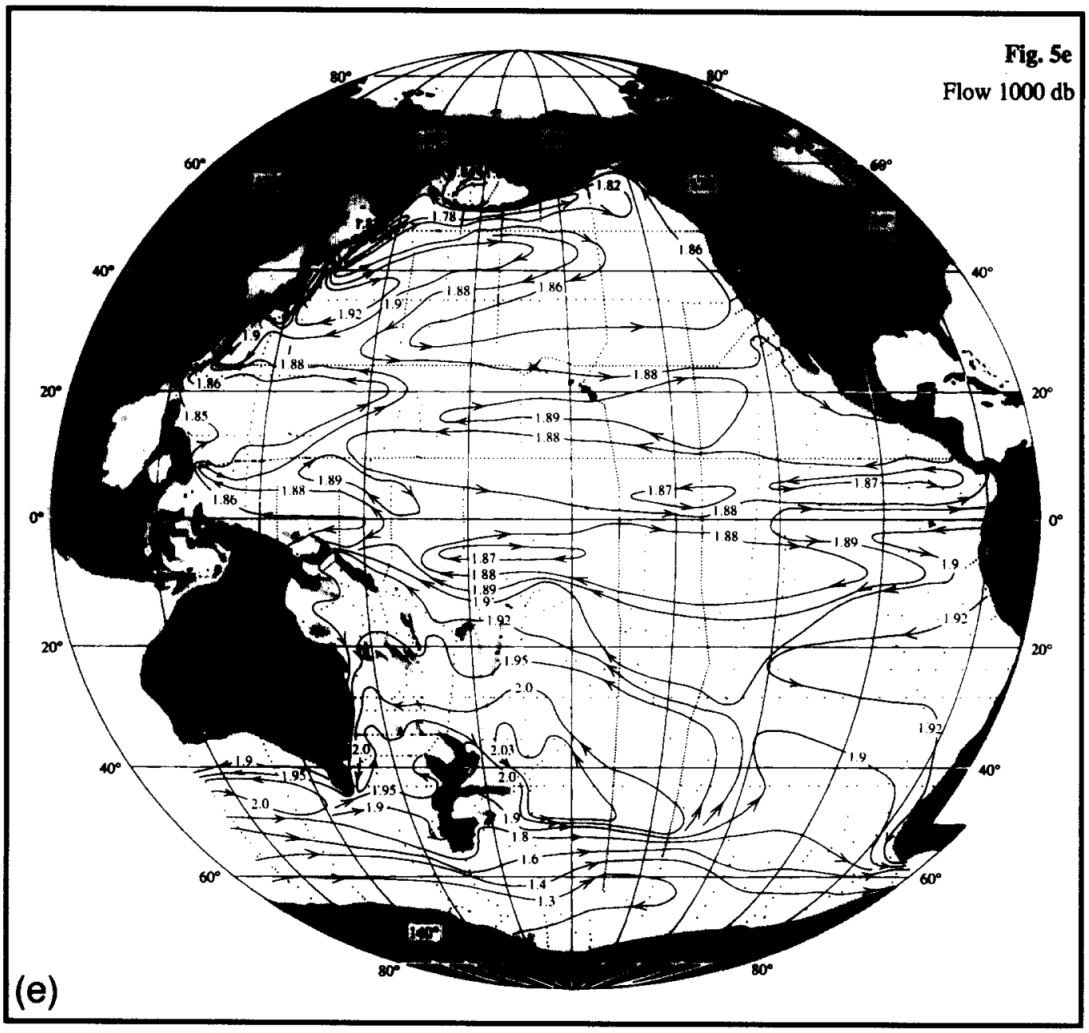

Fig. 5. (e), Adjusted steric height at 1000 db (10 m^2s^{-2} or 10 Jkg^{-1}). Depths less than 1000 m are shaded.

Figure 1.2: Circulation patterns for the Pacific Ocean at 1000db. Note that the gyre is located further south and is being blocked by more toporaphic features. From Reid (1986), original caption included.

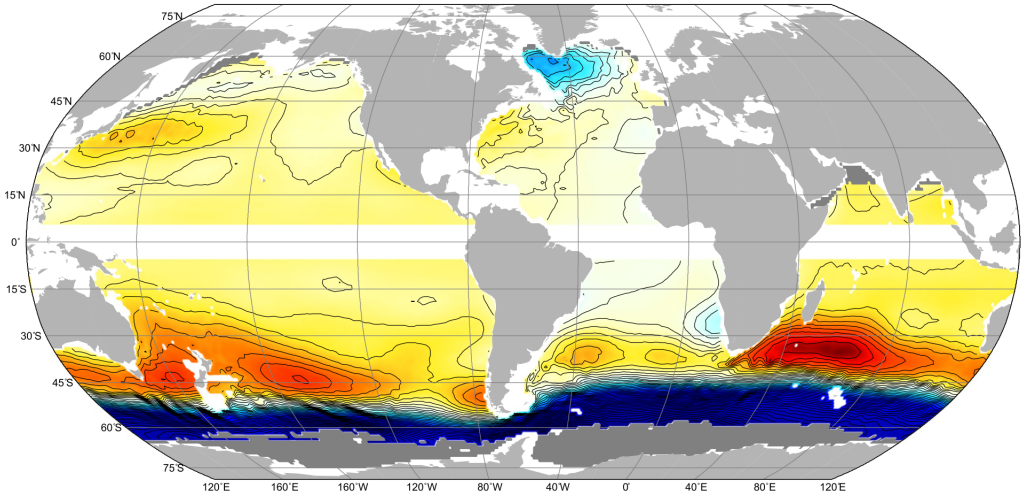

FIG. 4. Mean absolute geostrophic streamfunction at 1000 db from Argo data for December 2004–November 2010. Contour interval is 5 dyn cm. Colors as in Fig. 2.

Figure 1.3: Global circulation derived from float data at 1000db. Observe the two small gyres centered around 45°S in the Pacific, divided by New Zealand. From Gray and Riser (2014), original caption included.

polar Current or the South Pacific Gyre. During the Southwest Pacific Ocean Circulation and Climate Experiment (SPICE) the extent of the western South Pacific between Australia and New Zealand was extensively covered. This included the effects of the South Pacific Convergence Zone (SPCZ) on the Coral, Solomon and Tasman Seas, and the small boundary currents found around the Solomon Islands and Papua New Guinea [Ganachaud et al., 2014].

Of particular note in the central South Pacific, is the Deep Western Boundary Current (DWBC) which flows northward along the Tonga and Kermadec Trench. The theory of abyssal circulation put forward by Stommel included a schematic map of circulation (Figure 1.4), which predicted a northward flowing DWBC along New Zealand that extended well into the North Pacific. This current was first properly described by Reid et al (1968) [Reid et al., 1968], using the principals set forth in Stommel and Arons (1958) and hydrographic data gathered during the SCORPIO project. It has been found that this DWBC is the principal supply line of deep, Antarctic origin water into the rest of the Pacific Ocean as

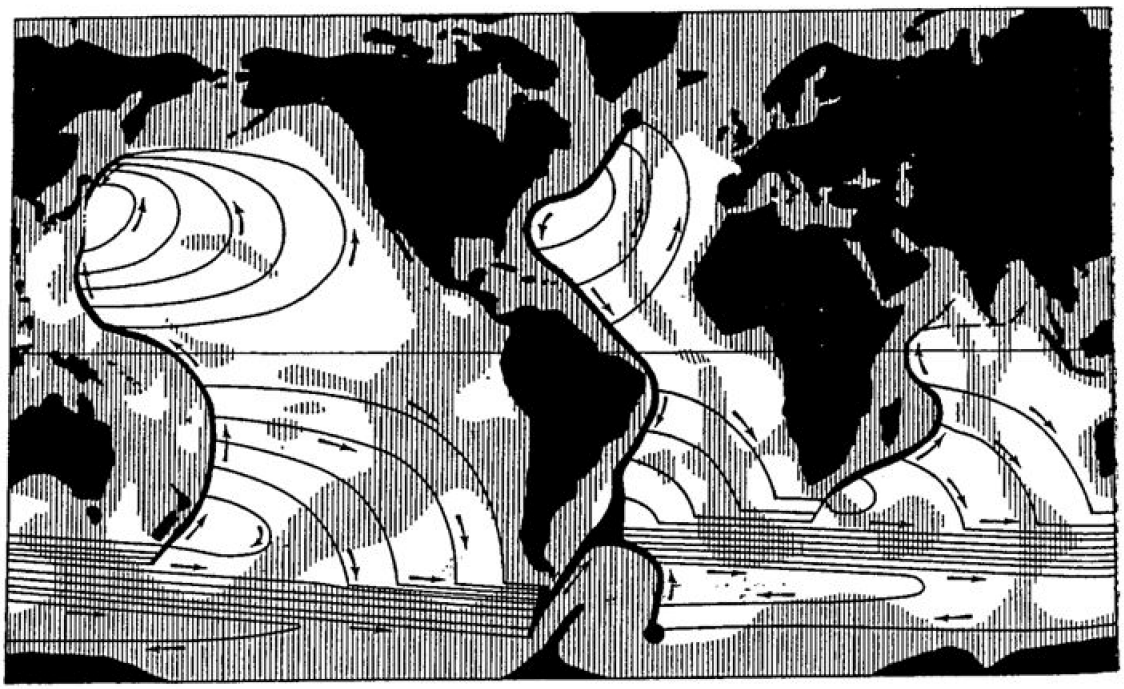

Figure 1.4: Schematic of global abyssal circulation as proposed by Stommel (1958).

was proposed by Warren (1976).

The DWBC has been found to flow northward below 2000m along the Tonga and Kermadec Ridges, after making its way around the Chatham Rise, with transport estimates ranging from 13-22Sv (1 Sverdrup = $10^6 \frac{m^3}{s}$) [Whitworth III et al., 1999, Warren, 1976] at the southern measurements points. Further north along the DWBC path, transport estimates decrease to 10-16 Sv [Banks et al., 1995] and the DWBC resides deeper in the water column (3000m). This is partly due to the effect of the South Pacific gyre's western arm reaching toward the Tonga Ridge. The longitudinal extent of the DWBC doesn't vary greatly during its journey through the South Pacific, remaining around 100km wide.

Water properties from smaller campaigns around the South Pacific have also contributed to the discussion of circulation in the South Pacific. With some knowledge of the topography in the area several pathways, not necessarily captured in large hydrographic averages, have

been proposed. There are Antarctic origin deep water properties found in the New Hebrides Trench and South Fiji Basin, but the Tasman Basin closes off direct communication with the south due to a sill depth too shallow for deep water penetration [Warren, 1976]. Wyrtki (1961) , postulated that the source was water renewal from the central Pacific and DWBC through pathways to the north of the basins (through the Vitiaz Trench, north of the Lau Basin).

Throughout these traditional studies the Lau Basin and Havre Trough, located east of Fiji and north of New Zealand, have all but been ignored. The ridge systems which frame these sub-basins have been considered an impediment to flow between the western South Pacific and the eastern South Pacific leaving an idea of circulation like that descibed above (Figure 1.5). This changed slightly due to a set of coordinated interdisciplinary experiments during the Ridge 2000 program [Tivey et al., 2012]. The Lau Basin was selected as one of the Integrated Study Sites in part due to its unique geologic features. The Lau Basin and Havre Trough are a classic back-arc basin located in the South Pacific 'ring of fire'. This is an area of intense hydrothermal and geologic activity resulting in a large number of earthquakes, hydrothermal vents and volcanic activity. Within the Lau Basin, a series of floats were released to study the circulation in the area [Speer and Thurnherr, 2012], resulting in the first dataset analyzed in this project.

We endeavor to contribute to the picture of circulation in the South Pacific by investigating the relationship the Lau Basin and Havre Trough have to communication between the eastern South Pacific and western South Pacific. In Chapter 2: Abyssal Circulation in the Lau Basin and Havre Trough, float data from the Ridge 2000 project, Argo floats and traditional ship-board hydrographic data are used to determine the circulation in the sub-basins. A simple analytical model is proposed, which captures some of the dynamics observed in the Lau Basin and Havre Trough. Chapter 3 expands on the analytical model, investigating the effects of topography. This requires the use of a spectral elements based numerical model with idealized topography. In Chapter 4, the role of the ridges and passages are explored in

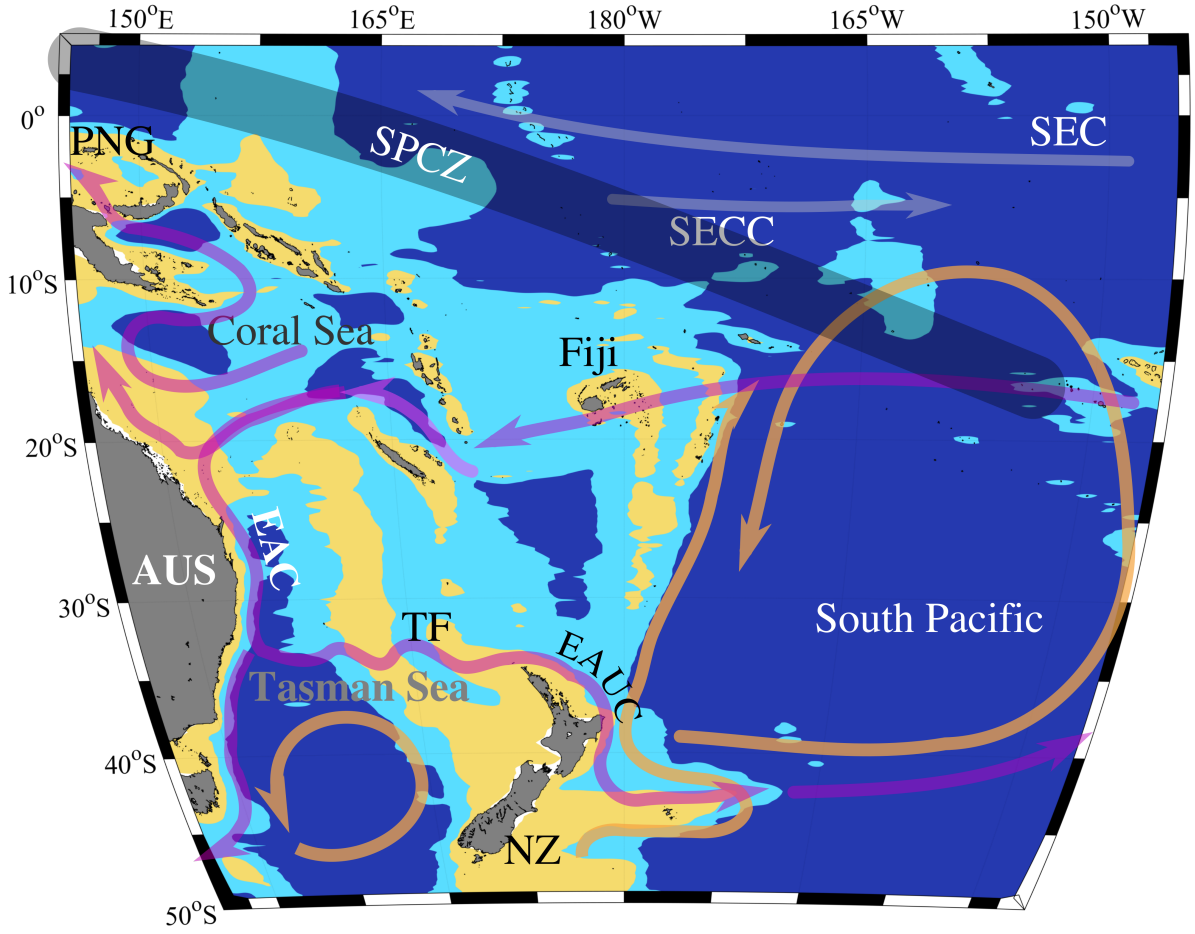

Figure 1.5: Schematic of the circulation in the South Pacific using data provided from literature. Purple lines indicate the upper 1000m of the water column, yellow is observed circulation below 1000m.

the import and export of the waters found within the Lau Basin and Havre Trough. Sources for the intermediate waters and deep waters are proposed. Chapter 5 summarizes the findings and proposes future work based on questions that arose throughout the course of this work.

CHAPTER 2

ABYSSAL CIRCULATION IN THE LAU BASIN AND HAVRE TROUGH

2.1 Introduction

The ridge system between New Zealand, Fiji, and Tonga (Figure 4.1) acts as the western boundary of the deep Southwest Pacific Basin, and is the location of a major deep current bringing bottom water and Circumpolar Deep Water (CDW) into the Pacific Ocean (Whitworth et al, 1999). These ridges form the barrier preventing a direct connection among the several basins of the western South Pacific Ocean and the interior South Pacific, leaving the South Fiji Basin an apparent cul-de-sac for the second major route of deep inflow, along the eastern margin of Australia. The basins within this ridge system, generally ignored as significant components of the deep circulation, are nevertheless well known in the geophysical community as active spreading centers hosting numerous hydrothermal vents, with tectonic and volcanic activity [Tivey et al., 2012, Sutton et al., 2012].

The Lau Basin is a back-arc basin with two active spreading centers located along the center of the basin. The Central Lau Spreading Center (CLSC) located at 17.5°S -19.5°S, and, along the eastern side of the basin, the Eastern Lau Spreading Center (ELSC) at 19.5°S - 23°S. The Tonga and Kermadec Ridges are attached to the active arc segment (still spreading) and the Lau and Colville Ridges are attached to the remnant arc (no longer spreading).

The hinged appearance of the Lau Basin is due to uneven motion from the spreading centers. The two spreading centers, the ELSC and the CLSC, run meridionally through the Lau Basin, but the CLSC opened after the ELSC and overlaps with the northern portion of

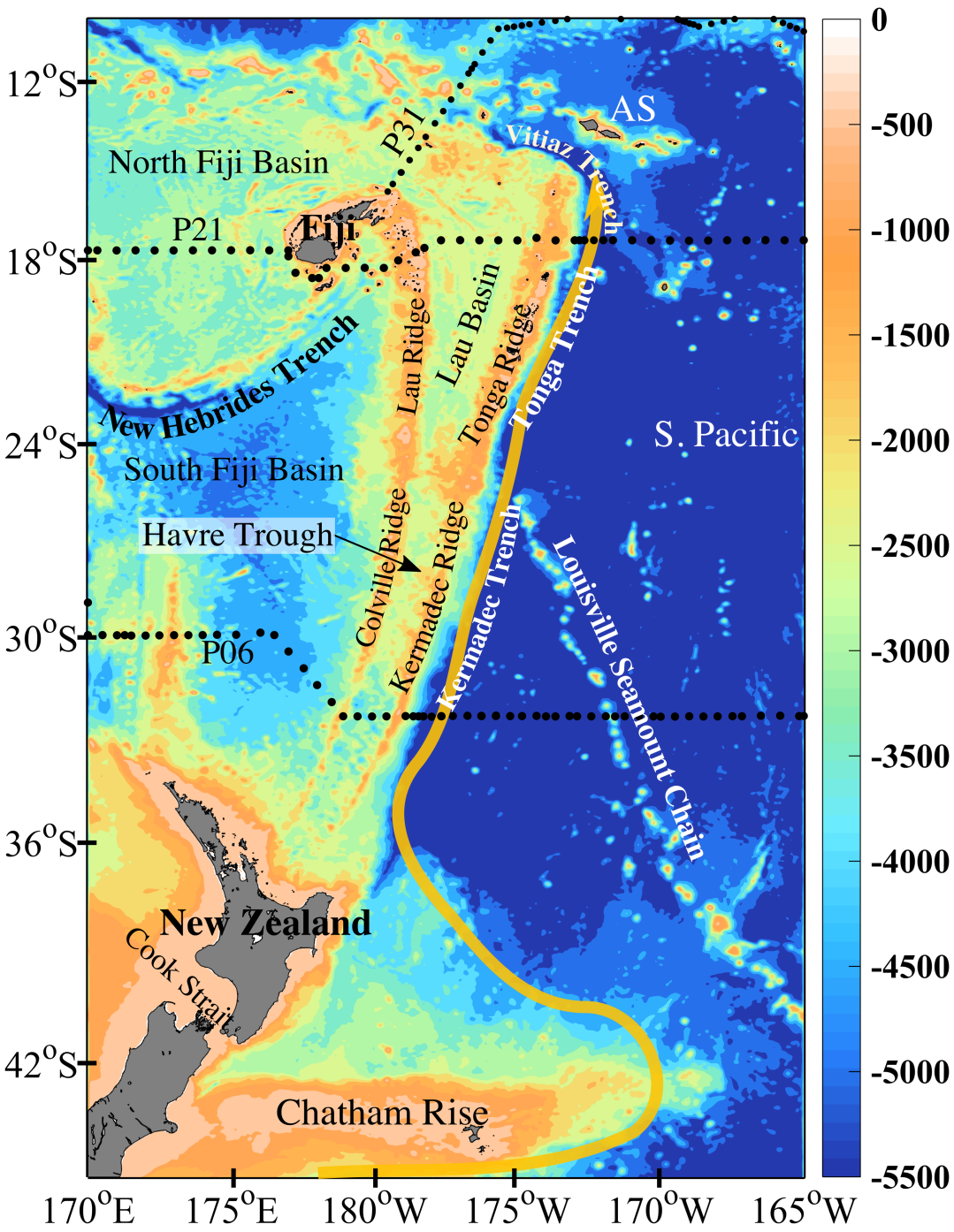

Figure 2.1: Lau Basin region. Hydrographic stations (black dots) and the DWBC path (yellow curve) are shown. AS = America Samoa.

the ELSC.

The Lau Basin is bordered on the west by the Lau Ridge and the east by the Tonga Ridge (Figure 4.1). A southern extension of the basin, called the Havre Trough, is separated from the Lau Basin by a wide sill about 2000m deep near 24 S, and is bounded by the Colville Ridge and Kermadec Ridge. The Havre Trough ends at the intersection with New Zealand. Within the Havre Trough two smaller basins are centered near 28°S and 33°S respectively. The northern boundary of the Lau Basin consists of a series of complicated shoals, and small volcanic islands.

The ridges that form the meridional walls of the Lau Basin and Havre Trough are gappy, uneven boundaries (Figure 2.2). The Tonga Ridge has multiple ridge breaks with the deepest ridge breaks at the Tofua Passage (1900m), and the Tonga Passage (2200m). The Tonga Passage is also the widest (meridional) passage along the Tonga Ridge, spanning about 200km. Along the northern portion of the Kermadec Ridge, a set of three shallower openings occur at the Kermadec Passage (1500m). Sills gradually deepen to the south, reaching a depth of 2400m at the base of the New Zealand continent.

At the northern end of the Lau Ridge is the North Fiji Passage (2200m; Figure 4.1). The ridge remains relatively shallow (above 750m depth) throughout the Lau Basin. Farther south, along the Colville Ridge bordering the Havre Trough, the sill depths increase. The Colville Passage, near 29°S with depths of 2000-2200 m is also relatively wide, about 80km at 1500m depth. It marks the start of a series of deeper passages leading up to an unnamed opening located near 32°S; this latter passage appears to be the deepest passage across the Colville Ridge, at 2500m depth. South of this passage, the various sills are shallower, up to the base of the New Zealand continental margin at depths close to 2000m.

The Kermadec Ridge and Tonga Ridge thus form a porous western boundary for the primary deep water inflow to the Pacific Ocean. This inflow, the Deep Western Boundary

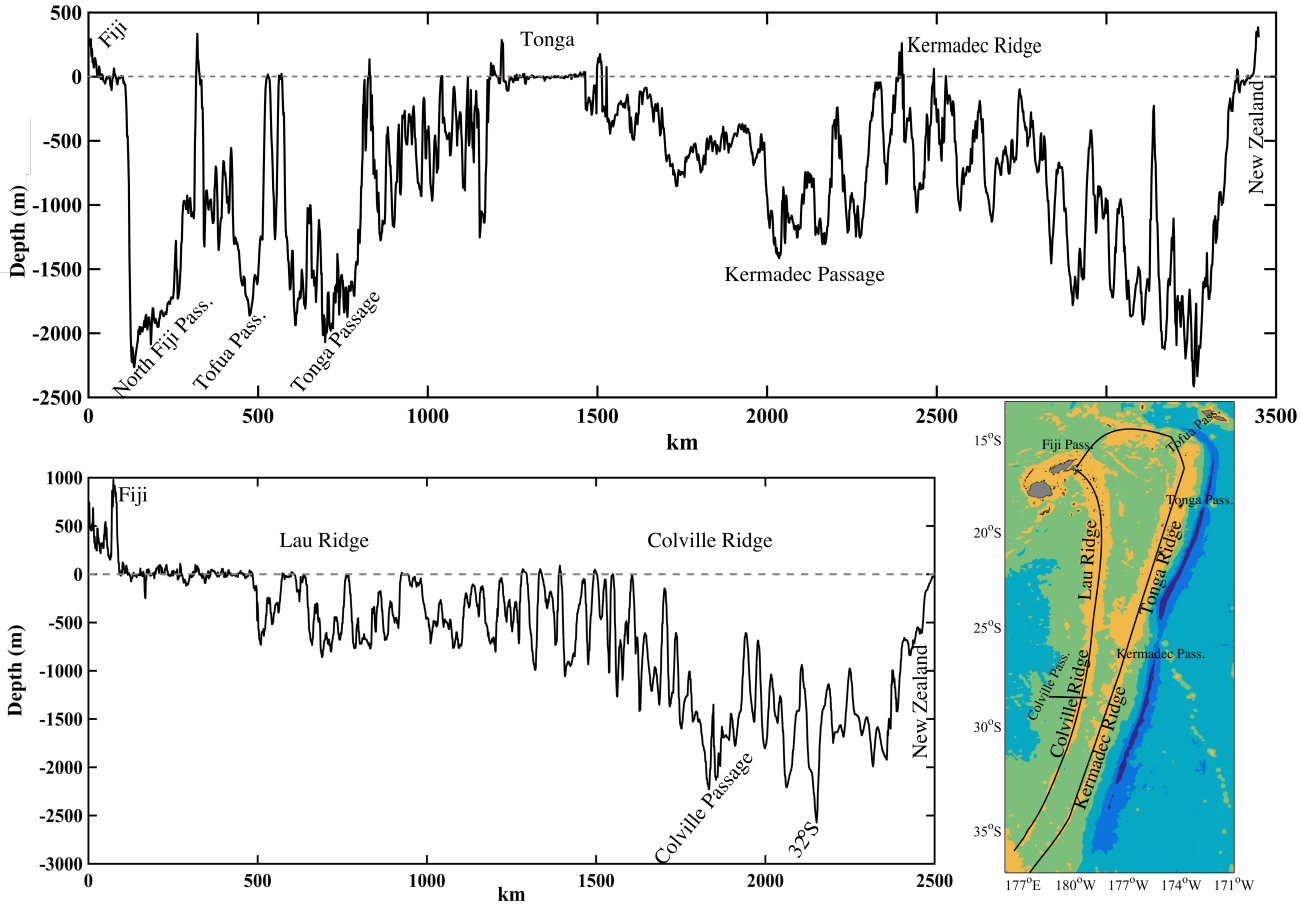

Figure 2.2: Sill depth along the Tonga and Kermadec Ridges. A) Sill depth starting at Fiji and ending at the northern island of New Zealand (meters). Passages are listed below, geographic reference points are listed above. B) Sill depth for the Lau and Colville Ridges starting on the southern side of Fiji. Passages are listed below, geographic references are listed above. C) Regional map of the area with the average path where the sill depth was taken (black line).

Current (DWBC), transports about 16 Sverdrups (1Sv = 10^6m/s) north, of which up to 6 Sv could be carried at depths less than 3250m [Whitworth III et al., 1999]. The upper reaches of the DWBC can potentially supply bottom water to the Havre Trough And South Fiji Basin through the passage at the intersection of the Kermadec Ridge and New Zealand and to the Lau Basin through the Tonga Passage. Warren et al. (1994) noted the possibility of the former but thought that any flow continued to the South Fiji Basin. They estimated a 0.2 Sv flow of Circumpolar Deep Water from the DWBC in the potential temperature range 2-2.2°C, lying above a sill of less than 2500m depth.

Several areas of recirculation are present in the Lau Basin and Havre Trough. The overall structure of the circulation is revealed by float measurements near 1700m depth and near 1000m depth, along with hydrography. As discussed below, deep water both enters and leaves the Lau Basin through the North Fiji Passage, and exits the Havre Trough at depths above the ridge crest primarily through the Colville Passage. The former supplies deep water modified by recirculation in the Lau Basin to the North Fiji Basin while the latter provides a major source at mid-depth to the South Fiji Basin. Moreover, the source of Bottom Water to the Havre Trough is found to be the South Fiji Basin, confirming an old suspicion of Wyrtki (1960).

Observations, old and new, show an unexpectedly rich boundary current system in the Lau Basin and Havre Trough. A simple model is developed to explain some of the boundary current structure, and expected and observed transports in the boundary currents are compared.

2.2 Observations

2.2.1 Lau Basin Float Experiment(LAUBFLEX)

As part of the Ridge 2000 Integrated Study Site [Fornari et al., 2012, Tivey et al., 2012] program in the Lau Basin, eleven APEX and PROVOR floats were deployed starting in mid-April of 2004, with the last deployment in June of 2005. The deployments were concentrated

in the NE and central Lau region [Speer and Thurnherr, 2012] to study circulation around an active spreading center and hydrothermal vents. Data was reported through March 2011. The floats were equipped to measure temperature and pressure, and to maintain a nominal 1700m drift depth. The cycle for a Lau Basin Float Experiment (LAUBFLEX) float consists of a drift period of $\sim$ 21 days at depth, returning to the surface (about 6 hours) to transmit data (about 12 hours) before returning to drift depth. Each of these floats measure temperature only in the water column while ascending to the surface. On average, during each 21 day cycle, the float spends 36 hours away from the target drift depth.

2.2.2 Argo Floats

The majority of Argo floats drift at a nominal depth of 1000m, and profile the water column vertically from 2000m to the surface. The typical float cycle for an Argo float is 10 days long with 9 days spent at drift depth before ascending to the surface to transmit data [Ollitrault and Rannou, 2013]. Floats transmit their data through either ARGOS systems or through Iridium systems. The ARGOS transmission requires a longer surface stay to transmit all the data (up to 12 hours), while Iridium can be as little as 30 minutes of transmission time.

Argo floats measure temperature, salinity, and pressure in the upper 2000m. The accuracy of these measurements is monitored and documented [Boyer et al., 2013], with temperature measurements typically accurate to ± 0.002°C, and salinity for real-time (minimal and automated quality control) data accurate to ± 0.01psu - ± 0.005psu dependent on the sensor, while delayed-time (sensor drift is removed and advanced quality control) data has a range from ± 0.005psu to ± 0.001psu dependent on the data flag [Boyer et al., 2013].

Within the Lau Basin, 152 distinct Argo floats, sourced from the Coriolis GDAC at the French Research Institute for Exploitation of the Sea (IFREMER), France (www.coriolis.eu.org), have passed through the region over 14 years from July 2001 to June 2015. The floats used

within this study were primarily APEX floats ($\sim$ 54%) and SOLO ($\sim$ 44%) with PROVOR floats making up the difference, see Ollitrault and Rannou (2013) for a full discussion of the float types and differences. The majority of floats used the Argos positioning system through 2005 [Ollitrault and Rannou, 2013], and after that the Iridium positioning system.

2.2.3 Argo and LAUBFLEX Float Processing

Following Ollitrault and Rannou [Ollitrault and Rannou, 2013], a representative park pressure (RPP) was assigned to each cycle of each Argo float. Assignment of the RPP relies on drift pressure measurements and configuration of park pressure assignments. If several park pressures are measured during a single drift phase, the RPP is the average value of those measurements. If only one number is reported (either as the mean of pressures or a single measurement) that becomes the RPP. If min and max pressures are given, the RPP is the mean value. When there is no pressure data available, the RPP is assigned from the reported configuration park pressure. This is checked locally, first against the local bathymetry and then against the reasonableness of the induced deep velocity. In the data set used for this study only one float had no measured park pressures and the 1000db programmed drift pressure appeared to be compatible with the surrounding bathymetry.

The Argo floats were sorted by drift depth (84 % at 1000db, 5 % below that and 11% above), and only floats that had an RPP of between 850 - 1250 db were used in the analysis. The Argo floats were a mix of Argos and Iridium based positioning. For further analysis only position data flagged as '3' (position accuracy of $<$ 150 m position uncertainty for Argos), and 'gps' (strong connection certainty for Iridium) were used for further velocity calculations and position tracks to limit track position errors once at the surface.

The measurement error encompasses several different points within the Argo cycle. The first is in the Argos positioning system, with a minimum position uncertainty of $<$ 150m. Using the midrange uncertainty of $<$ 1000m, Ichikawa, [Ichikawa et al., 2001], estimates velocity

errors of $\mathcal{O}(10^{-3}\frac{m}{s})$ for the 10 day cycle of the float. This error decreases with a decrease in position uncertainty. The second point of error comes in the form of clock drift which is considered to be negligible for the majority of floats. Within the dataset used for this study, there were no significant clock jumps. The third error comes from the drift associated with ascent and descent. The last error in the velocity estimates is unknown surface drift of the float while waiting for satellite connection and/or descent command. There are upper bound estimates for these errors from several sources [Lebdev et al., 2007, Katsumata and Yoshinari, 2010, Ichikawa et al., 2001, Ollitrault and Rannou, 2013]. Assuming a linear shear profile, Lebdev (2007) estimates the deep velocity errors at a mean of 5.3 $x10^{-3}\frac{m}{s}$, with the 'most probable' error around 2.5 $x10^{-3}\frac{m}{s}$. Katsumata (2003) uses a mean representative value of $5x10^{-3}\frac{m}{s}$ as a sampling error for deep velocities.

The Park et al. (2005) method extrapolates surface and dive positions from the known position fixes the float records and the float program time estimate for an actual surfacing and diving. We use this method for Argo velocity estimates yielding a total velocity uncertainty of $2x10^{-3}\frac{m}{s}$ [Park et al., 2005] independent of the number of floats, only requiring three or more surface fixes per surfacing. Velocity fields were estimated from the position tracks and cycle data following the methods outlined in [Park et al., 2005] and [Gray and Riser, 2014]. After this processing there were 152 Argo floats with 25,946 velocities used in the study.

All velocities, from Argo floats and LAUBFLEX were mapped onto a 0.25° X 0.25° Eulerian grid, with samples averaged in time bins of 3 months before fully averaging the area bin to limit the anomalous weighting from multiple observations within a short time frame due to one float occupying a bin for an extended number of continuous samples. The bins were then smoothed using a 2-D convolution filter with a gaussian halfwidth of 75km (Figures 2.3 & 2.4 discussed below in section 2.2.5). Four or more observations per bin were required for each bin, otherwise the bin velocities were set to an undefined value. It is worth noting that these bin sizes are smaller than have been used in other studies [Davis, 2005, Gray and Riser, 2014] which used 1° X 1° bins over larger sections of the Pacific basin. Smaller bin size does in-

crease bias within the bins, but was deemed necessary given initial estimates of the width of the western boundary current along the Lau Ridge, between 25km - 50km wide.

Transports within the Lau Basin were estimated from the float observations. For the float-based estimates, a layer 700m thick was chosen to match the nominal distance between the Argo floats (1000m) and the LAUBFLEX floats (1700m). The velocity used for the estimates was the mean of the binned data from Argo and LAUBFLEX through the Lau Basin. A conservative velocity error of 5mm/s applied to the dataset results in a $\pm$0.35Sv transport error due to velocity error. Transports within the Havre Trough were estimated from Argo displacements only since the LAUBFLEX floats did not reach that far south. Net transport was estimated using a 700m thick layer and a reference Argo velocity at 1000m.

2.2.4 Hydrographic Data

The World Ocean Experiment (WOCE), Climate Variability Project (CLIVAR), and Global Ocean Ship-board Hydrographic Investigations Program (GO-SHIP), produced three hydrographic lines crossing the basin (Figure 4.1). At the northern extremity of the Lau Basin, P31 runs from Fiji through the Samoan Passage. This hydrographic line has only been occupied once, in 1994, as a component of a mooring array project to study the deep flow through the Samoan Passage [Roemmich et al., 1996]. P21 lies nominally along 17.5°S bisecting the Lau Basin, and transects the Pacific Ocean from Australia to the western coast of South America. P21 has been occupied twice, in 1994 and again in 2009. In the southern limit of the Havre Trough, along 32.5°S, P06 has been repeatedly occupied; this is also the latitude of the PCM9 mooring array to measure the DWBC above the Kermadec Trench [Whitworth III et al., 1999]. P06 has been occupied four times thus far, 1992, 2003, 2009, and most recently in 2017.

CTD (conductivity, temperature, and depth) data were used for geostrophic velocity estimates relative to the 1000m dataset from Argo. The CTD data were processed using only data flagged as the most confident, all other values were deleted and filled by interpolation

using a Laplacian filter. The data are then re-interpolated linearly onto a uniform grid, finer than the original. A dynamic-height based streamfunction is calculated using absolute salinity (SA) and conservative temperature (CT), following the TEOS-10, referenced to 1000m. The geostrophic velocity is then estimated, referenced to the 1000m velocity field from the processed Argo floats that cover the hydrographic line's positions, or to 2000m on the P06 section.

The geostrophic velocity is found using:

$$\mathbf{k} \times \nabla_{surf} \Psi = f(\mathbf{v}_{geo} - \mathbf{v}_{ref}) \tag{2.1}$$

So then the geostrophic velocity is,

$$\mathbf{v}_{geo} = \frac{1}{f}(\mathbf{k} \times \nabla_{surf} \Psi + f\mathbf{v}_{ref}) \tag{2.2}$$

where $\mathbf{v}_{geo}$ is the geostrophic velocity vector, Ψ is the dynamic height streamfunction, f is the Coriolis parameter and $\mathbf{v}_{ref}$ is the reference velocity, in this case referenced to the 1000m Argo velocity data. ∇_{surf} here becomes ∇_p, since the dynamic height is referenced to a pressure surface.

Net transport estimates below 1000m were made from the $\mathbf{v}_{geo}$ estimates on P31 and P21, and below 2000m on P06. The flow field was integrated laterally from the western ridge to the eastern ridge and vertically every 2m. For hydrographic section P31, the flow field was integrated from Fiji northeast for 210km to a shallow shoal, and vertically every 2m. Error associated with the geostrophic velocity estimate comes from the reference velocity error (.35Sv), instrument error is negligible.

2.2.5 Float-based circulation estimates

The LAUBFLEX floats were the first observations to indicate a possible narrow (25-50 km wide) western boundary current along the Lau Ridge (Figure 2.3A), with northward

velocities of 6-7 cm/s and interior flows as strong as 3cm/s but typically much weaker [Speer and Thurnherr, 2012]. This current is evident from 21°S to 18°S, apparently disappears, and then re-appears from about 16°S until it exits into the North Fiji Basin through the North Fiji Passage. The gap is likely due to the sampling criteria of this analysis requiring at least 4 observations per bin. With relatively large velocities, long float cycle of the LAUBFLEX floats, and fewer floats, bins are undersampled. Inflow north of the North Fiji Passage is associated with a recirculation in the northern Lau Basin, flowing along a deep subsidiary ridge.

Argo displacement data (Figure 2.3B) in the area corroborate the western boundary current along the Lau Ridge and indicate that the current extends from 1700m to 1000m. The Argo data also yield a larger area coverage and indicate several other elements of the circulation in the Lau Basin (Figure 2.4). The first point is the latitudinal extent of the boundary current in the Lau Basin. Northward flow is fairly consistent from around 26°S through to the North Fiji Passage with velocities of 4-7 cm/s. At 26°S, a bifurcation in the flow leads to a southward flowing boundary current spur from about 26°S to about 30°S. Second, two westward jets are evident, one in the northern portion of the Havre Trough at 26°S and one in the northern portion of the Lau Basin at about 17°S. These two jets align with breaks in the ridge systems: the Tonga Passage (north) and the Kermadec Passage (south). Due to the bifurcation in the boundary current, there are also at least two outflow passages, the Colville Passage in the south, and the North Fiji Passage. Another relatively strong current lies on the Tonga Ridge, feeding the Tonga Passage source into the Lau Basin.

We find two relatively strong areas of recirculation, in the central Lau Basin centered near 19°S and another in the northern portion of the Havre Trough, centered near 30°S.

Both of these recirculation systems roughly follow constant geostrophic contours of large scale potential vorticity contours (f/h, where f is the Coriolis parameter and h is the thickness of the water column below 1000m depth; see Discussion). Within the Havre Trough the sense of the circulation is anticyclonic, consistent with the embracing boundary current

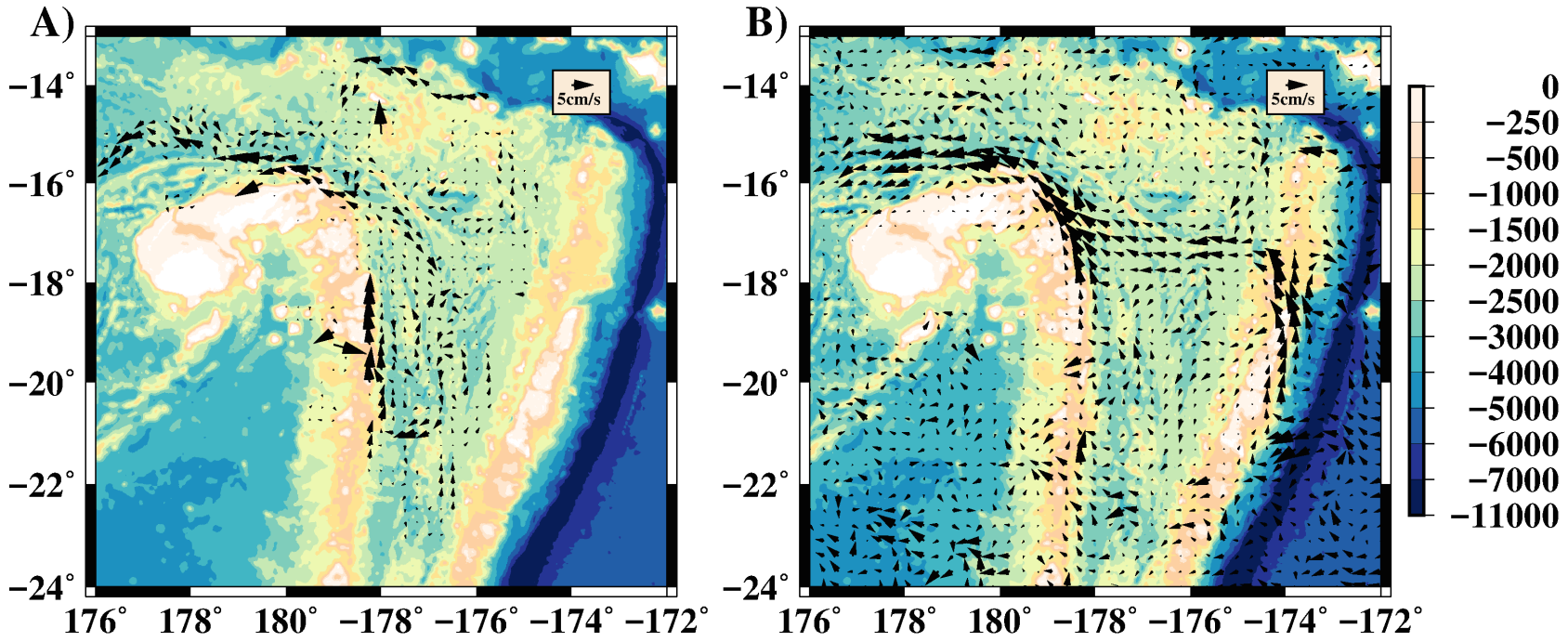

Figure 2.3: Binned velocities from LAUBFLEX and Argo. A) LAUBFLEX velocity at 1700m B) Argo velocity at 1000m. A westward jet is evident crossing the Lau Basin at 17°S.

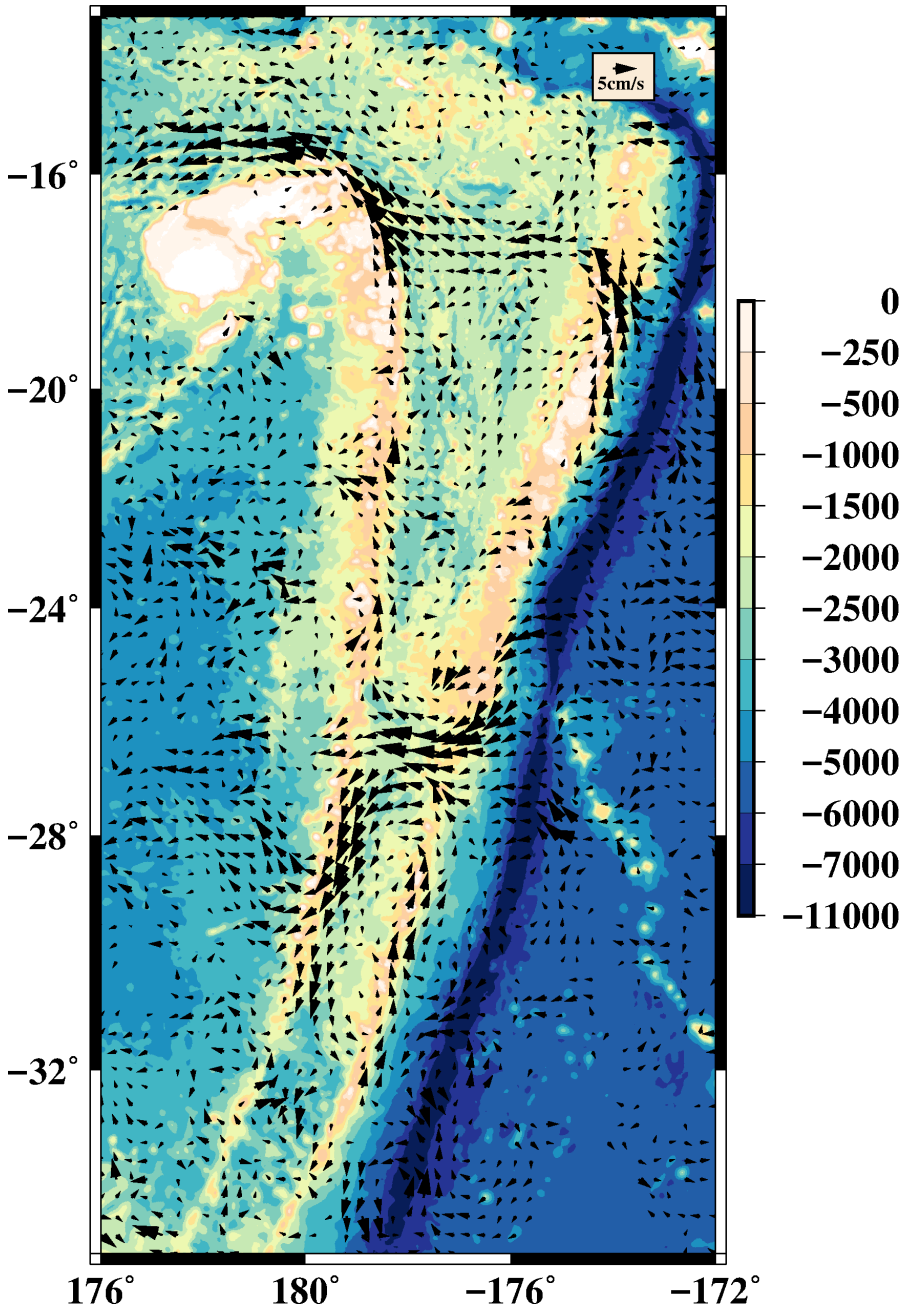

Figure 2.4: Argo velocity. Two westward jets are located at 17°S and 26°S. The bifurcation along the Colville Ridge, in which part of southern jet turns northward while the majority flows south, is located near 26°S. The northward flowing boundary current exits the Lau Basin through the North Fiji Passage near 16°S.

flow, with a northward return arm along the Kermadec Ridge. In the central Lau Basin the recirculation is cyclonic, with some of the western boundary current water returning southward within the central Lau Basin. A weaker anticyclonic recirculation is evident in the northern Lau Basin.

2.2.6 Hydrography

Potential temperature is lowest on Stn.84 from P06 (2017), in the Havre Trough, at 1.853°C, with the minimum potential temperature increasing to 1.947°C on P21 (2009); temperature is lower again on P31 at 1.885°C (Figure 2.5). The Havre Trough P06 potential temperature salinity relation converges to the South Fiji Basin relation within error below about 2°C (Figure 2.6), showing that the source of bottom water is the South Fiji Basin, and confirming the supposition of Wyrtki (1960), who had no data within the Havre Trough, that the Havre Trough is a minor dependent basin of the South Fiji Basin. On the other side of the Colville Ridge in the South Fiji Basin, bottom potential temperature is 1.545 C. These results suggest that the sill near 32°S (Figure 2.2) supplies the Havre Trough, at least as far as the rise separating the Havre Trough from the Lau Basin. This 32°S sill is slightly deeper than the saddle between New Zealand and the Kermadec Ridge. Warren et al (1994) observed the Havre Trough near this latter sill and found the coldest bottom water there to be 2.0°C.

The eastern side of the Havre Trough on P06 is slightly warmer, at 1.925°C (Figure 2.5D-G). The more recent occupations show somewhat higher temperatures. Silica concentration (Figure 2.7D-G) is slightly lower in the east, and higher on the western side of the trough, but only by about 2 μmol/kg; oxygen concentrations (not shown) are indistinguishable across the bottom, with a value near 154 μmol/kg. These properties are similar to those outside the trough at 2400-2500m, and consistent with both a South Fiji Basin source and some mixture of water from the DBWC entering at the saddle on the Kermadec Ridge, whose flow is

blocked by the shallower sill on the Colville Ridge, thus turning that inflow north toward P06.

The minimum observed temperature on P21, 1.947°C, occurs on the western side of the basin, corresponds also to higher silica (Figure 2.7B,C). The coldest bottom water on P31, at the northern limit of the basin, also occurs on the western side of the section. The northern Lau Basin evidently gets its water from the north, which first enters an area of anticyclonic recirculation (see below). This recirculation branches at 17°S, such that one branch carries similar properties to the western side of P21. Bottom water properties in the northern Lau Basin thus arrive from the north, through the northeastern side of the North Fiji Passage, and participate in the recirculation in this area described below. The role of the Tonga Passage as a source of bottom water is unclear, as properties at the closest stations (on P21) do not suggest a nearby source.

2.2.7 Geostrophic flow estimates

North Lau Basin. Along hydrographic line P31, a strong (8cm/s) north-northwestward flow is evident below 1000m hugging a portion of the Fiji Island bathymetry and extending close to 100km northeast (Figure 2.8A). There is a slower (1cm/s) southeastward flow outside the boundary flow, to just past 200km. A small opposing flow is observed beyond that, near a complicated bathymetric area just west of the Vitiaz Trench. Circulation in the upper 1000m is roughly consistent with Reids (1997) steric height maps, with outer flow around the rim of the Lau Basin. But closer to the Fiji plateau the flow is directed in the opposite sense perhaps related to local effects of the plateau.

Comparing the calculations based on hydrography with the LAUBFLEX deep float velocities, the geostrophic velocities are about two times larger than the float velocities. The hydrography also indicates a wider DWBC (100 km) than the floats (50 km). A net transport estimate below 1000m from the geostrophic flow (Section 2.2.4) results in 5.9Sv ±1Sv exiting the Lau Basin region. Comparison with transport estimates from the floats (Section

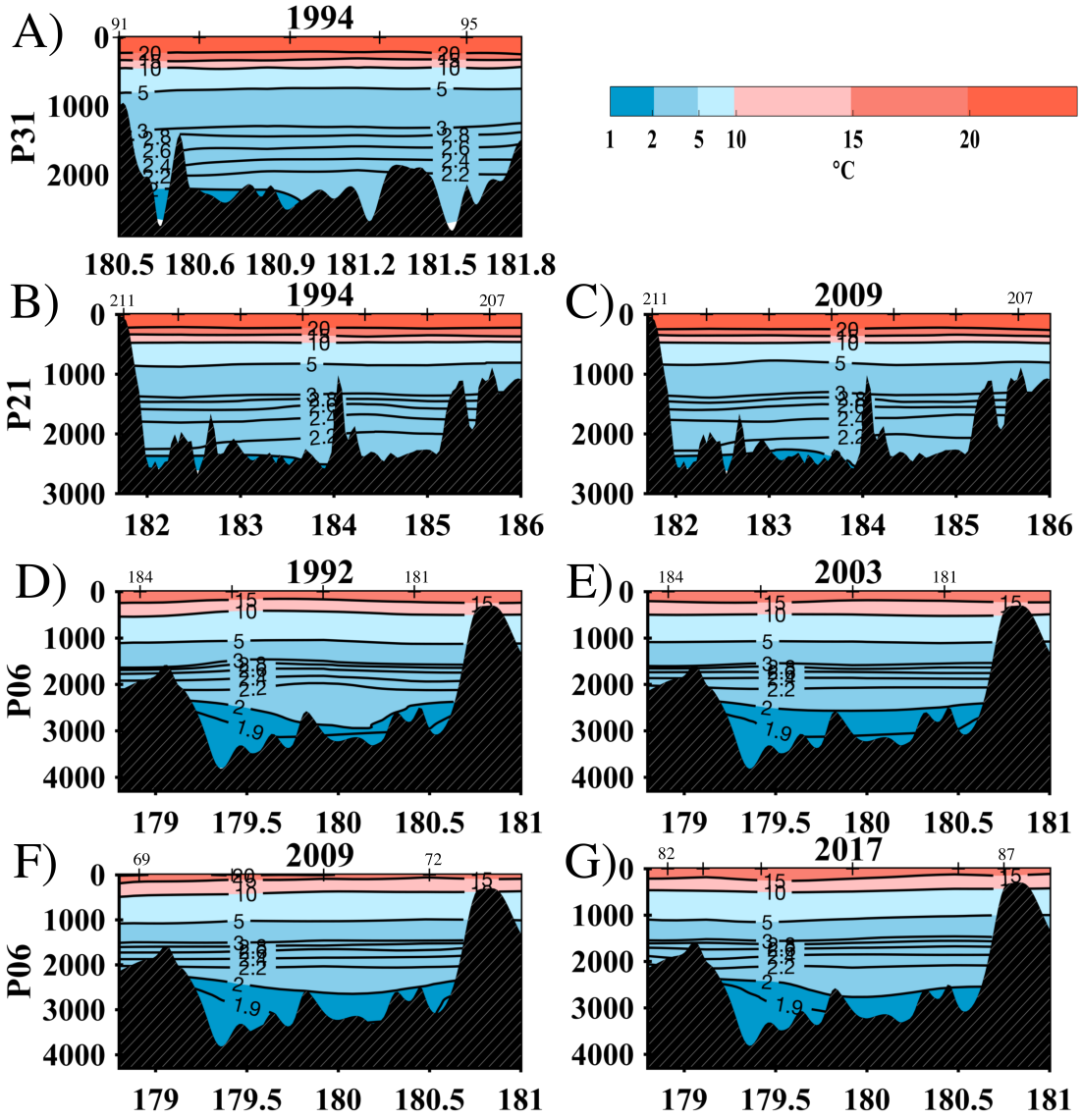

Figure 2.5: Potential Temperature for each hydrographic section and occupation in the Lau Basin and Havre Trough. A) P31 B) P21, occupation in 1994 C) P2, occupation in 2009. D) P06, occupation in 1992 E) P06, occupation in 2003 F) P06, occupation in 2009. G) P06, occupation in 2017.

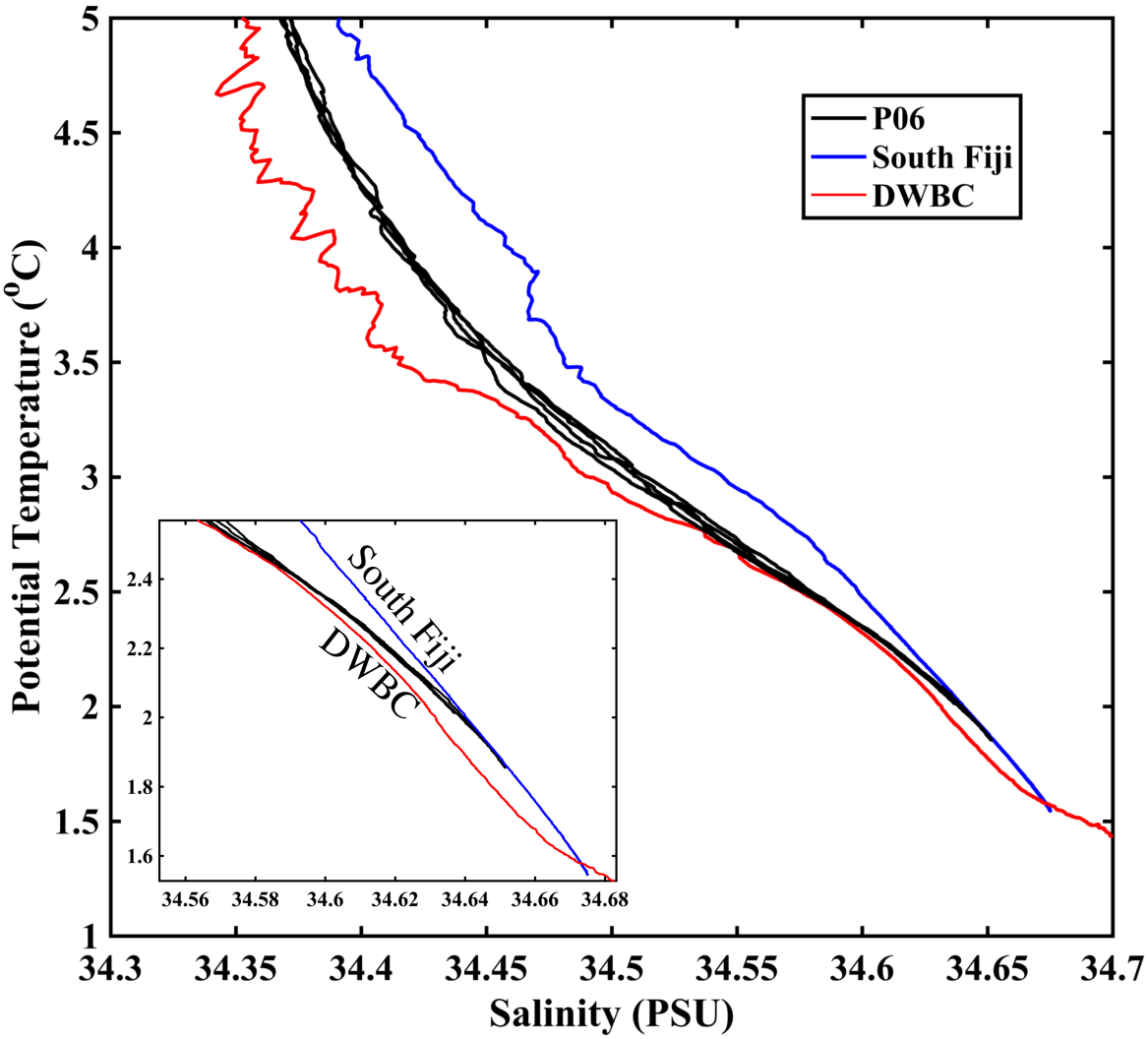

Figure 2.6: T-S plot of hydrographic stations from P06 (2017) in the southern Havre Trough. A representative DWBC station (red) and South Fiji Basin station (blue) are shown as well.

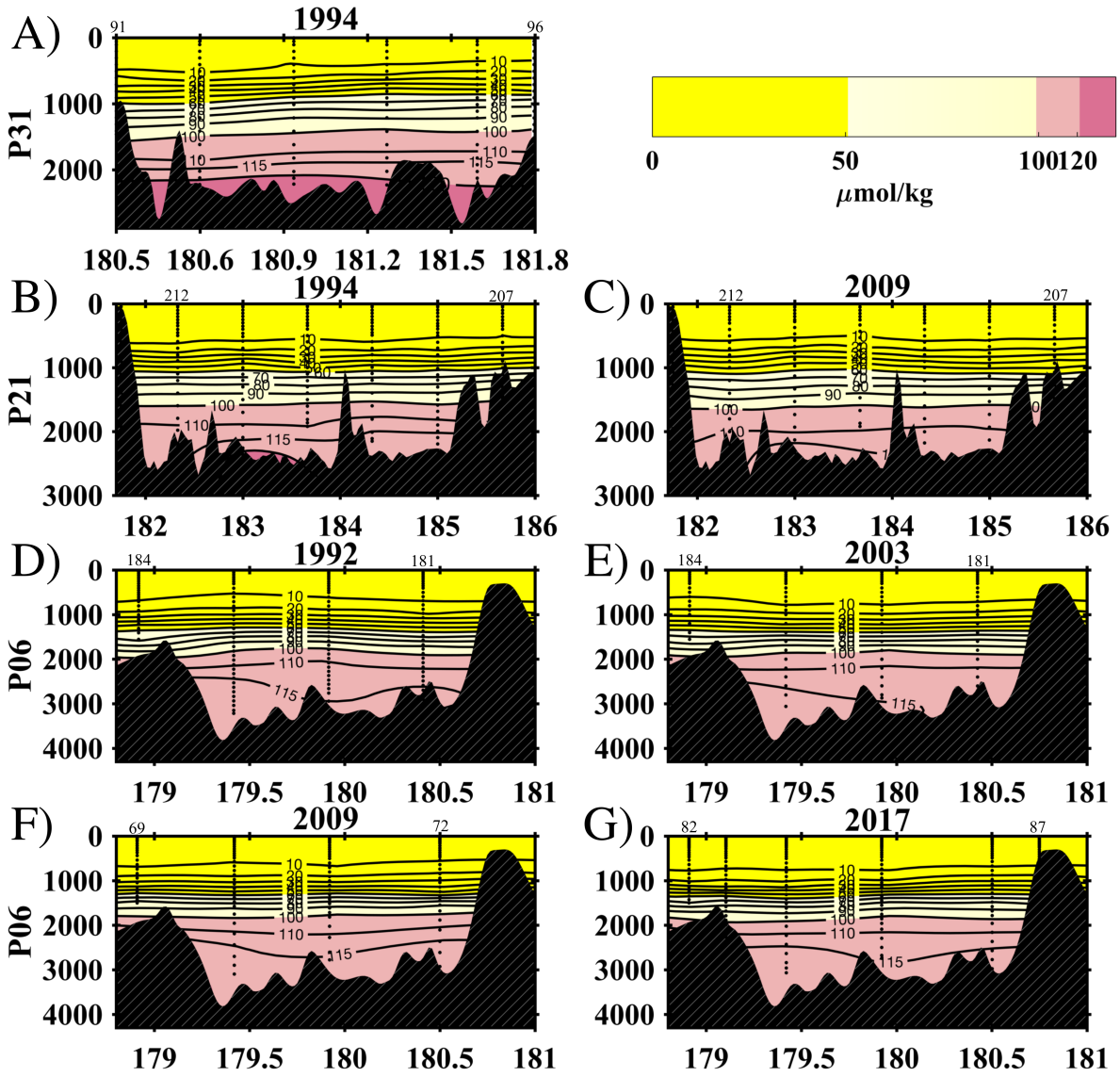

Figure 2.7: Silica observations for each hydrographic section and occupation in the Lau Basin and Havre Trough. A) P31 B) P21, occupation in 1994 C) P2, occupation in 2009. D) P06, occupation in 1992 E) P06, occupation in 2003 F) P06, occupation in 2009. G) P06, occupation in 2017.

2.2.3), 5.6Sv ±1Sv, indicates that though the LAUBFLEX velocities are smaller than the geostrophic velocity estimates, the transport estimates agree on the relatively large transport out of the Lau Basin region.

Lau Basin. Along P21, there is a strong (8-9cm/s) and narrow (about 70km) northward flow along the Lau Ridge from 750m to below 2000m (Figure 2.8B and 2.8C). This northward flow is trapped to the Lau Ridge with its strongest flow centered between 1500 and 2000m. The southward flow that occurs east of the boundary current has speeds of 4-6cm/s, is relatively wide ($\sim$ 160km)for the Lau Basin, and is mostly seen below 1000m depth.

There are two, weak (<1cm/s), and narrow (50-75km) alternating flows from about $183.5°E$ and eastward to the Tonga Ridge along P21. Near the Tonga Ridge is a deep southward inflow. Both occupations of P21 show similar patterns, though the first occupation in 1994 indicates a narrower ($\sim$ 50km), and slower (5-6cm/s) northward flow next to the Lau Ridge.

Comparison with the LAUBFLEX results along the P21 17.5°S line shows that the western boundary current is weaker in the float observations, $\sim$1cm/s, versus 5cm/s or so in the geostrophic fields. Outside (east) of the boundary the LAUBFLEX float trajectories do, however, indicate an inflow region consistent with the geostrophic calculations, but with smaller associated velocities. The net transport estimates yield similar relationships as those for P31. The net transport of P21 in the 1994 occupation is 3.7Sv ±1Sv northward and in the P21 2009 occupation is 4.1Sv ±1Sv northward, in agreement with the float-based net transport of 4.9±1Sv northward.

Southern Havre Trough. P06 hydrography indicates, initially somewhat to our surprise given the source passage just to the north of the P06 section, a deep northward flow along the Colville Ridge within the Havre Trough (Figure 2.8D-G). At this location the flow

shows smaller scale vertical structure; the apparent minimum in vertical shear near 2000m depth led us to choose that depth as a zero velocity reference level. With this choice the core of the flow appears to be aligned with the observed weak property variations. As remarked above, the bottom properties are consistent with inflow from the South Fiji Basin, with shallower levels receiving some component of water from the southern end of the Kermadec Ridge, though we are unable to make much of a distinction between the western and eastern sides of the trough. The width of the current varies between 30km and 45km wide probably because of variations in horizontal station spacing and resolution. The vertical extent is stable across the sections, with northward flow below about 2500m depth.

Velocity in bottom flow of the Havre Trough geostrophic flow is 1-2 cm/s. Net transport estimates from each of the four occupations of P06 indicate negligible net throughflow: 0.5Sv ±1Sv (1992), 0.3Sv ±0.5Sv (2003), -0.2 ±0.5Sv (2009), and 0.03Sv ±0.05Sv for an average of 0.1 Sv. Argo float-based net transport along 32.5° across the Havre Trough, from Colville Ridge to Kermadec Ridge, for what it is worth, also indicates negligible (1Sv ±1Sv) net southward flow.

2.3 Analytical Model

Pedlosky [Pedlosky, 1994] proposed an extension to the traditional Stommel-Arons abyssal circulation model, accounting for leaky or gappy ridges along a boundary, making use of Godfrey's Island Rule [Godfrey, 1989]. The model used in Pedlosky's work is a single layer, homogeneous fluid with a forcing given by an upwelling term $w_*(x, y)$ at the layer's surface. Governing dynamics are given by the linear barotropic vorticity equation:

$$\beta v = \frac{f w_*}{H} - r(\frac{\partial v}{\partial x} - \frac{\partial u}{\partial y}) \tag{2.3}$$

Where the advection of planetary vorticity is driven by the planetary vortex stretching given by the vertical velocity described by w_*. The frictional dissipation of vorticity, the

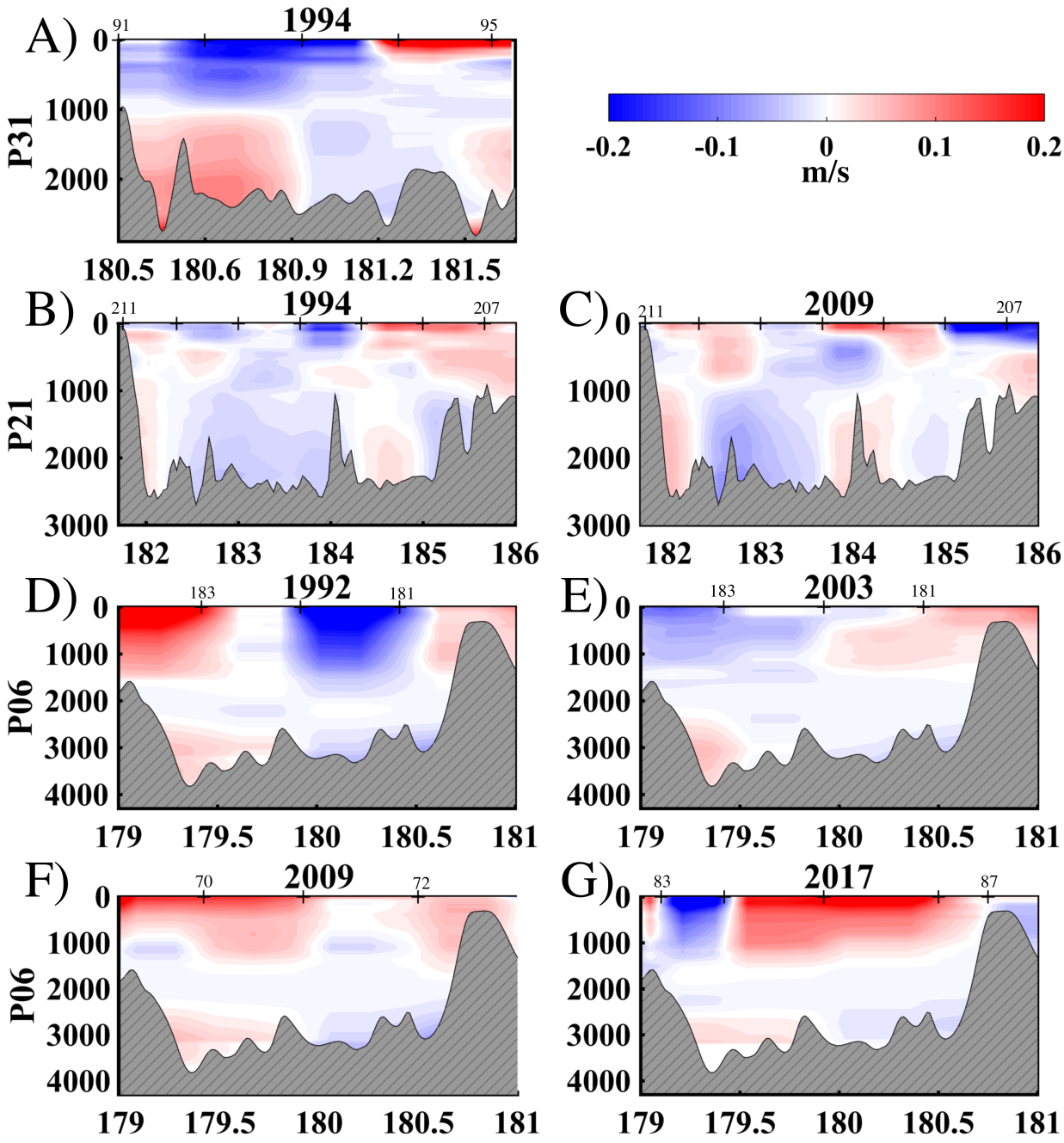

Figure 2.8: Geostrophic velocity for each hydrographic section and occupation in the Lau Basin and Havre Trough. Positive values (red), negative values (blue). A) P31 B) P21, occupation in 1994 C) P2, occupation in 2009. D) P06, occupation in 1992 E) P06, occupation in 2003 F) P06, occupation in 2009. G) P06, occupation in 2017.

second term on the RHS of the above equation, is assumed to be small and negligible everywhere outside of the boundary layer such that:

$$\frac{r}{\beta L} << 1 \tag{2.4}$$

Where L is a characteristic length scale of the size of the basin and the distribution of the upwelling, r is a frictional parameter, and β is the planetary β. The β-plane approximation is assumed to hold as well as the assumption that the velocity can be reasonably obtained from a geostrophic streamfunction, ψ, such that $u = -\frac{\partial \psi}{\partial y}$ and $v = \frac{\partial \psi}{\partial x}$.

The vorticity equation can then be written in terms of ψ,

$$\beta \frac{\partial \psi}{\partial x} = \frac{f w_*}{H} - r\nabla^2 \psi \tag{2.5}$$

Where $\psi = \frac{p}{\rho f_0}$. The setup of Pedlosky's example consists of two gaps located at the top and bottom of the ridge while two other ridge breaks are located within the middle of the ridge system. East of the segmented ridge the interior solution takes the form of

$$\phi_I = \int_x^{x_E} -\frac{f w_*}{\beta H}(x', y) dx' \tag{2.6}$$

The interior streamfunction is the westward integration of the ratio between vortex stretching due to upwelling and planetary β. While on the individual ridge segments the streamfunction takes on a slightly more complicated form,

$$\phi_j = \phi_I(x, y) - (\phi_I(x_T, y) - \gamma_j) e^{-(x - x_T)/\delta} \tag{2.7}$$

Where $\delta = r/\beta$ is the Stommel boundary layer, ϕ_I is the interior solution of (6), and $\phi_I(x_T, y)$ is the interior solution at the ridge. The resultant streamline from this provides a transport that may be compared to observations or other derived transport estimates. The constant γ_j is determined by an integral condition requiring that the net along-ridge frictional force vanish. It consists of the integration of the component of the momentum equation tangent to the ridge, around each ridge segment. γ_j takes the form:

$$\gamma_j = \frac{1}{(y_{jN} - y_{jS})} \int_{y_{jS}}^{y_{jN}} \phi_I(x_T, y) dy \tag{2.8}$$

The value of γ_j changes on each ridge segment since it is the average value of the interior ϕ along each segment. When $\phi_I = \gamma_j$ a stagnation point occurs on the ridge. If the ridge is 'long enough' two (or more) stagnation points can occur on the same j^{th} segment leading to an isolated recirculation cell existing whose boundary is given by the stagnation point form. When $\phi_I > \gamma_j$ the flow is directed to the north of the stagnation point, when $\phi_I < \gamma_j$ the flow is turned to the south of the stagnation point.

The ridges are very simple vertical walls along which the fluid rides. It is assumed that within the basin there is no topography, and no sloping island skirt. This leads to a simplified model of flow control and transport.

For the Lau Basin the topography is idealized to two vertical, parallel ridges with openings corresponding to the passages noted in the observed data set (Figure 2.2). The passages are simplified to a rectangular opening with an average depth based on the sill depth of the Tonga and Kermadec Ridges. Unlike the Pedlosky model, here no upwelling term is prescribed; instead, a non-zero eastern boundary streamline is set to represent the inflow through the Tonga Passage and the Kermadec Passage using velocities from the Argo float dataset. The outflow is not prescribed at each opening on the western boundary, allowing the stream field to adjust based on the dynamics described in the model. It is demanded, though, that the total inflow is balanced by the total outflow. The model results show the two westward jets observed in the Argo data and more interestingly itself the southern bifurcation point of the boundary current, directing a portion of the flow north while the rest flows southward along the ridge (Figure 3.5).

In this particular model configuration, $\gamma_j \neq \gamma_{j+1}$, the ridge system is not long enough and no two stagnation points are connected by the same streamline, the recirculation regions are not completely isolated, so the pools of each recirculation communicate with the western basin through zonal jets that flow westward through the gaps in the ridge system.

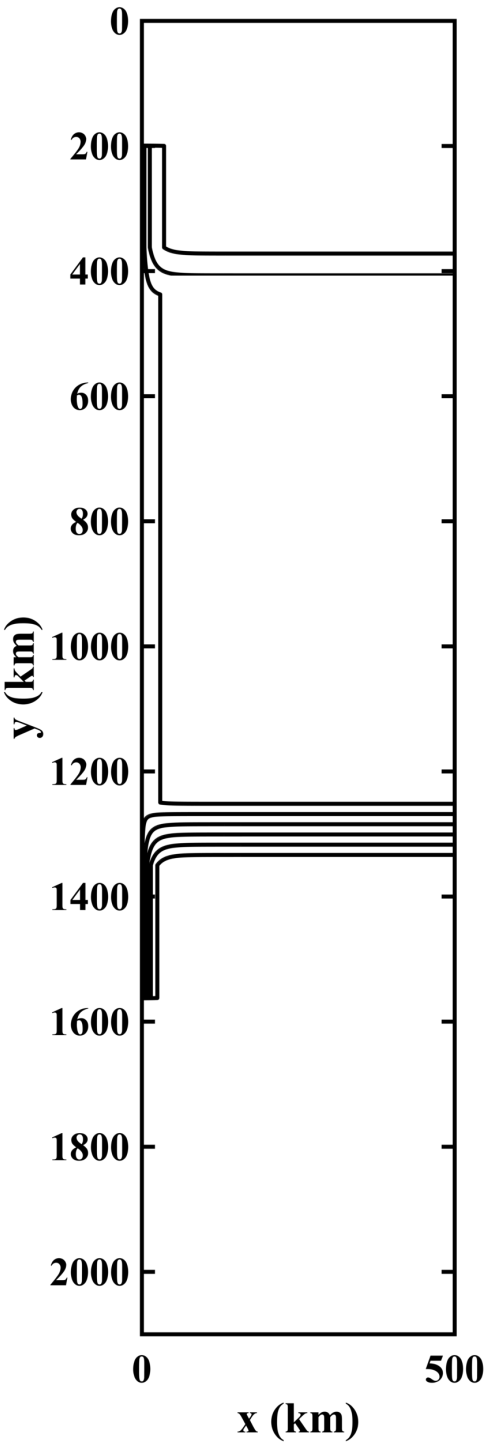

Figure 2.9: Simple flat bottom, uniform layer Stommel-Arons model with the extension to Pedlosky in the gaps of the ridges.

2.4 Western Boundary Transport Comparisons

Western boundary current transport was estimated from the float data, the geostrophic velocities derived from the hydrographic data, and the analytical model output. For the float data, a similar process was used as outlined in Section 2.2.3. The boundary current flow was integrated laterally until the first zero velocity line, designating the lateral end of the boundary current. The geostrophic velocity derived transports of the boundary currents were estimated by integrating laterally to the zero velocity line. The analytical model output provides a transport streamline.

Forcing the inflow region of the analytical model with values similar to those observed in the inflow region of the Argo data results in boundary current transports on par with transport estimates taken from the observational data (Figure 2.10). There is good agreement between the transport estimates, with the Fiji Passage outflow transport balancing the boundary current within the Lau Basin. A total of 3-4 Sv$\pm$1Sv is transported within the DWBC in the Lau Basin and exits into the North Fiji Basin.

2.5 Discussion

Hydrography and Argo displacement data not only reveal the boundary current system in the northern part of the Lau Basin but also the extension of the boundary current into the southern portion of the Lau Basin. Boundary current systems are present in the Havre Trough along both the Lau Ridge and the Colville Ridge systems. These boundary currents are fed by two westward flowing jets located at 18°S and 27°S respectively.

Geostrophic velocity estimates from the WOCE, CLIVAR, and GO-SHIP hydrographic lines together provide independent support for the presence of the western boundary current system along the Lau and Colville Ridges. Net transport and boundary current transport estimated from the hydrographic sections also agree well with the net transports and boundary

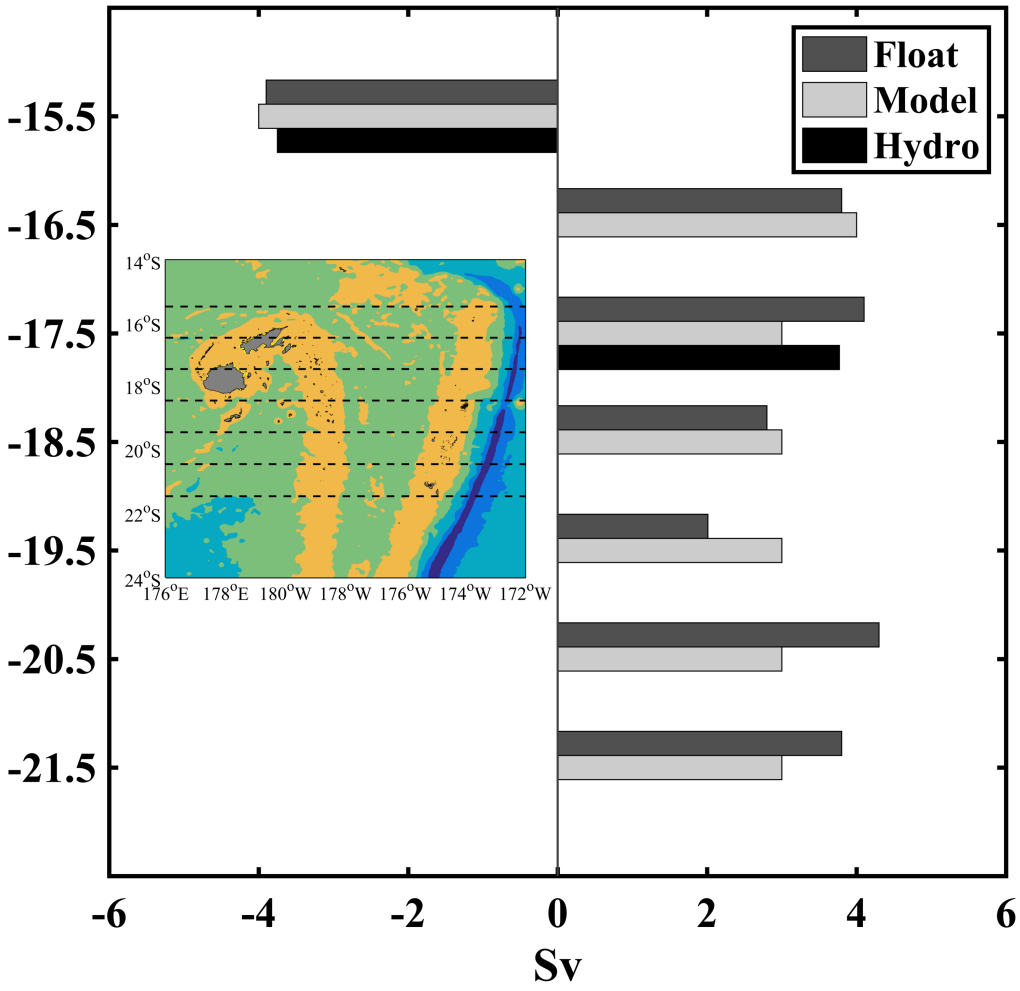

Figure 2.10: Transport of the western boundary flow estimated from float observations, analytical model output, and geostrophic velocity derived from hydrographic data: P31 and P21 (black), float derived transports (dark grey), and the model (light grey). The inset shows the northern portion of the basin and the midpoints of the transport estimates.

current transports derived from the float data within the Lau Basin and the Havre Trough.

The flow bifurcation on the Colville Ridge, where the southern, westward-flowing jet comes into contact with the ridge, provides an opportunity to test simple ideas about basin-scale control on boundary current systems. The bifurcation leads to a northward flowing boundary current that joins flow in the northern portion of the Lau Basin along the Lau Ridge, and a short, southward flowing current along the Colville Ridge in the Havre Trough that exits into the South Fiji Basin. The boundary current that exits into the North Fiji Basin is a tightly confined jet even after leaving the boundary.

Using Pedlosky's extension to the Stommel-Arons abyssal circulation model, with only inflow forcing and no interior upwelling, gives a reasonable, albeit simplified view of the dynamics controlling the boundary currents. Prescribing the inflow from the Argo float velocities results in boundary current transports in agreement with the estimates of boundary current transport from the Argo and LAUBFLEX floats. The analytical model also predicts the flow bifurcation and location of the bifurcation observed in the Argo float displacements. The regions of recirculation and other interior flow observed in the Lau Basin and Havre Trough are not, however, represented in the analytical model. Linking the boundary current transports to the interior recirculation and other interior components of flow, if indeed there is a link, and relating these, in turn, to the sources of water at various depths remains to be done.

Three regions of recirculation are present, two in the Lau Basin, the other in the Havre Trough. In the Lau Basin both the northern and central areas of recirculation are formed by a deep flow counter to the general western boundary current flow direction; this flow branches at the westward jet near 17-18°S with one branch crossing underneath to continue south and close the central recirculation loop at about 22°S. Strong recirculation appears in the Havre Trough centered near 30°S. Deep recirculation linked to topography is fairly common, and these flows appear to be responding to both topography and the Coriolis parameter such

that they roughly follow f/h contours. This linkage is illustrated by combining the velocity estimates from both the Argo and LAUBFLEX float observations with geostrophic contours (Figure 2.11).

While a remarkably consistent picture of the circulation emerges from the combined float tracks, it should be emphasized that most of the individual mean float velocities are insignificant or barely significant. The coherence between the float displacements and the underlying topography, whose depth varies so dramatically throughout the region, is expected to be highly variable. Nevertheless, a consistent structure emerges from the various datasets of a vigorous deep circulation in the Lau Basin and Havre Trough, with a strong connection to surrounding basins.

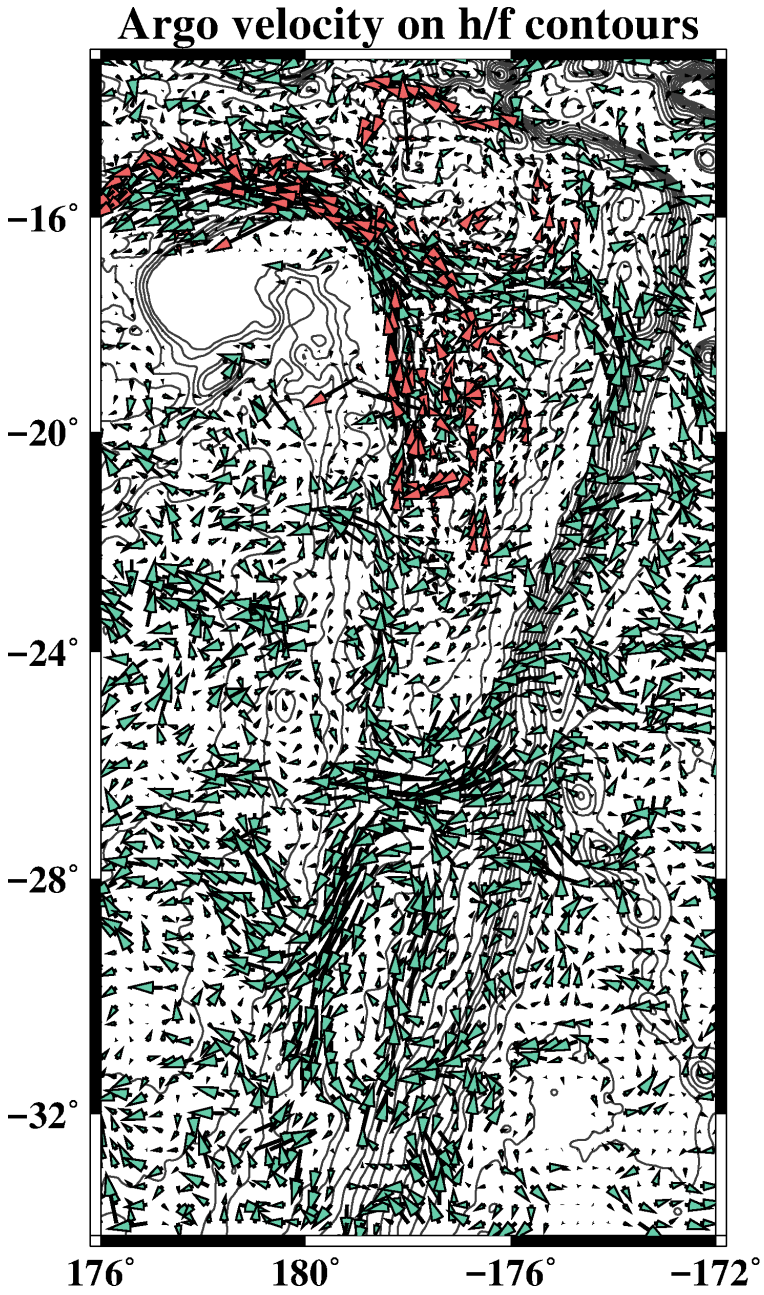

Figure 2.11: LAUBFLEX and Argo velocities on f/h contours. Three main areas of recirculation stand out, cyclonic and anticyclonic circulation in the Lau Basin indicated by the LAUBFLEX (red) data, and another anticyclonic circulation in the Havre Trough (blue), indicated by the Argo data.

CHAPTER 3

MODELING OF THE LAU BASIN AND HAVRE TROUGH

3.1 Introduction

The Lau Basin and Havre Trough are bordered by extremely complicated and gappy ridge systems; the Lau and Colville Ridges to the west and the Tonga and Kermadec Ridges to the east (Figure 3.1). The interiors of the Lau Basin and Havre Trough also have rough and variable topography due to the fast spreading centers located within the Lau Basin, and the young age [Gill, 1976] of the sea floor within the sub-basins in comparison to the age of the sea floor of the interior Pacific Ocean.

Float observations in the area indicate flow through the gappy ridge systems to the east, resulting in two distinct westward flowing jets that impinge on the Lau and Colville Ridges turning into a deep western boundary current (DWBC). The southernmost jet's interaction with the Colville Ridge results in a stagnation point and flow bifurcation, with a portion of the flow turning northwards to join with the northward flowing DWBC along the Lau Ridge with the rest forming a short southward flowing DWBC along the Colville Ridge.

The role of the variable topography associated with the Lau Basin and Havre Trough on the flow patterns observed in float data and hydrographic data is pursued through this document.

3.2 Analytical Model with Vertical Walls

In Chapter 2: Circulation in the Lau Basin and Havre Trough, Section 3: Analytical Model, the extension proposed by Pedlosky (1994) to the traditional Stommel-Arons (1958)

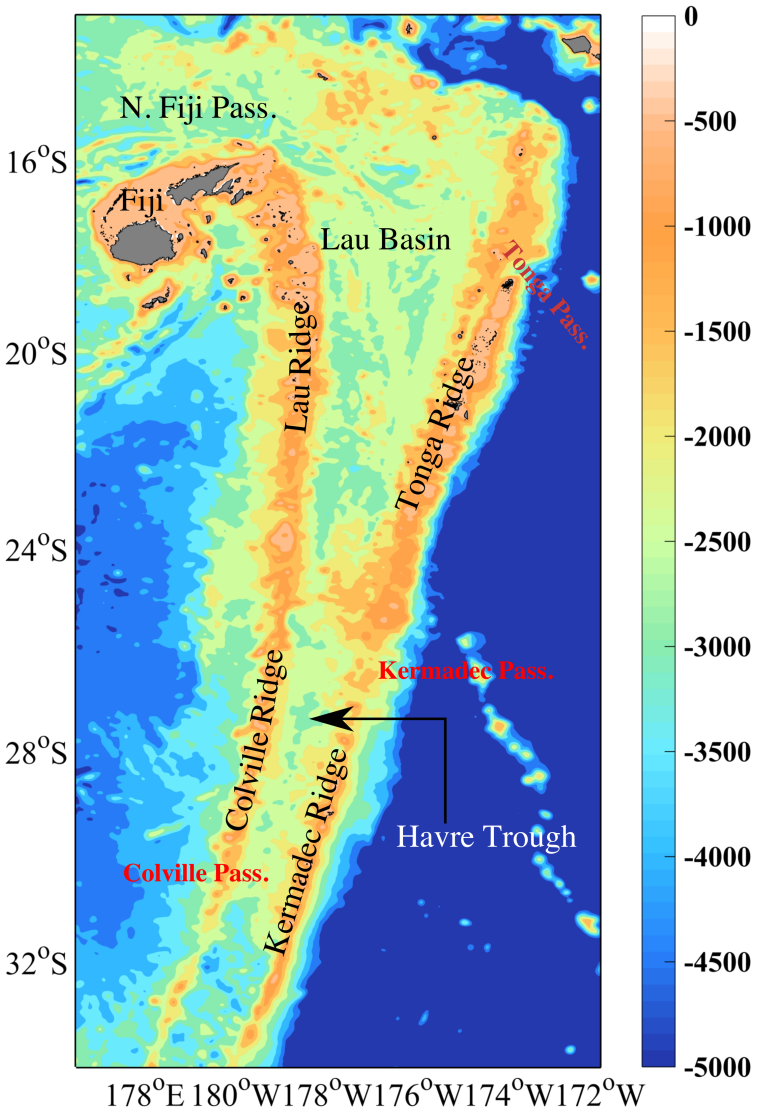

Figure 3.1: Topographic map of the Lau Basin and Havre Trough. Ridges, passages, and landmasses are labeled.

abyssal circulation model was shown to predict the flow bifurcation observed in the Argo float and Lau Basin Float Experiment float datasets. Here we aim to understand why such a simple model can explain this behavior even though reality permits modification of dynamics through stratification and variable topography. For completeness, a brief summary of this model extension and application to the study area follows.

The model used in Pedlosky's work is a single layer, homogeneous fluid with a forcing given by an upwelling term $w_*(x, y)$ at the layer's surface. Governing dynamics are given by the linear barotropic vorticity equation:

$$\beta v = \frac{f w_*}{H} - r(\frac{\partial v}{\partial x} - \frac{\partial u}{\partial y}) \tag{3.1}$$

Making the assumption that β-plane holds and that the velocity can be obtained from a geostrophic streamfunction, ψ, the vorticity equation can be written in terms of ψ,

$$\beta \frac{\partial \psi}{\partial x} = \frac{f w_*}{H} - r\nabla^2 \psi \tag{3.2}$$

The setup of Pedlosky's example consists of two gaps located at the top and bottom of the ridge while two other ridge breaks are located within the middle of the ridge system (Figure 3.2).

East of the segmented ridge the interior solution takes the form of

$$\phi_I = \int_x^{x_E} -\frac{f w_*}{\beta H}(x', y) dx' \tag{3.3}$$

While on the individual ridge segments the streamfunction takes on a slightly more complicated form,

$$\phi_j = \phi_I(x, y) - (\phi_I(x_T, y) - \gamma_j) e^{-(x - x_T)/\delta} \tag{3.4}$$

Where $\delta = r/\beta$ is the Stommel boundary layer, ϕ_I is the interior solution of Eqn.3.3 , and $\phi_I(x_T, y)$ is the interior solution at the ridge. γ_j is determined by an integral condition requiring that the net along-ridge frictional force vanish and consists of the integration of

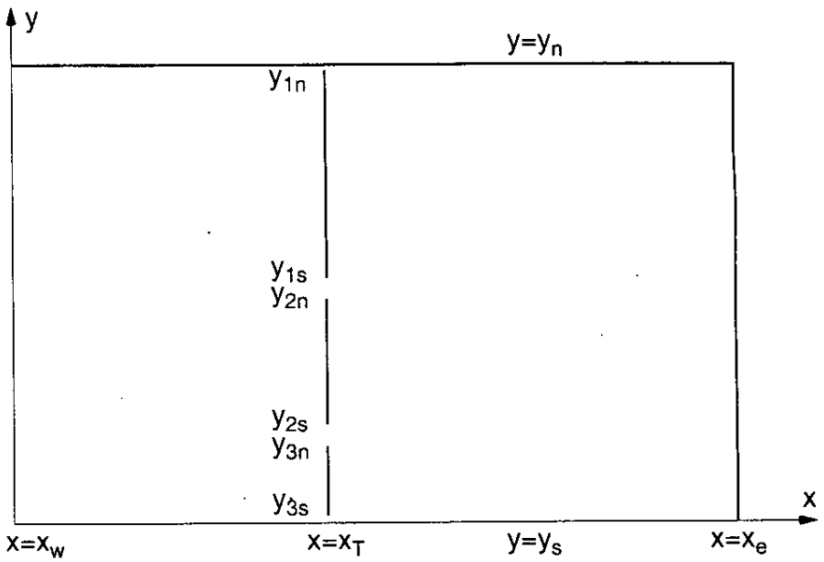

FIG. 1. The basin containing the flow. The rectangular basin is divided into an eastern ($x > x_T$) and western basin ($x < x_T$) by a ridge at $x = x_T$ with gaps at the locations shown.

Figure 3.2: Schematic of setup of gappy ridge in Pedlosky (1994). Original figure caption included.

the component of the momentum equation tangent to the ridge, around each ridge segment. γ_j takes the form:

$$\gamma_j = \frac{1}{(y_{jN} - y_{jS})} \int_{y_{jS}}^{y_{jN}} \phi_I(x_T, y) dy \tag{3.5}$$

The value of γ_j changes on each ridge segment since it is the average value of the interior ϕ (Equation 3.3) along each segment. When $\phi_I = \gamma_j$ a stagnation point (location where the boundary layer flow reaches zero) occurs on the ridge. If the ridge is 'long enough' two (or more) stagnation points can occur on the same j^{th} segment leading to an isolated recirculation cell existing whose boundary is given by the stagnation point form (Figure 3.3) . When $\phi_I > \gamma_j$ the flow is directed to the north of the stagnation point, when $\phi_I < \gamma_j$ the flow is turned to the south of the stagnation point.

Application of this model extension to the study area required a simplification of the topographic complexity. For the Lau Basin the topography is idealized to two vertical, parallel ridges with openings corresponding to the passages noted in the observed data set (Figure 3.4). The passages are simplified to a rectangular opening with an average depth based on the sill depth of the Tonga and Kermadec Ridges. Unlike the Pedlosky model, here no upwelling term is prescribed; instead, a non-zero eastern boundary streamline is set to represent the inflow through the Tonga Passage and the Kermadec Passage using velocities from the Argo float dataset (See Chapter 2, Section 2.2).

The outflow is not prescribed at each opening on the western boundary, allowing the stream field to adjust based on the dynamics described in the model. It is demanded, though, that the total inflow is balanced by the total outflow. The model results show the two westward jets observed in the Argo data and more interestingly itself the southern bifurcation point of the boundary current, directing a portion of the flow north while the rest flows southward along the ridge (Figure 3.5).

In this particular model configuration, $\gamma_j \neq \gamma_{j+1}$, the ridge system is not long enough and no two stagnation points are connected by the same streamline, the recirculation regions

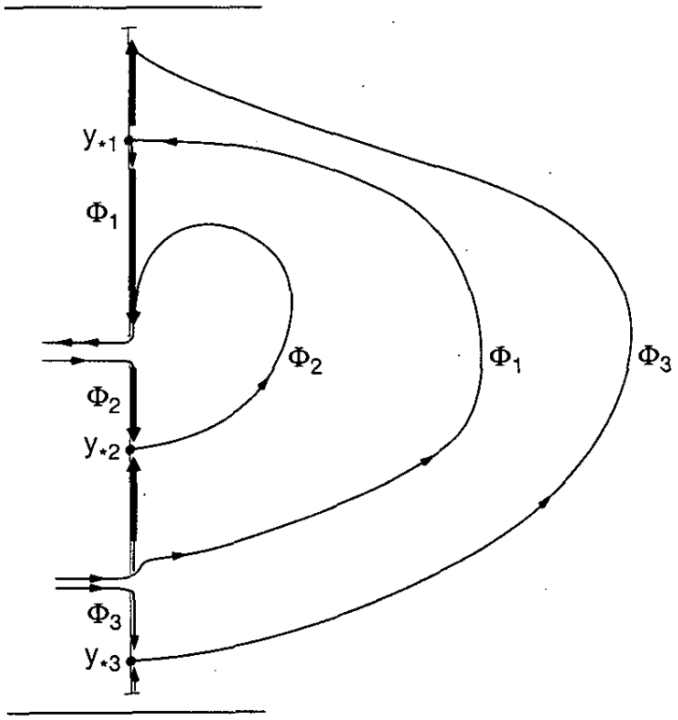

FIG. 5. A schematic of the principal elements of the circulation in the example described in Fig. 4. The streamlines connected to each stagnation point are shown, as well as the zonal jets issuing from the western basin.

Figure 3.3: Schema of results associated with the setup in Figure 3.2 from Pedlosky (1994). Figure from Pedlosky (1994) with original caption included.

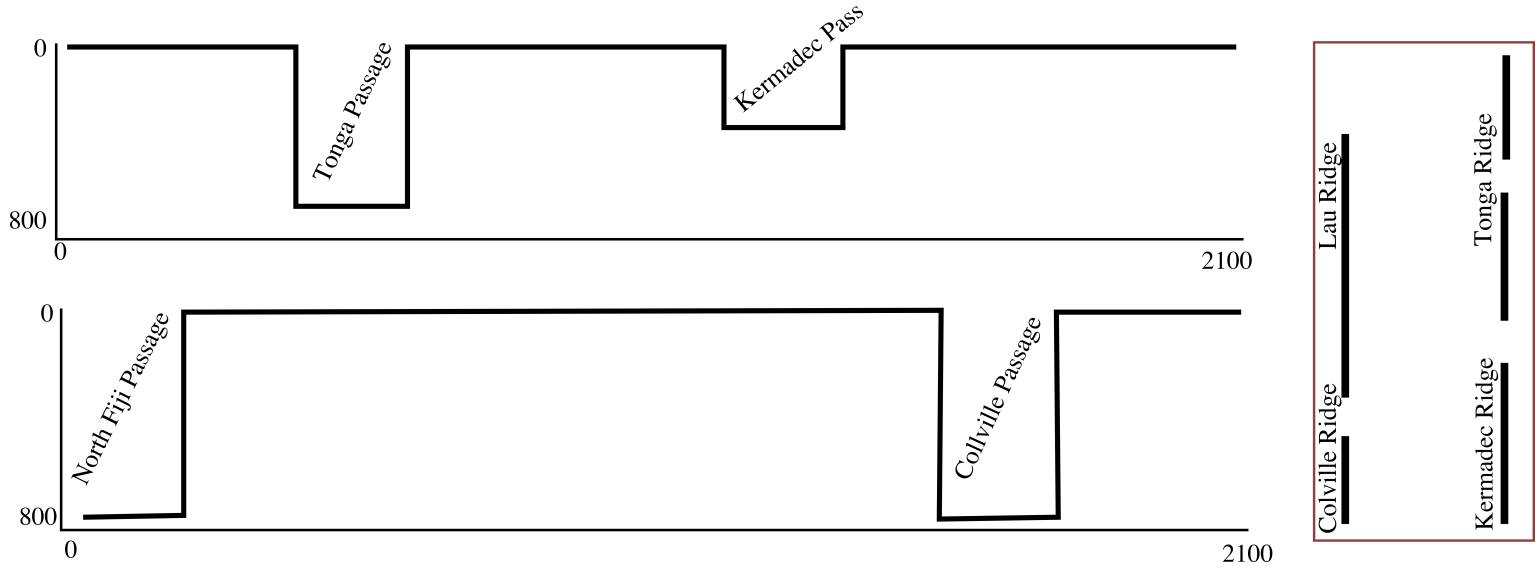

Figure 3.4: Schema of analytical model setup as it applies to the Lau Basin and Havre Trough.

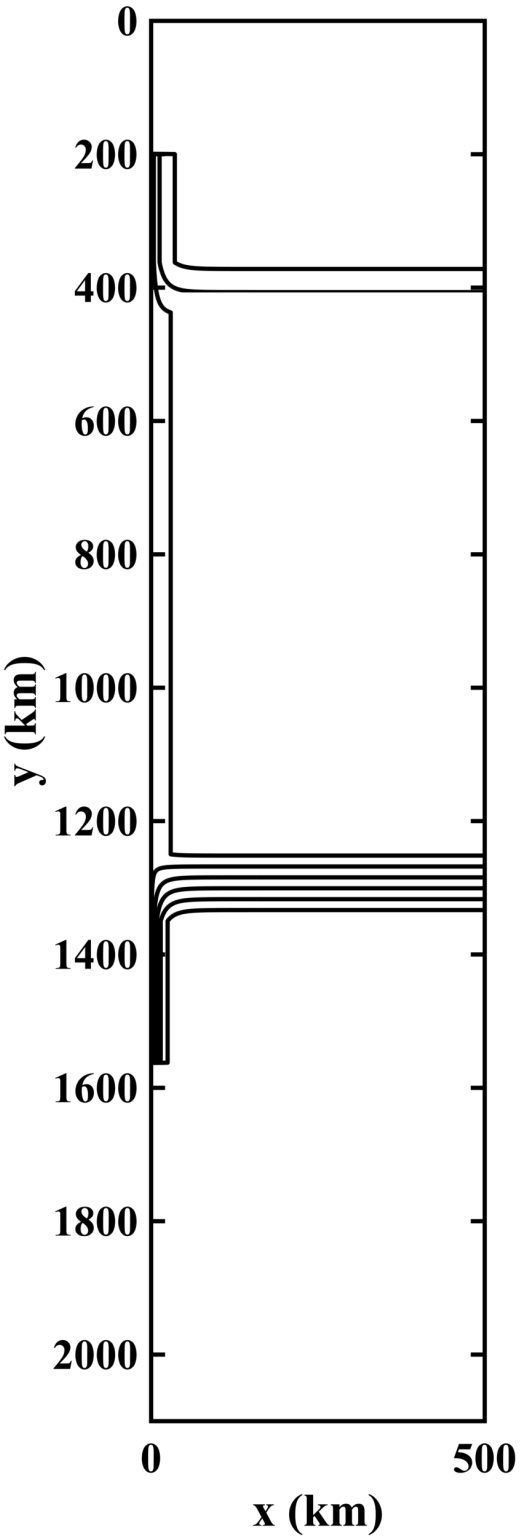

Figure 3.5: Pedlosky extension applied to the Lau Basin and Havre Trough in an idealized setting.

are not completely isolated, so the pools of each recirculation communicate with the western basin through zonal jets that flow westward through the gaps in the ridge system.

3.3 Topographic Effects: The Role of a Ridge with a Topographic Skirt

In order to ascertain the affect that topography has on flow pathways, including topographic blocking, a simple anayltical model that assumes straight, vertical walls that penetrate through the layer surface is too much of a simplification. Observations, again from float data, indicate a fairly strong f/H control of the flow along the Lau and Colville Ridges (Figure 3.6). The simple anayltical model, though appropriate for predicting the flow bifurcation, is incapable of capturing the affect of the topographic flow modulation since the topography consists of straight vertical walls.

The impacts of topography on the abyssal flow are examined by solving the steady state, geostrophic, barotropic vorticity equations with an idealized topography. Since an analytical solution is unmanageable for even relatively simple topography we appeal to numerical methods. Here, the 'Geostrophic Barotropic Vorticity Solver' (GeoBarS, 2017) is used. For integrity, Section 3.1 shows the derivation of the equations that are solved.

3.3.1 Equations Solved

For sufficiently slow moving flows, the effects of gravity waves can be approximated as instantaneous adjustments of the fluid surface that act to keep the fluid transport divergence free; the rigid lid assumption. Steady state, linear flows subject to all of the previous assumptions are now governed by two equations :

$$f\hat{z} \times \vec{u} = \nabla P - C_d \vec{u} + \vec{\tau} \tag{3.6a}$$

$$\nabla \cdot (H\vec{u}) = 0 \tag{3.6b}$$

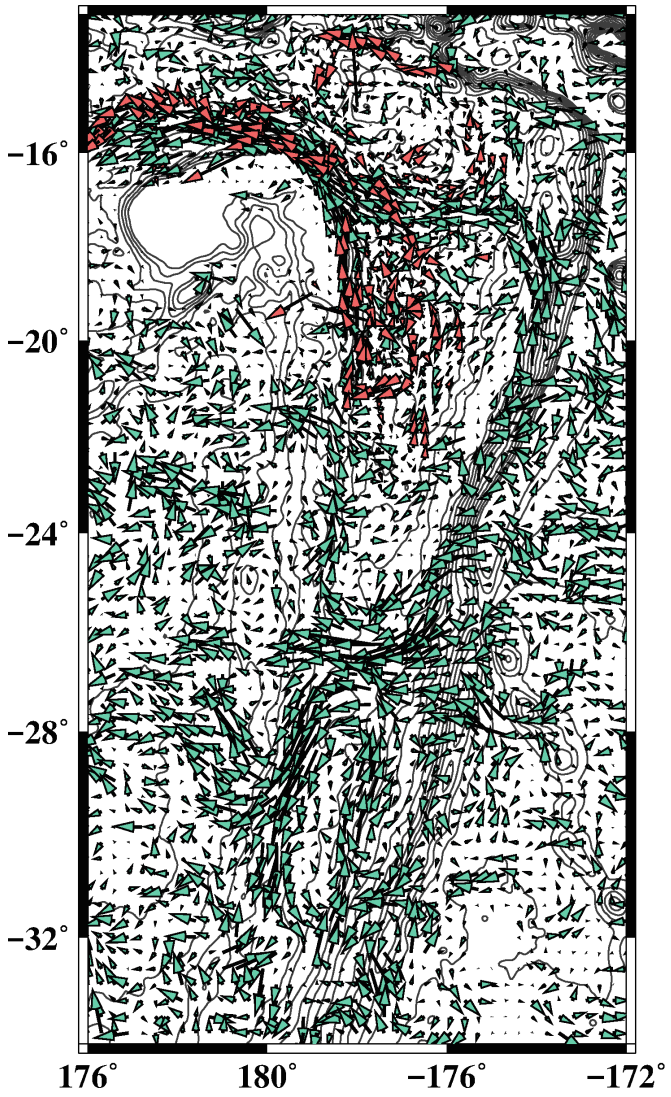

Figure 3.6: f/H contours (black) with Argo (blue) and LAUBFLEX (red) velocity overlaid.

In Equations. (3.6), f is the coriolis parameter, $\vec{u} = u\hat{x} + v\hat{y}$ is the lateral velocity field, P is the barotropic pressure per unit mass, $\vec{\tau}$ is the stress imposed on the fluid at the surface per unit mass, $C_d\vec{u}$ is a parameterization of the stress felt at the sea-floor (linear bottom drag), C_d is a drag coefficient (with units $(ms)^{-1}$, and H is the fluid thickness. Eq. (3.6b) is satisfied exactly if the transport is written in terms of the transport stream function

$$H\vec{u} = \hat{z} \times \nabla\Psi \tag{3.7}$$

Further, the equation set (3.6) can be reduced to a single equation for the transport stream function by taking the curl of (3.6a) and substituting in (3.7). Doing so gives

$$\nabla \cdot \left(\frac{C_d \nabla\Psi}{H^2} + \hat{z} \times Q\nabla\Psi \right) = \nabla \times \left(\frac{\vec{\tau}}{H} \right) \tag{3.8}$$

where

$$Q = \frac{f}{H} \tag{3.9}$$

is the background planetary vorticity.

3.3.2 Discretization and Solution Algorithm

Within GeoBarS, equation (3.8) is solved using a Nodal Continuous Galerkin Spectral Element Method [Schoonover, 2018]. Given a 2-D region of space, the domain is discretized into curvilinear quadrilateral elements. Within each element, the transport stream function is approximated by a Lagrange interpolating polynomial of degree N. The interpolation points within each element are taken to be the Legendre Gauss points of degree N. Provided the solution to (3.8) is complete (it's derivatives are defined everywhere), the error in the discrete approximation decays exponentially with N [Schoonover et al., 2015].

The details of arriving at the discrete form of the equations are not given here, but Kopriva (2009) provides a complete derivation. Ultimately, the discrete system can be expressed as a matrix system

$$\mathbb{M}\vec{\Psi} = \vec{b} \tag{3.10}$$

where $\mathbb{M}$ is not symmetric positive definite.

3.3.3 Model Configuration

An idealized topography was developed to represent the Lau and Colville Ridges, using a pre-defined maximum slope (10%), and a quadratic function for shaping the ridge (Figure 3.7). The maximum depth of the model was set to 1600m with the maximum ridge height coming within 600m of the surface (Figure 3.7). The break in the ridge is representative of the Colville Passage, while the area to the east of the ridge represents a flat-bottomed approximation of the Lau Basin and northern portion of the Havre Trough. Two westward flowing jets are initiated at the eastern boundary of the domain with equivalent outflow points on the western boundary. The western boundary of the domain was set 'far enough' away from the interior of interest so as to not influence the solution with boundary condition corrections. A variable mesh was configured with refinement centers around the topography, including the ridge break, as well as refinement centers around the the jet paths within the interior of the basin (Figure 3.8).

In order to test the sensitivity of the flow and solution to variations in chosen constants, C_{drag} was varied between 10^{-9}, 0.5×10^{-9}, and 0.25×10^{-9}, while the jet structure's initial velocity varied between 0.4 m/s, 0.8 m/s, and 1.2 m/s. Ridge height was also varied, with constant C_{drag} and jet initial velocity, to find the point where flow crossed topography.

3.3.4 Topographic Control

The resulting output from the varied runs indicates that topographic control, like that described in Pedlosky et al. (2009) , of the flow alters the solution minimally, but noticeably from the straight, vertical sidewalls of the simple analytical model (Figure 3.9). The bifurcation of flow predicted by the analytical model still exists, but the compression of streamlines following f/h in the numerical model more closely compare (qualitatively) with the observations.

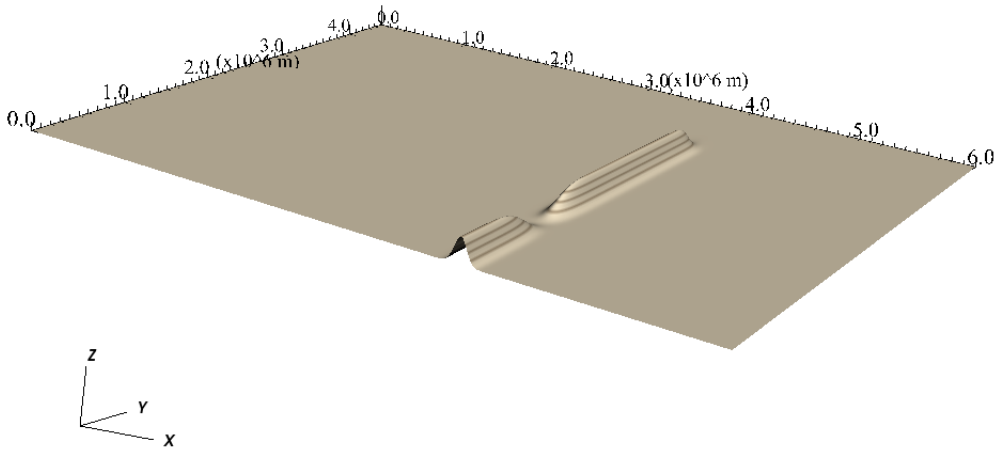

Figure 3.7: Idealized topography for the numerical run. The maximum topographic steepness is 10%. The topography is representative of the Lau and Colville Ridges found in the study area. The break in the ridges represents the Colville Passage. The area to the east of the Ridges approximates a flat-bottomed form of the interior Lau Basin and northern portion of the Havre Trough.

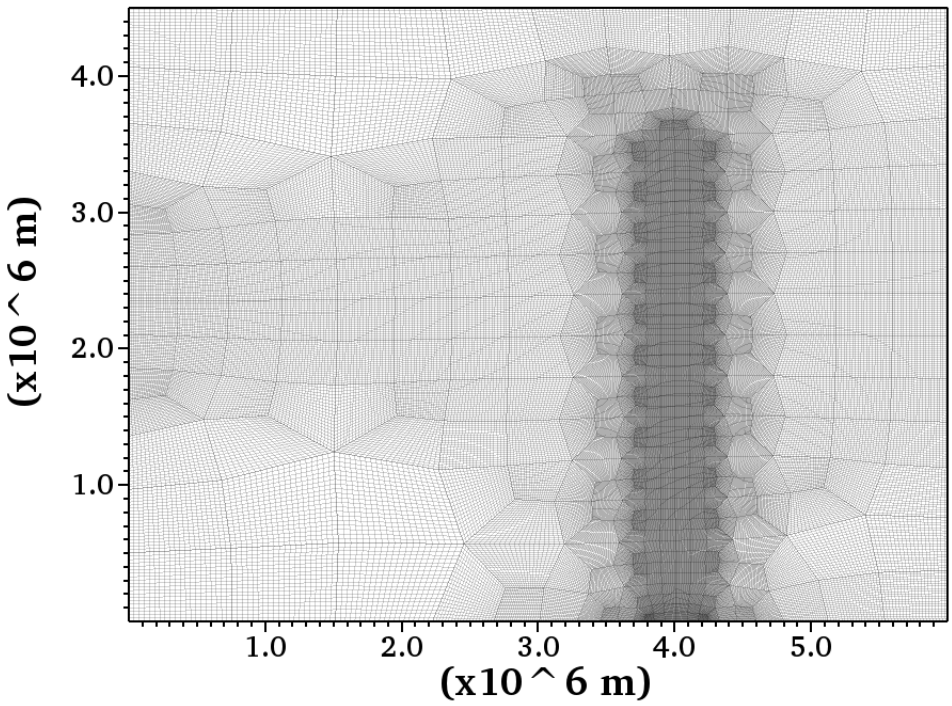

Figure 3.8: Mesh used in the numerical model runs. Refinement centers were placed around the location of the topography and the location of the pre-conditioned (iteration 0) jets to improve stability and decrease iterations for convergence.

Along the outflow region along the northern section of the idealized ridge (equivalent to the North Fiji Passage and the northern portion of the Lau Ridge) streamline compression is most noticeable, following closely with the compression of flow observed in the LAUBFLEX and Argo data. In the south, through the Colville Passage, there is a retroflection of streamlines, with a portion trying to turn northward and a portion turning southward. This is very similar to the float data, at the outflow region around 30°S, there is flow correction based on the last f/H contour the flow was connected to leading to a slight correction to try to preserve its potential vorticity. There are several differences in the northern outflow, mainly due to the shape of the idealized topography in comparison to the observed topography; ie the idealized topography does not have the 'large' landmass of Fiji attached to the northern portion of the Lau Ridge which helps to maintain the jet-like structure of the outflow region into the North Fiji Basin.

When C_{drag} is varied, the result is a widening or narrowing of the $\triangle$x coverage of the DWBC as well as the spread of the incoming jets. When the incoming jet velocity is varied, the topographic control of the flow doesn't change, rather by definition the difference lies in the magnitude of the transport through the denoted passages (See Appendix A.1 and A.2).

3.3.5 Topographic Blocking and Crossing

Finding the condition for when topography impacts a flow, ie topographic blocking can be done using a scaling argument:
Starting with the Jacobian form

$$J(\psi, \frac{f}{H}) = C_{drag}\nabla^2\psi \tag{3.11}$$

expanded becomes:

$$\frac{\beta\psi_x}{H} + \frac{f\psi_y H_x}{H^2} = C_{drag}\nabla^2\psi \tag{3.12}$$

where ψ is the stream function with ψ_x and ψ_y representing the velocity components, assuming a divergence free fluid. H is the total water depth and H_x is the effective slope of

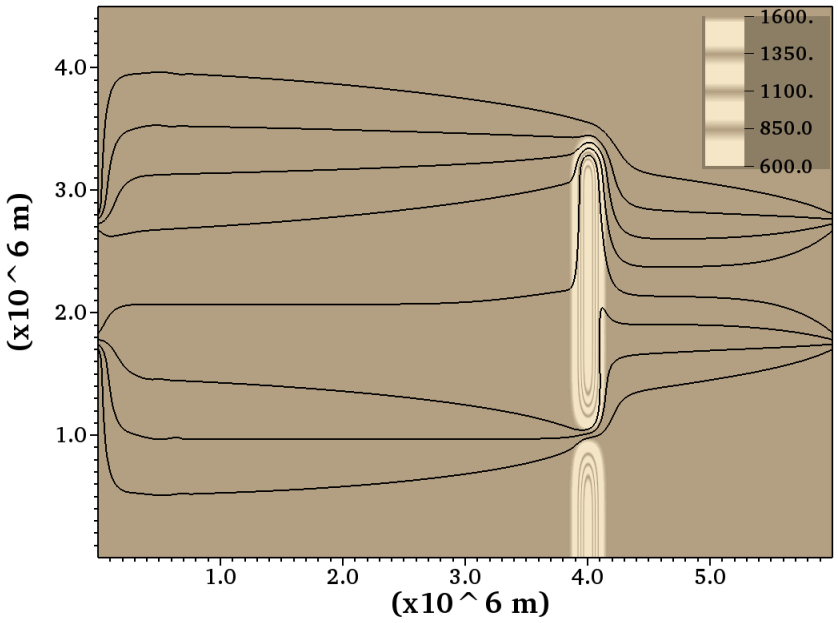

Figure 3.9: Output from numerical run with an effective bottom drag of $0.5 * 10^{-9}$. The topographic control on the flow patterns is evident, with topographic trapping both along the northern outflow (North Fiji Passage) and within the interior along the western boundary where the flow bifurcation occurs.

the topography. Assuming that $L_x << L_y$ Scaling each term of Equation 3.12 ;

$$\overbrace{\frac{\beta}{HL_x}}^{\text{Advection of planetary vorticity}} \qquad \underbrace{\frac{f\triangle H}{HL_xL_y}}_{\text{Vortex stretching}} \qquad \overbrace{\frac{C_{drag}}{L_x^2}}^{\text{Stommel Boundary Layer}} \tag{3.13}$$

where L_x is the width of the ridge, L_y is the width of incoming jet, and $\triangle H$ is the height of the ridge.

Looking for the largest term to balance the vortex stretching term, we find that the scale for there to be topographic blocking depends on the Stommel Boundary Layer more so than the advection of planetary vorticity. According to the scaling analysis, for this particular problem, topographic blocking will occur as long as $\triangle H > \mathbb{O}(100m)$. Below this, there is no guarantee that the topography will have any control over the flow.

Varying the topographic maximum height within the GeoBarS runs supports the scaling argument (Figures 3.10, 3.11, 3.12, and 3.13). Starting at the full height topography (1000m), the flow is completely blocked from crossing over the ridge, and instead is directed around the topography towards the passages along the ridge. As the ridge height decreases the streamlines become less confined to the ridge, though f/H corrections (seen as oscillations and meanders in the streamline paths) maintain the effect of topographic blocking with a majority of the flow still directed towards the passages. There appears to be a critical point in ridge height for strong topographic blocking, with a transition occurring below 500m (Figure 3.14), where though there is still topographic control of the flow, topographic crossings become more regular.

3.4 Discussion

The simple analytical model goes a long way in describing the dynamics of the DWBC flow along the the Lau and Colville Ridges as well as the interior westward jets that feed the observed DWBC. Expanding the model again to include a topographic skirt further refines the flow patterns, especially around the outflow passages (North Fiji Passage and Colville

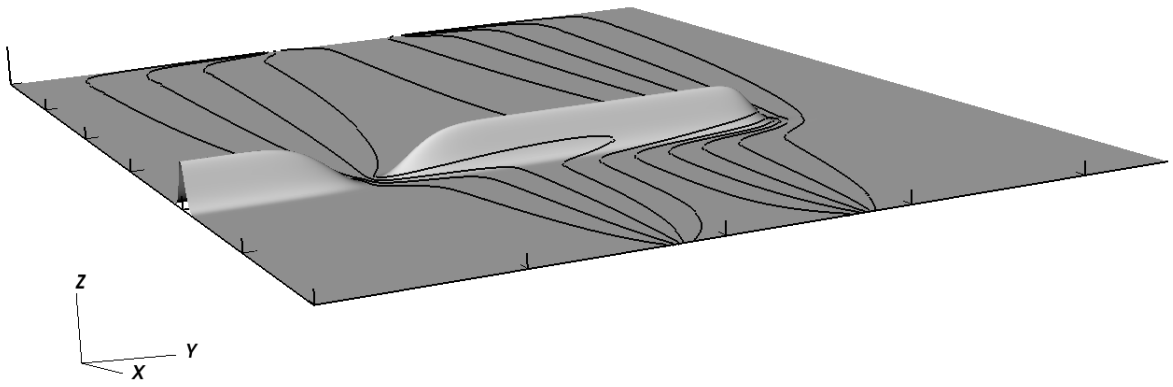

Figure 3.10: 3d view of flow with full height topography ($\triangle H = 1000$m)

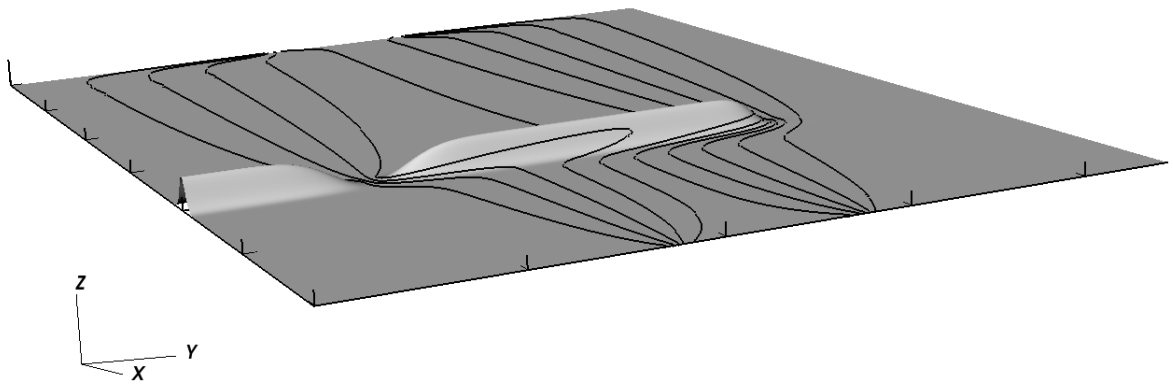

Figure 3.11: $\triangle H = 700$m, flow field is starting to encroach on the hill but is correcting to f/h.

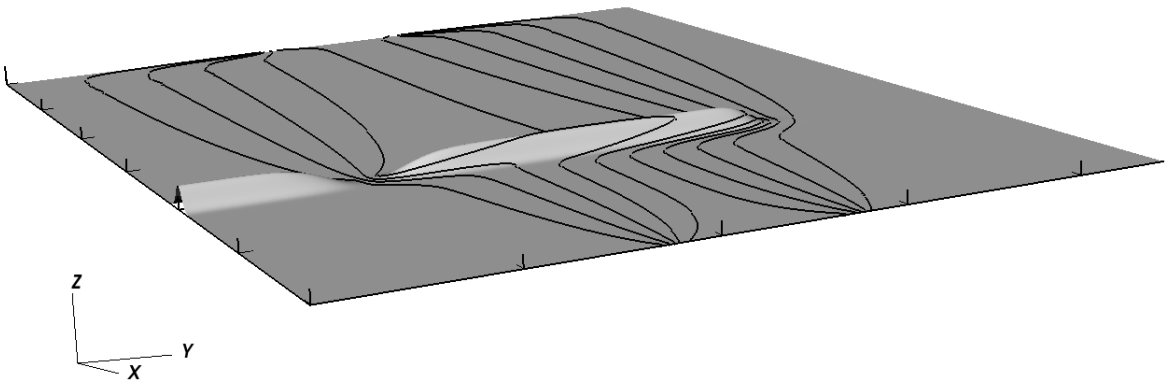

Figure 3.12: $\triangle H = 500$, starting to get into the transition zone where f/h is having less control over the flow. Full topographic blocking is starting to break down.

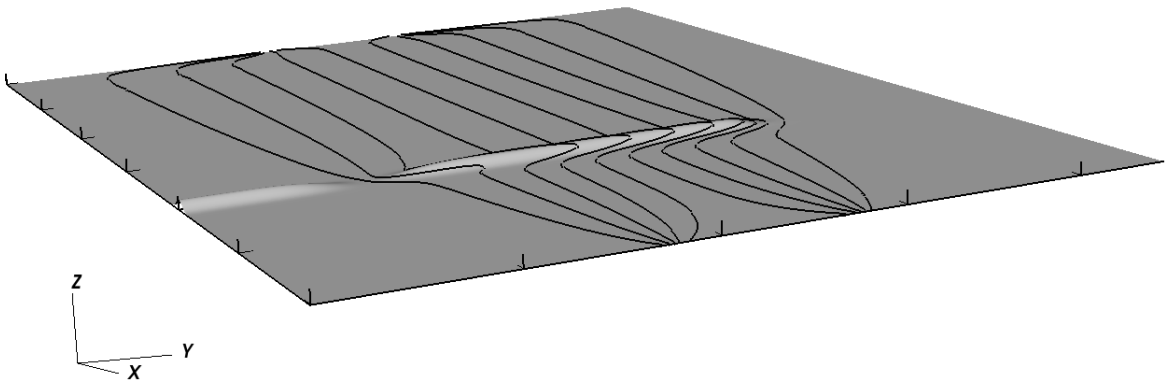

Figure 3.13: $\triangle H = 200$. There is still some topographic control of the flow, though about 40% of the streamlines make it over the ridge.

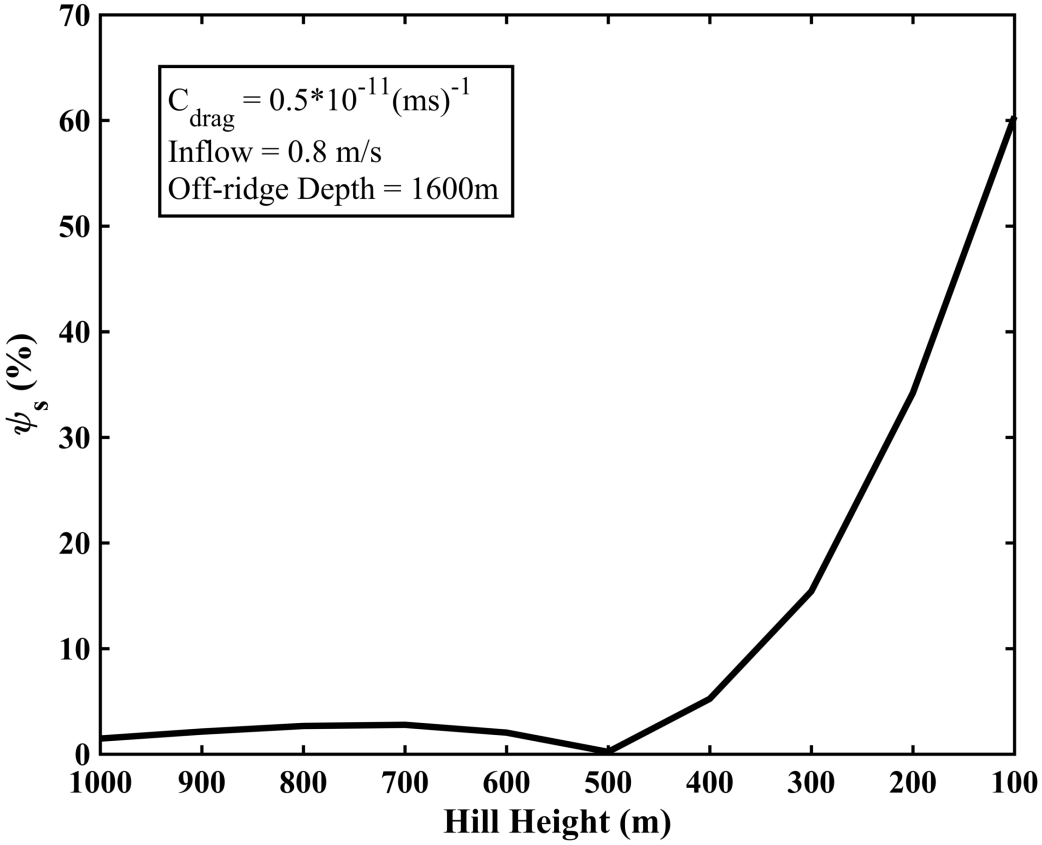

Figure 3.14: Line plot showing the crux point for topographic blocking vs. ridge height. Y axis shows percentage of streamlines that cross the ridge.

Passage) where streamline compression due to tightening f/H contours is most evident in observations.

We know that the real ocean is stratified and through a large portion of the South Pacific there is a high amount of variable topography, so the main question becomes how the simple analytical model proposed by Pedlosky can describe the dynamics in the Lau Basin and Havre Trough so well. It is a barotropic, homogenous, single layer model that predicts accurately the major dynamics of flow observed in the Lau Basin, including the behavior of flow through 'gappy' ridges, the location of the flow splitting and the ratio of the transport that turns north vs. the transport turning south. Even the numerical model that takes into account topographic skirting is a simplified, barotropic, homogenous model.

We can argue that the dynamics of variable topography in a stratified fluid can mimic that of no-normal flow, homogenous fluid under the right set of conditions following the steps outlined in Rhines (1970) and Chapman & Rizzoli (1989) . Boundary dynamics along the topography are controlled by the combination of the Burger number ($S = \frac{HN}{f_0 L}$) squared and the ratio between the topographic slope and the total aspect ratio for the basin ($\delta = h_x / \frac{H}{L}$): $S^2\delta$. If H, L are given, we are freed to modify h_x and N^2. So the original question of how a straight-walled, homogeneous model can be so accurate is answered through dynamic similarity (See Appendix B for derivation).

In a straight wall, homogeneous set-up: $h_x \to \infty$, $N^2 \to 0$ is the Pedlosky model. If the balance of $h_x N^2$ is similar between the 'real world' and the simple model, the dynamical behavior should be similar as well, resulting in flow behavior that is familiar. Within the Lau Basin a typical N^2 value is between $10^{-6}\frac{1}{s^2}$ to $10^{-7}\frac{1}{s^2}$ below 1000m. With a very large h_x of 10%, this yields an $N^2 h_x$ of $10^{-8}\frac{1}{s^2} \to 10^{-9}\frac{1}{s^2}$ which $\to 0$ arguing that vertical velocity is suppressed resulting in a balance that is similar to that of a vertical walled model.

CHAPTER 4

LAU BASIN AND HAVRE TROUGH CONNECTIONS TO SOUTH PACIFIC SUB-BASINS

4.1 Introduction

Results in *Chapter 2: Abyssal Circulation in the Lau and Havre Trough* raised questions related to the role of the Tonga Passage to the Lau Basin (Figure 4.1). Argo float displacements indicated a flow into the Lau Basin through the Tonga Passage, though with no clear certainty in how the Lau Basin was being filled. This was further complicated with the observation of flow into the basin, that was linked to a recirculation region connecting the outflowing DWBC along the North Fiji Passage to an inflow region located further northeast, introducing flow to the central portion of the Northern Lau Basin. From hydrographic section P21 (which runs nominally along 17.5S), below the northern jet stemming from the Tonga Passage, there was indication that the Tonga Passage supplies the intermediate water, but was less clear on a deep water source.

The source of deep water into the Havre Trough was answered in Ch.2, originating in the South Fiji Basin and entering through a deep ridge break at 32°S, validating Wrytki's (1970) intuition of flow in the South Fiji Basin and eastward. The intermediate waters (1000-2000m) are assumed to be supplied through the Kermadec Passage. The Havre Trough has connections to the Lau Basin through the effect of a flow bifurcation along the Colville Ridge, where a portion of an impinging jet is turned northward. Observed circulation in the area gives no indication that there is any more than this one-way communication between the basins.

In this chapter we explore the role of the ridges (Lau, Colville, Tonga, and Kermadec) and their respective passages in the import and export of waters through the Lau Basin and Havre Trough (Figure 4.2). We also seek to explain the sources supplying the deep and mid-depth layers of both sub-basins.

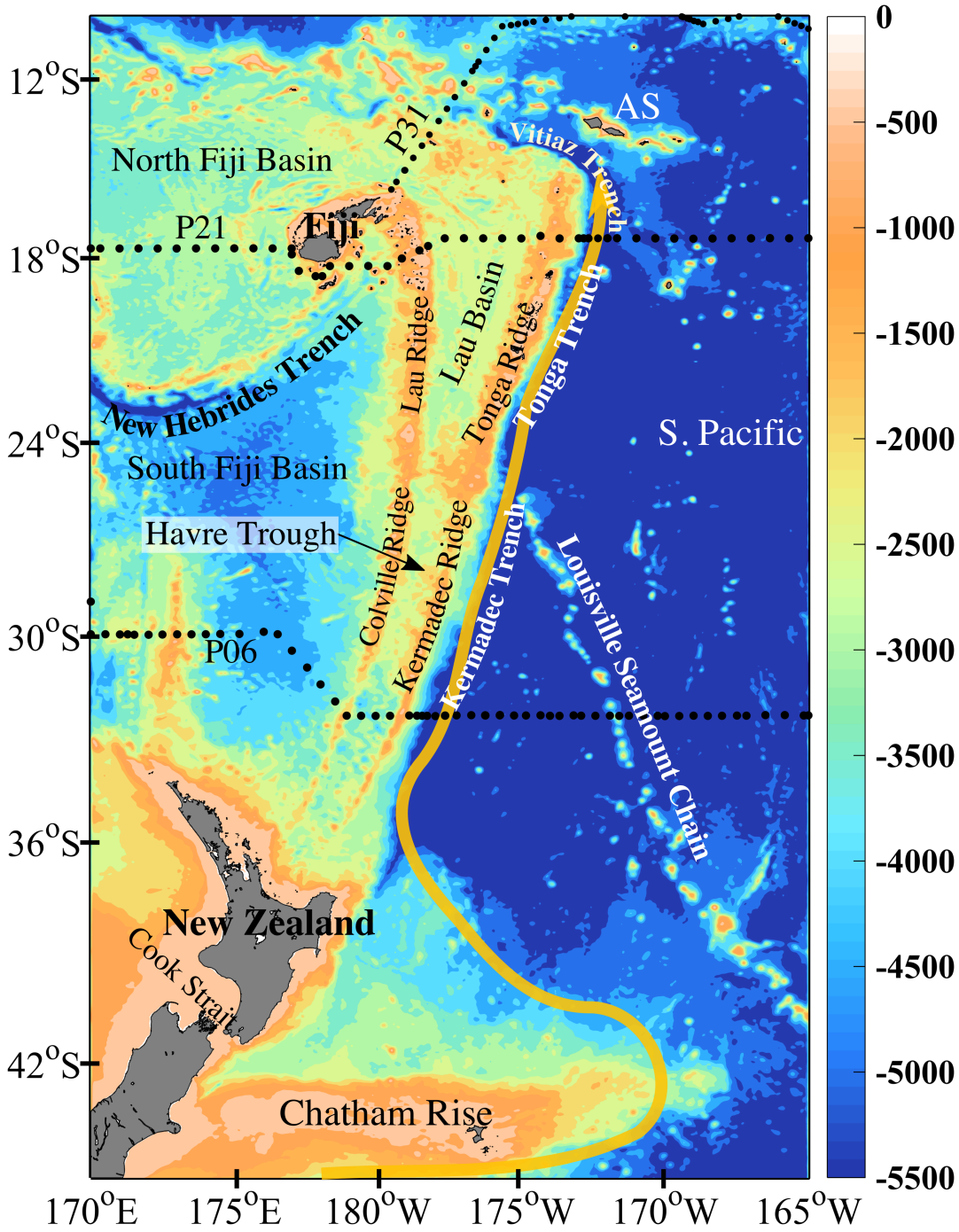

Figure 4.1: Map of the Lau Basin and Havre Trough. The ridge systems associated with the boundaries have been labeled, as well as salient geographic features. The yellow line along the Tonga and Kermadec Trench schematically shows the route of the DWBC as discussed in Whitworth (1999). AS = America Samoa.

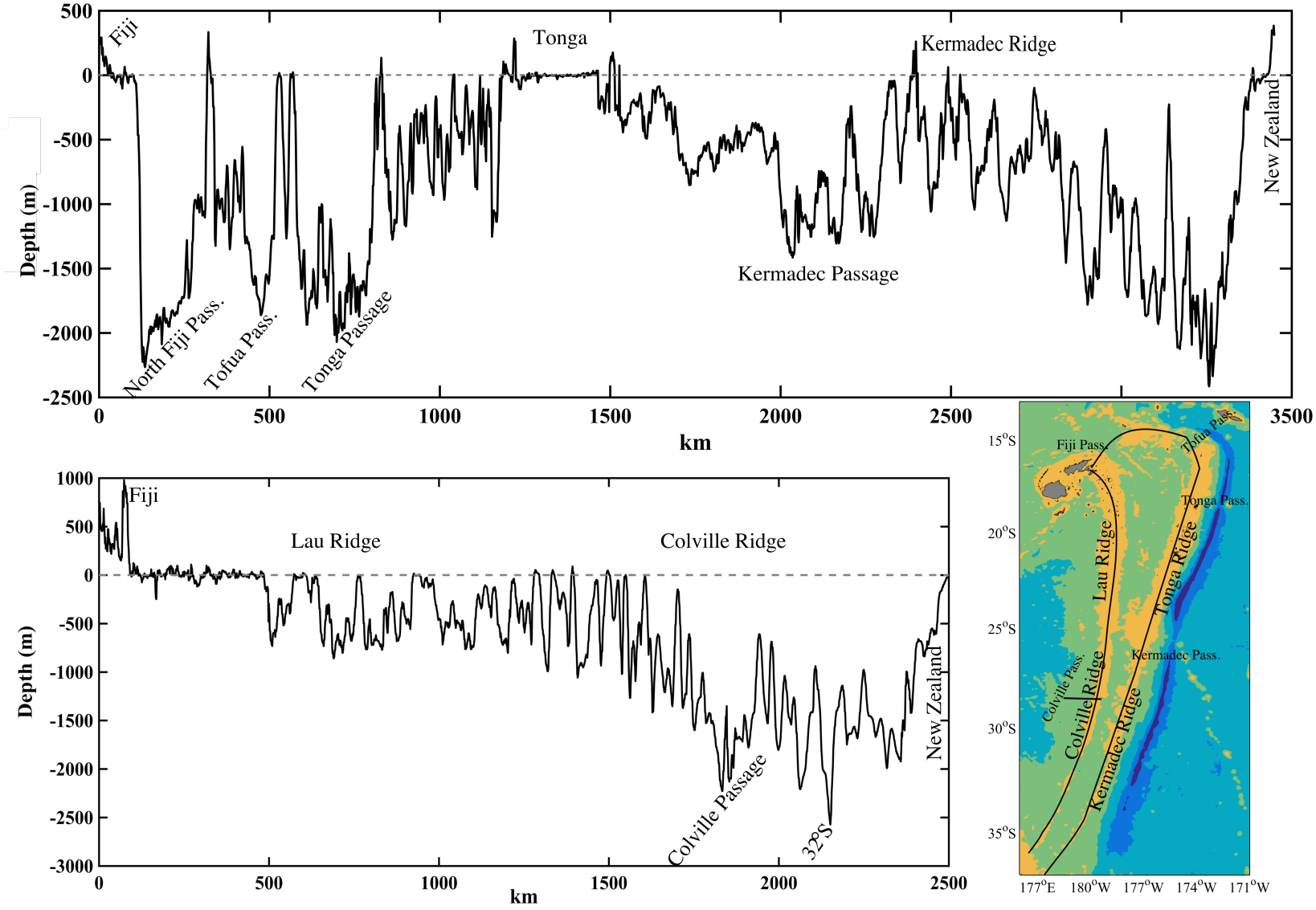

Figure 4.2: Sill depths along the study area. Subset map shows the full study area with ridges and passages labeled for reference.

4.2 Data

4.2.1 Argo Profiles

Argo floats, beyond measuring displacement at a nominal depth, profile the water column during each cycle. Typically a float will drift nominally at 1000m before descending to between 1500m and 2000m to begin an upwards profile of the water column. The descent depth is dictated by the initial programming of the Argo float, but is metered by the local topography where the Argo float finds itself.

The majority of floats measure temperature (T), salinity (S), and pressure (P) with more recent models branching out to oxygen and other biogeochemical measurements. Within this study, the large majority of floats ($> 90\%$) only sample T, S, and P. The accuracy of the sensors have improved with time. Temperature ranges from (0.002°C - 0.005°C) depending on the float type. Specifics about float type were discussed in Chapter 2: Abyssal Circulation in the Lau Basin and Havre Trough, Section 2.2. Salinity sensors at the beginning of the Argo program had an accuracy around $0.01 mS/cm$, this has improved to 0.005 mS/cm. Pressure measurements are accurate to within 2.4db, with some very early floats having a 5db hysteresis error [Boyer et al., 2013].

Errors in the measurements can come from two points. The first being sensor problems, primarily salinity drift. Oka (2005) estimated an average salinity sensor drift from recovered Argo floats of -0.016$\pm$0.006mS/cm per year. Several algorithms have been developed to correct for the salinity drift and abrupt calibration deviations. Delayed mode Argo data are corrected for this drift, using one of the developed algorithm. The second point of error comes from transmission issues. Floats that used the ARGOS transmission system had higher occurrences of missed or broken packets [Boyer et al., 2013], due to longer surface stays. Originator flags are attached to each observation which takes into account potential sensor and transmission errors. For this study any data attached to a flag >2 (2: Likely

good data, 3+: bad data) were set to an undefined value.

Throughout the Lau Basin, Havre Trough, and the surrounding ridge systems 8326 distinct profiles were taken by the Argo floats over 14 years from July 2001 to June 2015.

4.2.2 Hydrographic Data

Traditional shipboard hydrographic data in the Lau Basin and Havre Trough consists of repeat occupations along three sections, P31, P21 and P06. P21 runs through the Lau Basin, nominally along 17.5°S, while P31 runs from Fiji northeast through the Samoan passage. P06 transects the southern portion of the Havre Trough, nominally along 32.5°S. A full discussion of each line is found in Chapter 2: Abyssal Circulation in the Lau Basin and Havre Trough, Section 2.4.

The CTD (conductivity, temperature, and depth) data from the hydrographic lines was processed using only data flagged as the most confident. Any values outside of the acceptable range were set to an undefined value and interpolated across using a Laplacian filter. Sensor accuracy associated with the CTD is more accurate than that associated with the Argo floats. The temperature sensor is accurate to 0.001°C. Salinity is accurate to $0.003 mS/cm$, and pressure is reported as accurate to 1.5db [Murata and Uchida, 2009].

4.3 Tonga and Kermadec Ridges and Passages

The Tonga and Kermadec Ridges act as the eastern boundaries to the Lau Basin and Havre Trough respectively. The Tonga Ridge system is bordered at its northern point by the Vitiaz Trench, a continuation of the Tonga and Kermadec Trenches. The majority of the nothern portion of the Tonga Ridge is below 1000m. South of the Tonga Passage the ridge becomes more shallow, acting as a barrier below 750m. Once the ridge system transitions to the Kermadec Ridge, the sill depths drop on average below 1500m with breaks as deep as

2500m at the southern end of the ridge system.

Along the Tonga and Kermadec Ridges 467 profiles were used for the analysis. The majority of the Argo float profiles ($> 65\%$) on the Tonga Ridge and the Kermadec Ridge profiled depths between 1000m and 1500m with deeper profiles (2000m) within the Tonga Passage and along the Kermadec Ridge. Geostrophic velocities were estimated from the Argo profiles referenced to the 1000m float velocities.

In Chapter 2, the circulation inferred from Argo floats (nominally 1000m) and Lau Basin Float Experiment (LAUBFLEX) floats (nominally 1700m) indicated inflow at the Tonga Passage and the Kermadec Passage which are situated along the Tonga Ridge and Kermadec Passage respectively. The Tonga Passage is the most northern passage along the Tonga Ridge and is the widest ($\sim$200km) and deepest passage ($\leq$2000m) observed along the eastern boundary of the Lau Basin and Havre Trough. The Kermadec Passage is the southernmost passage on the eastern boundary of the Havre Trough. Existing at the north-end of the Kermadec Ridge, the passage is the shallowest (1500m) of all of the passages observed along the Lau Basin and Havre Trough region.

The float profiles indicate a persistent westward flow through the Tonga Passage (Figure 4.3A) below 1000m, with a similar westward signal through the Kermadec Passage. Weaker westward flow through other breaks in the Kermadec Ridge appear as well. There is also an indication of a potential deep westward flow around the northern end of the North Island of New Zealand (around 2000km). Temperature is the apparent controlling term for the density and the geostrophic velocity(Figures 4.3B, C, and D), with the lowest potential temperature recorded by the Argo floats 2.3°C.

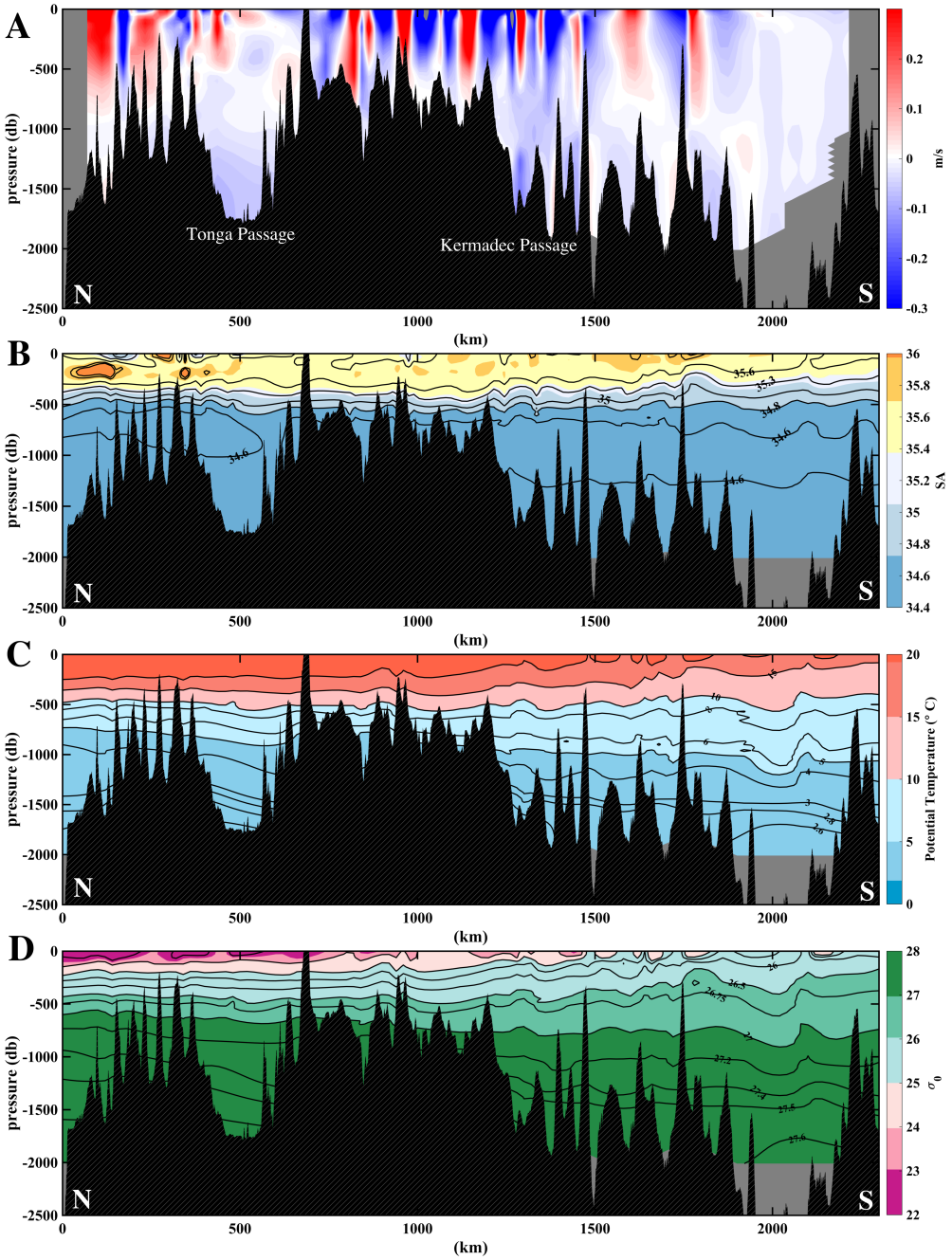

Figure 4.3: Property plots from Argo float profiles over the Tonga and Kermadec Ridges. A) Geostrophic velocity derived from Argo float profiles and referenced to the Argo velocity at 1000m. B) Absolute Salinity. C) Potential Temperature. D) Density σ_θ

4.4 Lau and Colville Ridges and Passage

The Lau Ridge behaves as a solid boundary penetrating to the surface over a large area (500km), with the northern 1200km extent shallower than 1000m (Figure 4.4) forming the northern portion of the western boundary to the Lau Basin and Havre Trough. The southern portion of the western boundary, the Colville Ridge, is exceptionally gappy and steepens quickly toward the Colville Passage ($\sim$ 2000m). South of the Colville Passage along the Colville Ridge was found to have a region of deep (below 2000m) inflow into the Havre Trough at 32°S that the Argo profile data can not illustrate (Figure 4.2) through a sill break deeper than 2500m.

Along the Lau and Colville Ridges 213 Argo float profiles were used. Fewer profiles were available on the Lau and Colville Ridges due to the ridge heights associated with the Lau Ridge system. Profile depths were restricted to the upper 750m until about 1600km. Floats descended to 2000m whenever the topography allowed. Similar to the Tonga and Kermadec Ridge profiles, geostrophic velocity estimates were referenced to the 1000m Argo float velocity.

Geostrophic velocity estimates along the Lau Ridge indicate strong, countering flows trapped to steep ridge breaks in the upper 750m (Figure 4.4A). Deep ridge breaks do not occur until the Colville Passage at which point a relatively weak westward flow is observed below 1000m, weakening even more below 1500m. The ridge break at 32°S is not shown. As with the Tonga and Kermadec Ridge profiles, potential temperature controls the density (Figures 4.4B, C, and D) with the lowest temperature (2.2°C) occurring in the Colville Passage.

4.4.1 North Fiji Passage

The North Fiji Passage connects the Lau Basin to the North Fiji Basin through a fairly deep (>2000m) passage and is the terminus of the Lau Ridge system. The majority of flow through the passage comes from the northward flowing DWBC that hugs the Lau Ridge

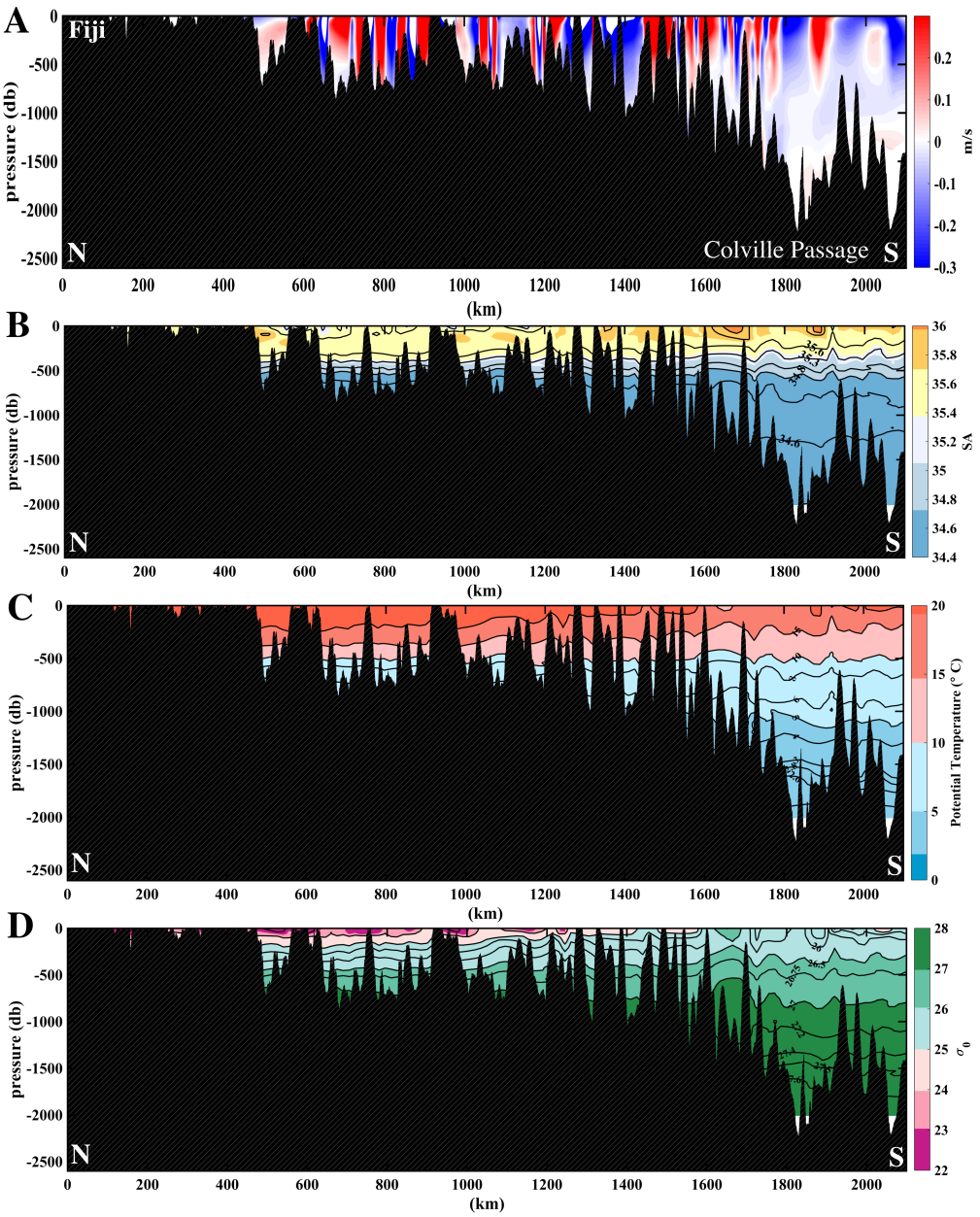

Figure 4.4: Property plots from Argo float profiles over the Lau and Colville Ridges. A) Geostrophic velocity derived from Argo float profiles and referenced to the Argo velocity at 1000m. B) Absolute Salinity. C) Potential Temperature. D) Density σ_θ

within the Lau Basin. Northeast of Fiji, the topography is complicated but relatively deep (below 1000m) until the Samoan Passage (far north of the study area).

Float based circulation in this area indicated a strong northwest outflow into the North Fiji Basin fed from the DWBC in the Lau Basin. Geostrophic velocity estimates from the 109 Argo profiles are in agreement with a northwestward flow below 1000m through the N. Fiji Passage (Figure 4.5). The width of the flow is also in agreement with the observed DWBC width (∼50km) from floats and traditional hydrographic data observations. Just north of the outflowing DWBC, there is a narrow region of inflow present in the profile data, which also agrees with observations in the float data and hydrographic data (See Chapter 2, Section 2.7).

4.5 Transport

Transport derived from geostrophic velocity estimates (referenced to Argo velocity at 1000m) is compared against estimates taken from the float displacements in Chapter 2. Transports were estimated in the same way as the traditional hydrographic derived transports in Chapter 2. The velocity was integrated over 2m vertical increments and laterally across the passage.

The profile derived transports are on average 1Sv larger than the float derived transports (Table4.1). A partial reason for this disparity is the float displacements use a single vertical layer of 700m and an averaged velocity from the Argo floats and the LAUBFLEX floats. These float averaged velocities are smaller than the geostrophically estimated velocities, and fall short (vertically speaking) of the depths represented in the profile data by 300m in some cases. There is one passage where the reverse is true, and the profile derived transport is smaller than the float displacement data. This occurs at the North Fiji Passage, and appears to underestimate the outflow transport into the North Fiji Basin. Float displacement data estimated 3.9Sv ±1Sv, while traditional hydrographic data in the area (P31) estimated 5.6Sv ±1Sv outflow from the Lau Basin into the North Fiji Basin. Velocities associated

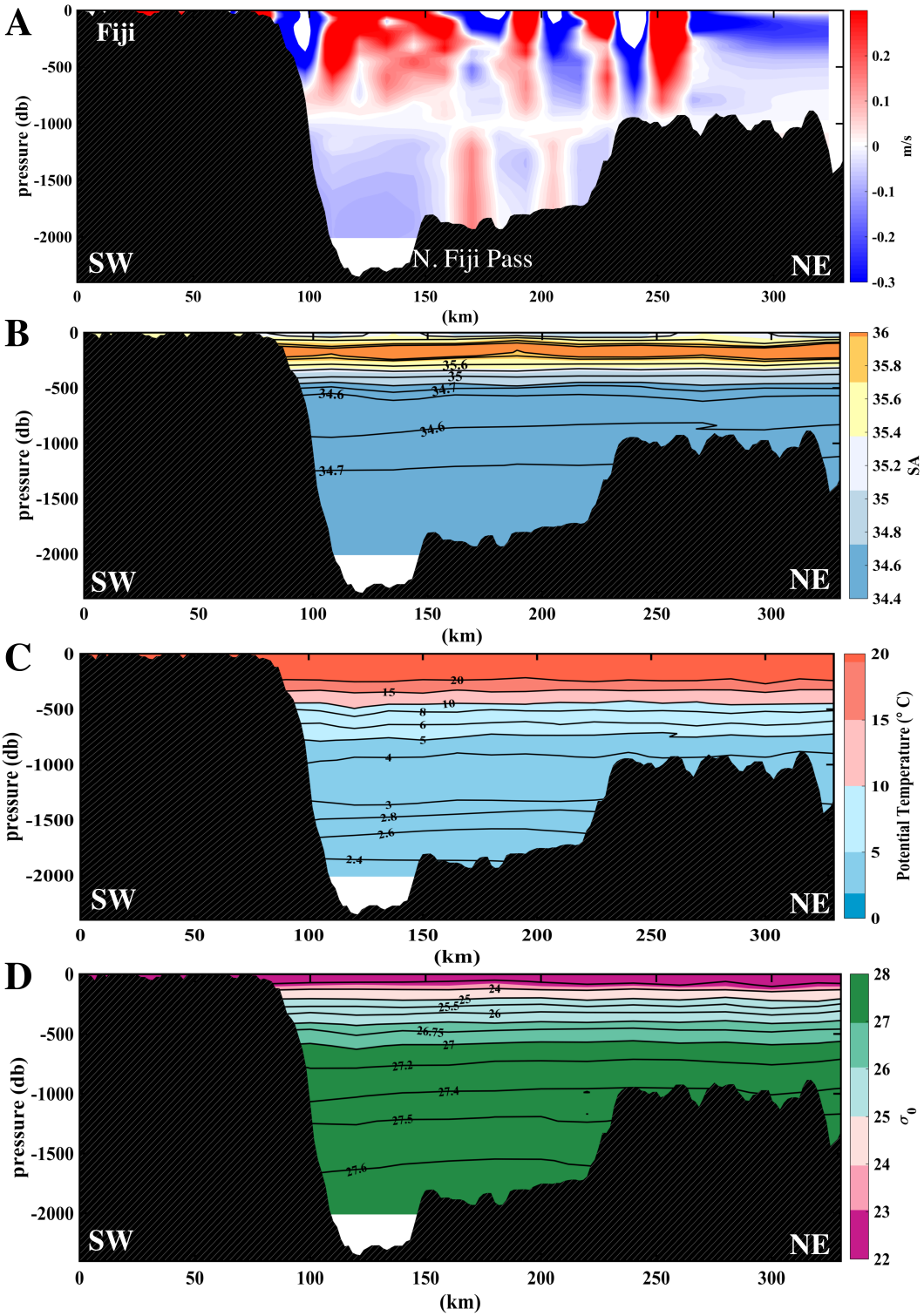

Figure 4.5: Property plots from Argo float profiles over Fiji and the North Fiji Passage. A) Geostrophic velocity derived from Argo float profiles and referenced to the Argo velocity at 1000m. B) Absolute Salinity. C) Potential Temperature. D) Density σ_θ

Table 4.1: Estimated transports through each of the passages derived from geostrophic velocity estimates from float profiles (Hydrographic) and velocity estimates within a layer thickness from Argo float and LAUBFLEX displacements (Float).

	Hydrographic	Float
Tonga Passage	-3.2Sv ±1Sv	-2.3Sv ±1Sv
Kermadec Passages	-3.9Sv ±1Sv	-1.5Sv ±1Sv
N. Fiji Passage	-2.9Sv ±1Sv	-3.9Sv ±1Sv
Colville Passage	-2.7Sv ±1Sv	-1.3Sv ±1Sv

with the Argo and LAUBFLEX floats are much larger in this area ($\sim$ 10cm/s) than along other passages ($\sim$ 4-5 cm/s) and geostrophic velocity estimates from P31 are also large, in agreement with the float velocities (See Figure 8A in Chapter 2).

4.6 Lau Basin and Havre Trough Connections

The sources for the waters filling the Havre Trough have been addressed in Chapter 2. It was found that the abyssal waters of the Havre Trough were being supplied by the South Fiji Basin (Chapter 2, Figure 6). The entrance route for this source is most likely through the deep ridge break on the Colville Ridge at 32°S. The intermediate water in the Havre Trough appears to originate to the eastern of the Kermadec Ridge and enter the Havre Trough through the Kermadec Passage. The T-S properties associated with the Kermadec Passage (inflow to the Havre Trough) and Colville Passage (outflow to the South Fiji Basin) are fairly similar (Figure 4.7).

Sources of water into the Lau Basin are less obvious than those into the Havre Trough. T-S properties show a difference in waters entering the Lau Basin through the Tonga Passage and what is exiting the Lau Basin into the North Fiji Basin through the North Fiji Passage (Figure 4.6). Potential sources into the Lau Basin are from the North Fiji Basin to the west, the DWBC and the eastern South Pacific to the east, the pre-Samoan plain to the north, and the Havre Trough to the south (Figure 4.7). It appears that the intermediate water source enters the Lau Basin from the Tonga Passage. The deep water into the Lau Basin resembles

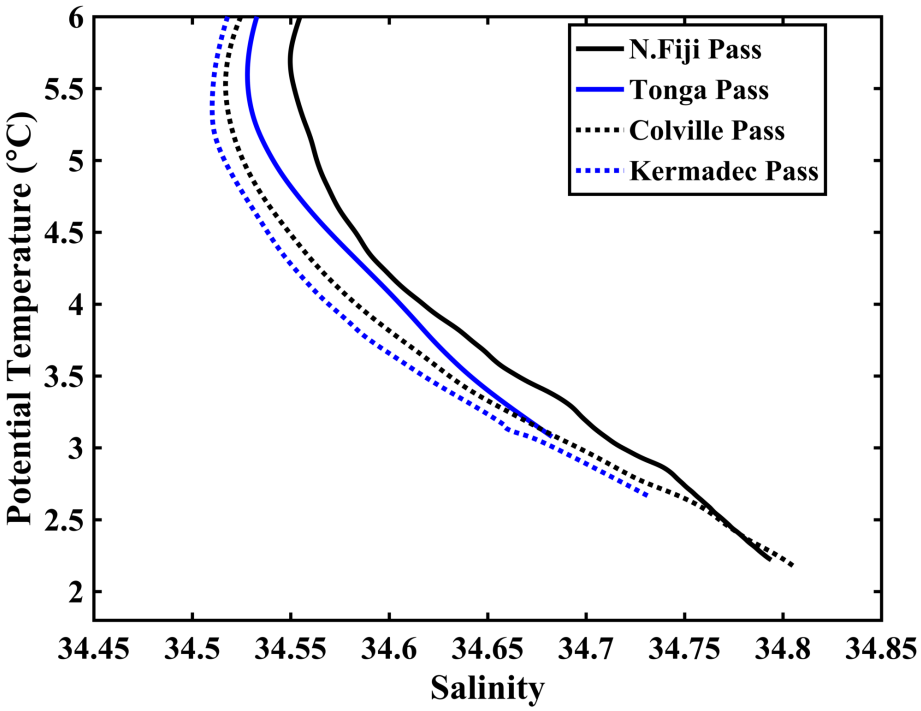

Figure 4.6: T-S of the four passages (Tonga, Kermadec, North Fiji, and Colville). Dashed lines indicate passages around the Havre Trough, solid lines indicate passages around the Lau Basin. Blue is incoming, black is outgoing.

the Samoan Passage properties and deep water found in the North Fiji Basin (Figure 4.8). One potential point of entry into the Lau Basin of this water is the region of inflow noted just north of the N. Fiji Passage. Due to the shared properties with the Samoan Passage water, which originates in the DWBC along the Tonga and Kermadec Trench, another potential passage into the Lau Basin of this water is along the minimally mentioned Vitiaz Trench and Tofua Passage in the northeast corner of the Lau Basin at the northern extent of the Tonga Ridge.

4.7 Conclusions

The Tonga and Kermadec Ridges, a set of gappy ridges acting as the eastern boundary to the Lau Basin and Havre Trough, restrict flow into these sub-basins primarily through the Tonga Passage and Kermadec Passages. The geostrophic velocity estimates from Argo

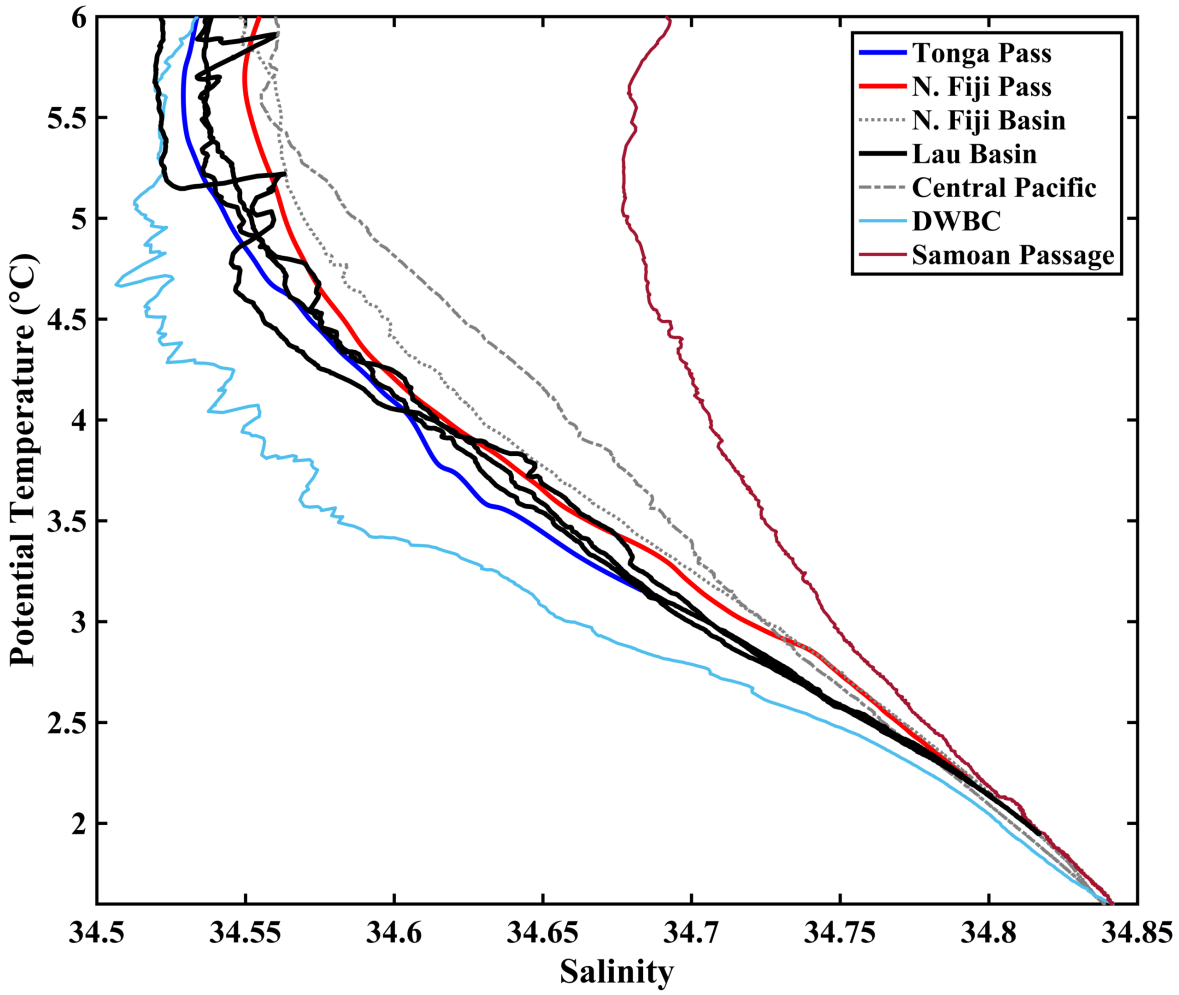

Figure 4.7: T-S diagram of Tonga Passage, North Fiji Passage, the Lau Basin with comparisons to external South Pacific basins.

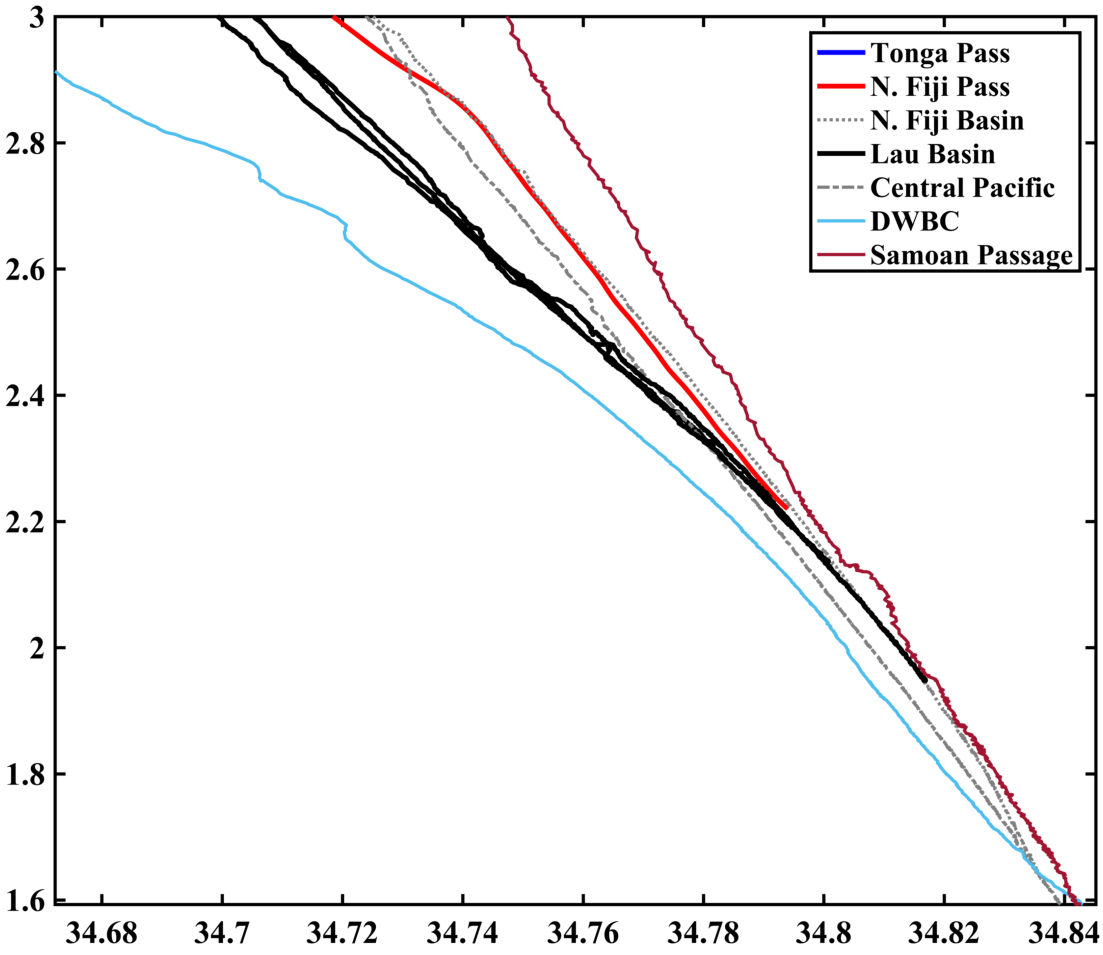

Figure 4.8: Same as Figure 4.7, with empahsis on T-S relationships below 3°C

profiles provide a consistent picture of westward flow through the Tonga Passage and Kermadec Passage with other observations. These two passages act to supply the intermediate water to the Lau Basin and Havre Trough respectively.

On the western boundary of the Lau Basin and Havre Trough, the Lau Ridge acts as a barrier to free communication between the Lau Basin and the North Fiji Basin, funneling instead the northward flowing DWBC to the North Fiji Passage. The Colville Ridge, with deeper, and more frequent ridge breaks than the Lau Ridge provides communtication between the Havre Trough and South Fiji Basin through two prominent ridge breaks, the Colville Passage and at 32°S.

The role of the passages to the import and export of waters in the Lau Basin and Havre Trough are not as clear cut as the float trajectories would imply. The Colville Passage was originally anticipated to be the one way source of communication between the Havre Trough and South Fiji Basin, as the southward flowing DWBC along the Colville Ridge exited into the South Fiji Basin at this point. From hydrographic data though this was shown to not be the case, with 32°S providing a ridge break for deep water from the South Fiji Basin into the Havre Trough. From the Argo profile data, it appears that though the deep water is supplied into the Havre Trough at 32°S, the mid-depth is supplied through the Kermadec Passage.

The North Fiji Passage, was also originally thought to export Lau Basin waters to the North Fiji Basin. Though this is accurate it is not all. Due to evidence of a deep inflow in both traditional hydrographic data and the Argo profile data, the North Fiji Passage is also a supplier of deep water to the Lau Basin from the north. This northern source has markers of the North Fiji Basin water as well as the Samoan Passage water. Another source into the Lau Basin of these deep waters is through a minimally mentioned area attached to the Vitiaz Trench; the Tofua Passage. The role of the Tonga Passage is not as large as the float data originally suggested. The sill depth of the Tonga Passage is too shallow to allow

the Antarctic origin waters in the DWBC flowing along the Tonga Ridge access to the Lau Basin. Instead its role is to supply the intermediate depth of the Lau Basin.

CHAPTER 5

CONCLUSION AND FUTURE WORK

5.1 Circulation and Sources

Circulation in the South Pacific, historically has relied on large spatial averages. This is mainly due to the large spatial expanse of the Pacific Ocean coupled with limited cohesive traditional observational data. The introduction of autonomous instrumentation, including Argo floats, has been a boon to the study of subsurface circulation globally as well as locally in the South Pacific. Global participation and coverage projects (WOCE, CLIVAR, GoSHIP), have also aided in adding more data points in the sparse coverage in the South Pacific of traditional ship-board hydrographic data.

Using these datasets together yields an alteration to our understanding of the circulation around the Lau Basin and Havre Trough. Previously, the ridge systems framing these two sub-basins was thought to block communication between the east and west South Pacific. Float data however indicated that this was not the case. In fact, floats showed a clear and persistent deep western boundary current (DWBC) that flowed along the Lau and Colville Ridges. Two westward flowing jet-like structures feed the DWBC through breaks in the Tonga and Kermadec Ridges. Within the Havre Trough, from the jet that originates from the Kermadec Passage, a flow bifurcation occurs along the Colville Ridge, leading to a portion of flow being directed south and exiting into the South Fiji Basin while the rest of the flow turns north to join the northward flowing DWBC. The northward flowing DWBC exits the Lau Basin into the North Fiji Basin through the North Fiji Passage.

An extension to the Stommel-Arons (1958) abyssal circulation model, proposed by Pedlosky (1994), predicts the location and existence of the flow bifurcation in the float data. The model was a simple, analytical model with a homogenous layer and straight vertical

walls based on the barotropic vorticity equation. Though the model captured the major features present in the observations, the effects of topography could not be completely ignored. Using a numerical model, with an idealized topographic skirt, though still homogenous layer barotropic vorticity model, refined the flow to include the topographic control observed in the outflow regions along the Lau and Colville Ridges.

Traditional hydrographic data supports the DWBC observed in the float data and expands the depth to which the DWBC occurs. Through occupations of the P31 and P21 lines, a thin (50km wide) but clear northward flowing DWBC is observed. This DWBC appears to exist from 1000m to the bottom of the basin. P06, which runs through the southernmost point of the Havre Trough indicates a strong and deep (below 2000m) northward flowing current, indicating as well a deep passage on the Colville Ridge.

Using hydographic data from CTDs and floats, the sources of water into the Havre Trough supported Wyrtki's (1961) supposition of deep water from the South Fiji Basin flowing east. It is assumed that deep water enters the Havre Trough through the deep passage on the Colville Ridge. Intermediate waters enter the Trough through the Kermadec Passage, forming the jet observed in the float data. A mixture of these two waters is what ends up exiting the Colville Passage back into the South Fiji Basin. Sources into the Lau Basin are slightly more complicated, water properties in the outflowing North Fiji Passage indicate colder and fresher water than the intermediate water the Tonga Passage permitted into the basin. Ship-board hydrographic data indicated an area of inflow along P31, northeast of the main outflow, connecting the Lau Basin to the Vitiaz Tranch and further north.

5.2 Future Work

The original intention of the Ridge 2000 floats was to investigate the flow modification by hydrothermally driven effects. Since the Lau Basin is rife with hydrothermal vents, in some estimates 100's per km (the highest density in the world), it is suspected that heat driven flow would have some effect on the behavior of the flow in the area at least locally.

Originally, a portion of this project was proposed to pursue the affect of hydrothermal vents on the flow. This is still a question to be addressed.

The numerical model used in Chapter 3, used idealized topography, inflow streamlines, and a flat bottom. Refinements to the numerical model to include more realistic topography as well as an idealized stratification are in the design stage to further investigate the dynamic similarity argument.

A beginning analysis of LADCP data (by Andreas Thurnherr) along P06 during the most recent occupation (2017), indicated significantly elevated vertical kinetic energy in the Havre Trough as compared to the South Fiji Basin or the Kermadec Trench. This signal persisted across the Kermadec Ridge and could be having an effect on the DWBC transporting deep water north.

APPENDIX A

C_{DRAG}, JET VELOCITY, AND RIDGE HEIGHT VARIATIONS

A.1 C_{drag}

Following are the variations in the drag term with constant initial jet velocity and Ridge Height.

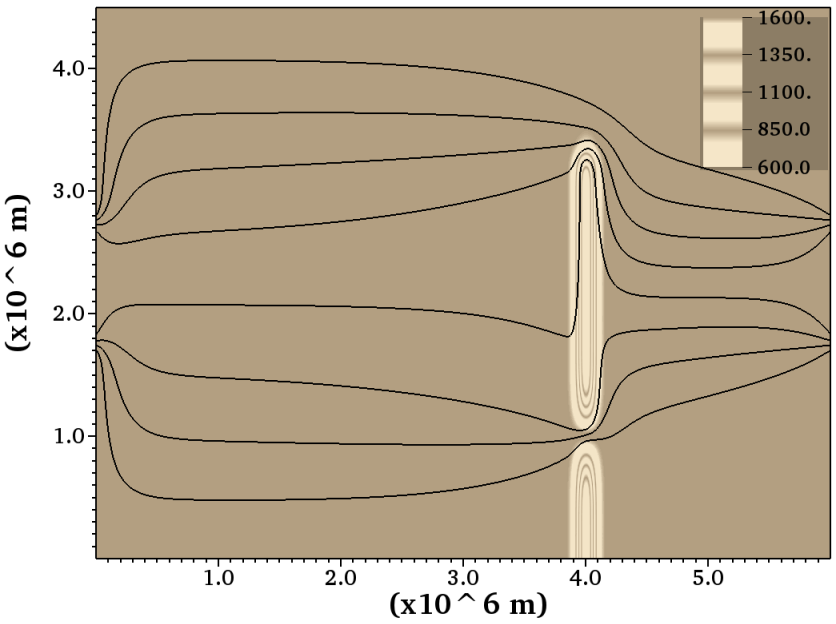

Figure A.1: $C_{drag} = 1 * 10^{-9}$

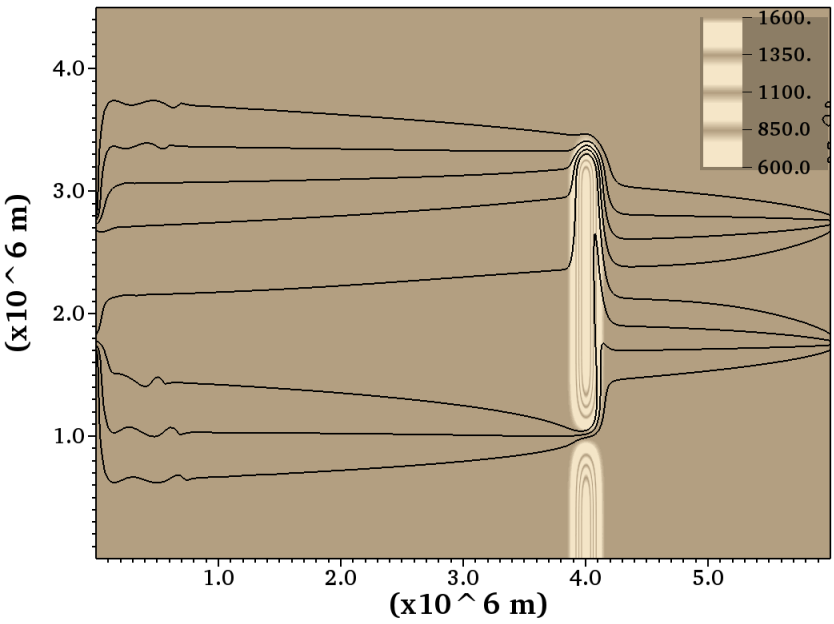

Figure A.2: $C_{drag} = 0.25 * 10^{-9}$

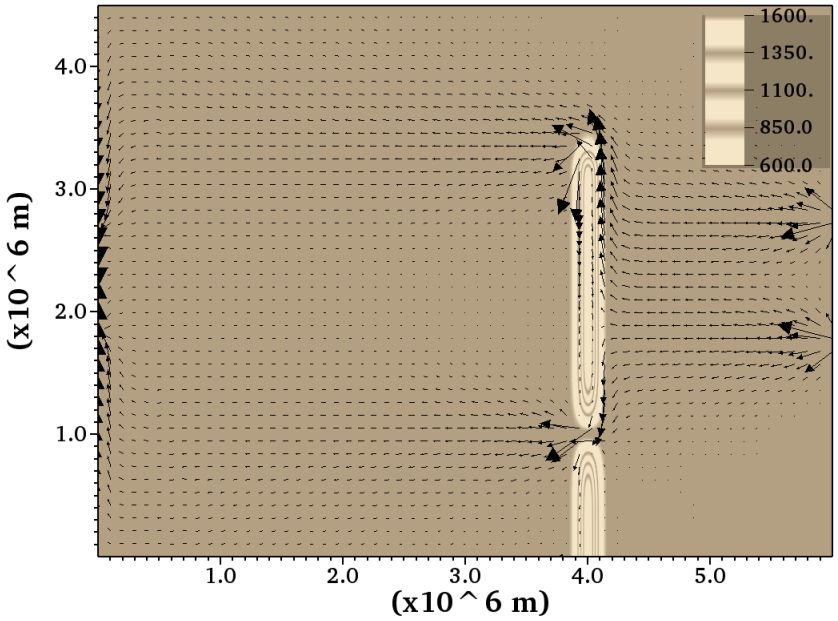

Figure A.3: Jet initial velocity: 0.4 m/s

A.2 Initial Jet Velocity

Following are the variations in the initial jet velocities with constant drag and ridge height. Plots are presented with velocity vectors instead of streamlines to illustrate the varying jet strengths.

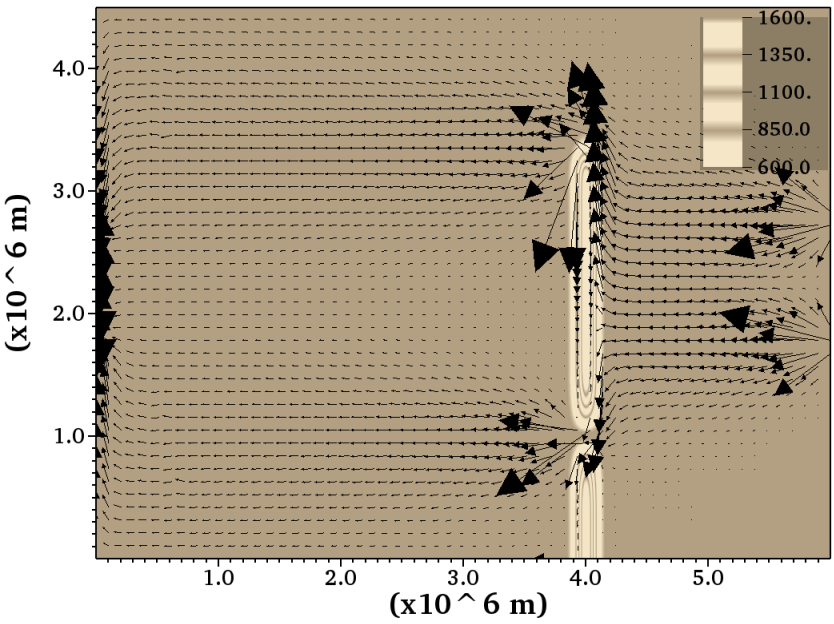

Figure A.4: Jet initial velocity: 0.8m/s

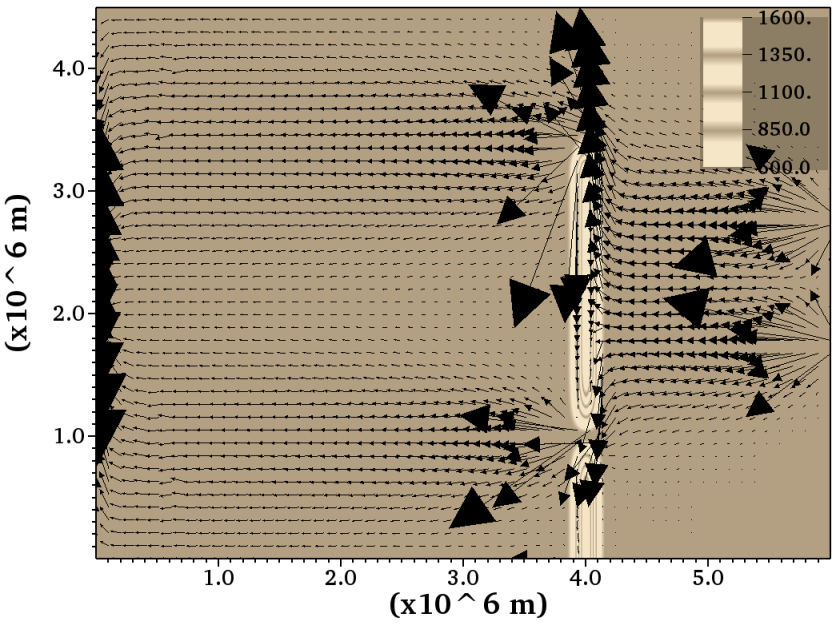

Figure A.5: Jet initial velocity: 1.2 m/s

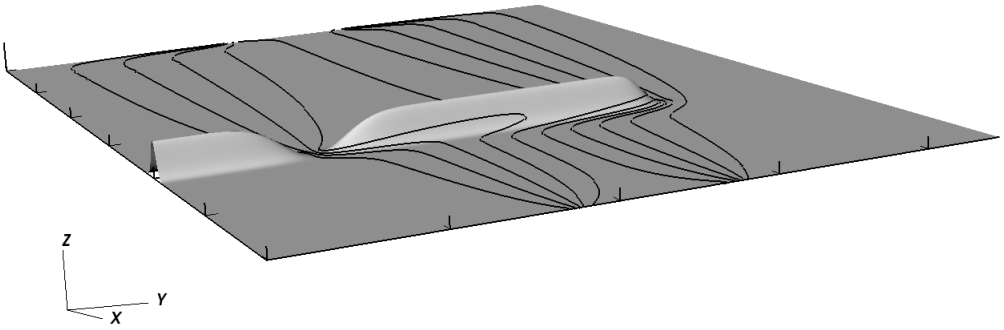

Figure A.6: $\triangle H = 900$m

A.3 Ridge Height

Following are the variations in ridge height that were not presented in the main body of the document. The drag and initial jet velocity remain constant through each ridge height change.

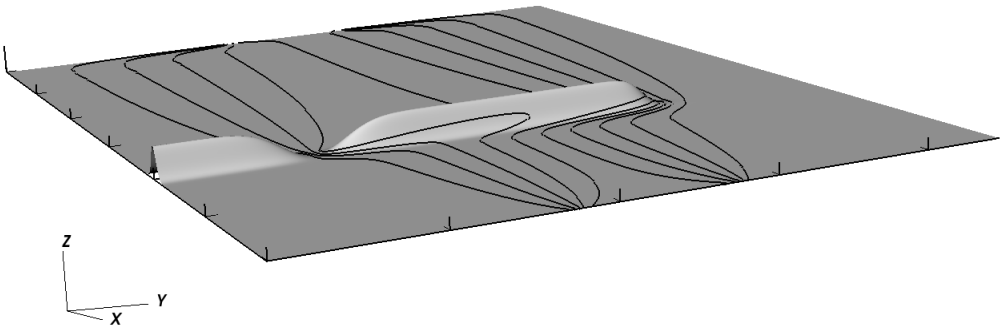

Figure A.7: $\triangle H = 800$m

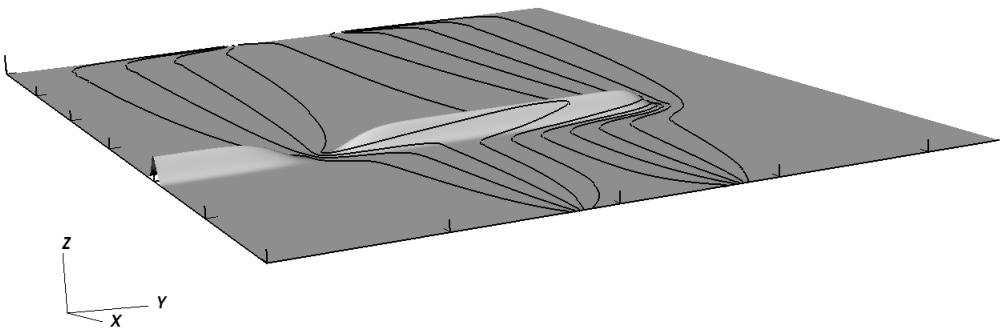

Figure A.8: $\triangle H = 600$m

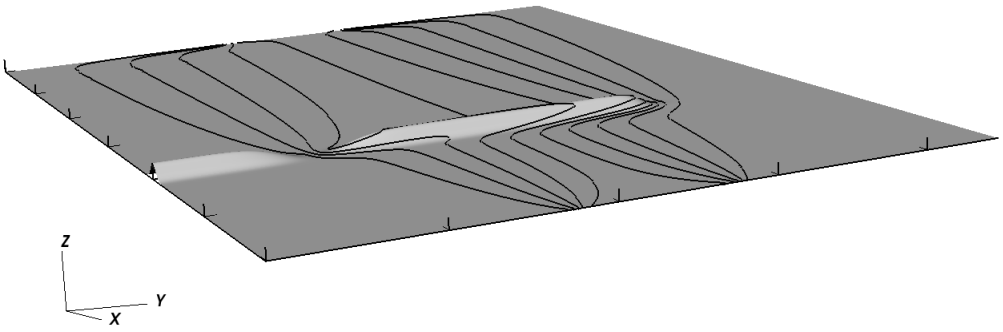

Figure A.9: $\triangle H = 400$m

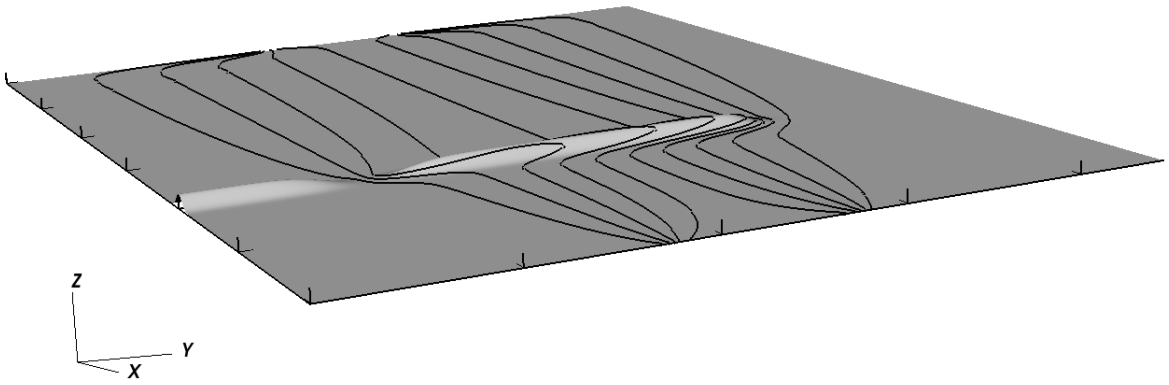

Figure A.10: $\triangle H = 300$, flow overcomes topographic blocking

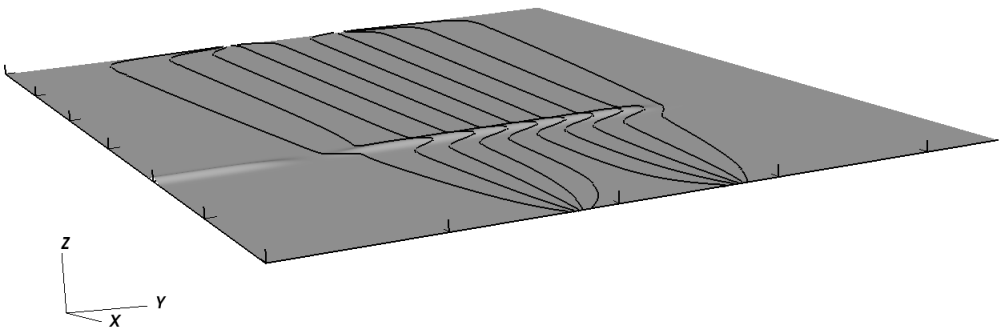

Figure A.11: $\triangle H = 100$m

APPENDIX B

DYNAMIC SIMILARITY DERIVATION

Starting with linear, hydrostatic, Boussinesq equations:

$$u_t - fv = -\frac{1}{\rho_0} p_x \tag{B.1a}$$

$$v_t + fu = -\frac{1}{\rho_0} p_y \tag{B.1b}$$

$$p_z = -g\rho \tag{B.1c}$$

$$w = -\frac{\rho_t}{\rho_z} \tag{B.1d}$$

$$u_x + v_y + w_z = 0 \tag{B.1e}$$

From the hydrostatic equation we can write the density equation in terms of pressure:

$$w = -\frac{p_{zt}}{\rho N^2} \tag{B.2}$$

where N is the Brunt-Vaisala frequency, ρ is the density, p is the pressure, u is the velocity in the zonal direction, v is the velocity in the meridional direction, w is the vertical velocity, g is gravity, and f is the Coriolis parameter.

Non-dimensionalizing these equations gives us:

$$\frac{\mathcal{U}}{T}\vec{u}_t + \mathcal{U} f_0 (1 + \frac{\beta L_y}{f_0} y)\hat{z} \times \vec{u} = -(\frac{\Pi}{L\rho})\nabla P \tag{B.3a}$$

$$\frac{\mathcal{U}}{L_x} u_x + \frac{\mathcal{V}}{L_y} v_y + \frac{\mathcal{W}}{H} = 0 \tag{B.3b}$$

$$\mathcal{W} w = -\mathcal{U}\delta\vec{u} \circ \nabla h \tag{B.3c}$$

$$\mathcal{W} w = -\frac{\Pi}{HT\rho N_{ref}^2} \frac{p_{zt}}{\rho N^2} \tag{B.3d}$$

Where δ is the scale for topographic gradients, not necessarily H/L and N_{ref} is the scale for the Brunt-Vaisala frequency.

Several assumptions need to be made to maintain the simplicity of this progression. The first

is in regards to scaling the horizontal motion. Does $\mathcal{U} \sim \mathcal{V}$? The second, does $L_x \sim L_y$? Are the timescales in the problem longer than the inertial time scale (ie, f)? In other words is it a low Rossby number problem? Lastly does the β-effect matter; $\epsilon_\beta = \frac{\beta L_y}{f_0} > 1$? In order, yes horizontal velocity scales are similar, yes length scales are similar (not depth scales though), and yes we want to focus on a low Rossby number problem.

Dividing equation 8a by $\mathcal{U} f_0$ we get;

$$\epsilon \vec{u}_t + (1 + \epsilon_\beta y)\hat{z} \times \vec{u} = -(\frac{Pi}{L\rho f_0 \mathcal{U}})\nabla p \tag{B.4}$$

We require that $\frac{\Pi}{L\rho f_0 \mathcal{U}} \sim \mathbb{O}(1)$ which leads to the pressure scaling resembling:

$$\Pi = \rho \mathcal{U} f_0 L \tag{B.5}$$

Which is a pressure scale in terms of lateral momentum viscosity.

Scaling of the continuity eqn leads to a scaling relationship for w of $w = \mathcal{U}H/L$ and for the no-normal flow requirement w scales as $w = \mathcal{U}\delta$ and for the buoyancy-hydrostatic eqn we have another scaling of w, $w \sim -\frac{\Pi}{HT\rho N^2_{ref}}$. So the question arises, what is the appropriate scaling for w?

Defining the scaling terms:

$$\epsilon = \frac{1}{f_0 T} \tag{B.6a}$$

$$T = \frac{1}{f_0 \epsilon} \tag{B.6b}$$

$$w \approx \frac{\mathcal{U} f_0^2 \epsilon L}{H N^2_{ref}} \tag{B.6c}$$

Which dictates that the vertical velocity scale is set by stratification. Recall that the Burger number is represented by $S = NH/fL$.

Pursuing the possible solutions for the interior the set of coupled equations in the horizontal momentumis:

$$u_t - fv = -p_x/\bar{\rho} \tag{B.7a}$$

$$v_t + fu = -p_y/\bar{\rho} \tag{B.7b}$$

Combining the hydrostatic equationn ($p_z = \rho' g$) with the original buoyancy equation gets;

$$w = -\frac{p_{zt}}{\rho N^2} \tag{B.8}$$

We want to decouple the momentum eqns. To do this we take $\frac{\partial}{\partial t}$ of both 18a and 18b.

$$u_{tt} - f v_t = -\frac{p_{xt}}{\rho} \tag{B.9a}$$

$$v_t = -\frac{p_y}{\rho} - fu \tag{B.9b}$$

$$u_{tt} - f(-\frac{-p_y}{\rho} - fu) = -\frac{p_{xt}}{\rho} \tag{B.9c}$$

$$\tag{B.9d}$$

The meridional momentum eqn takes a similar form leaving us with:

$$u_{tt} + f^2 u = -\frac{p_{xt}}{\rho} - \frac{f p_y}{\rho} \tag{B.10a}$$

$$v_{tt} + f^2 v = -\frac{p_{yt}}{\rho} + \frac{f p_x}{\rho} \tag{B.10b}$$

We also want to decouple w within the continuity equation;

$$u_x + v_y + w_z = 0 \tag{B.11}$$

knowing that $w = -p_{zt}/\rho N^2$, we can take $\partial/\partial x$ of 21a and add it to $\partial/\partial y$ of 21b:

$$(\frac{\partial^2}{\partial t^2} + f^2)(u_x + v_y) = \frac{1}{\rho}(p_{xxt} - p_{yyt}) \tag{B.12a}$$

$$w_z = -(\frac{p_{zt}}{\rho N^2})_z \tag{B.12b}$$

$$(\frac{\partial^2}{\partial t^2} + f^2)(\frac{p_{zt}}{\rho N^2})_z = \frac{1}{\rho}(-p_{xxt} - p_{yyt}) \tag{B.12c}$$

We can decouple space from time (look at haberman) but we can't decouple (x,y,z) from each other. This is the condition that allows the waves to be topographically trapped. If we assume:

$$\rho \quad = \rho_0 + \bar{\rho}(z) \tag{B.13}$$

$$= \rho_0(1 + \tfrac{\bar{\rho}}{\rho_0}) \tag{B.14}$$

$$\approx \rho_0 + \mathbb{O}(\tfrac{\bar{\rho}}{\rho_0}) \tag{B.15}$$

So to $\mathbb{O}(\frac{\bar{\rho}}{\rho_0})$

$$\frac{1}{\rho}(\frac{\partial^2}{\partial t^2}+f^2)(\frac{p_z}{N^2})_{zt}=-\frac{1}{\rho}(p_{xx}+p_{yy})_t \tag{B.16}$$

So then:

$$p_{xx}+p_{yy}+(\frac{\partial^2}{\partial t^2}+f^2)(\frac{p_z}{N^2})_z=0 \tag{B.17}$$

Recall that $w=-\frac{p_{zt}}{\rho N^2}$ and that on the bottom (against topography) $-\frac{p_{zt}}{\rho N^2}=-\vec{u}\cdot\nabla h$. So by definition if p_z is small then w will be small. If there is no vertical structure then $w=0$ by definition which leaves$p_{xx}+p_{yy}=0$. If we non-dimensionalize equation 28:

$$\frac{1}{L^2}(p_{xx}+p_{yy})+f_0^2(\epsilon^2+1)(\frac{1}{H^2N^2})(\frac{p_z}{N^2})_z=0 \tag{B.18}$$

Divide through by $1/L^2$:

$$(p_{xx}+p_{yy})+(\frac{f_0^2L^2}{H^2N^2})(\epsilon^2+1)(\frac{p_z}{N^2})_z=0 \tag{B.19}$$

$$(p_{xx}+p_{yy})+(\frac{1}{S})^2(\epsilon^2+1)(\frac{p_z}{N^2})_z=0 \tag{B.20}$$

$$S\equiv\frac{HN}{f_0L}\ \textit{Burger number} \tag{B.21}$$

If the Burger number is large, $S>>1$, then the vertical structure is suppressed, as S$\rightarrow\infty$, $p_{xx}+p_{yy}=0$.

The interior dynamics suggest that, when H is a depth scale (for the particular region), L is the scale of the basin or currents within, and S$>>1$, we tend to have little to no vertical structure away from topographic boundaries. The question arises though, what about the flow near topography? What we are really interested in is the set of solutions this can take along a boundary, rather than within an interior.

On $z=-h(x)$, $w=-uh_x$ and recall:

$$w=-\frac{p_{zt}}{\rho N^2} \tag{B.22}$$

and that under low Rossby number:

$$f^2u=-\frac{p_{xt}}{\rho}-\frac{fp_y}{\rho}+\epsilon \tag{B.23}$$

So then:

$$u = -\frac{1}{f^2}\frac{p_{xt}}{\rho} - \frac{p_y}{f\rho} + \mathbb{O}(\epsilon) \tag{B.24}$$

$$w = [\frac{1}{f^2}\frac{p_{xt}}{\rho} + \frac{p_y}{f\rho}]h_x + \mathbb{O}(\epsilon) \tag{B.25}$$

$$-\frac{p_{zt}}{N^2} = [\frac{1}{f^2}p_{xt} + \frac{p_y}{f}]h_x \tag{B.26}$$

Non-dimensionalizing:

$$\frac{1}{HT}\frac{p_{zt}}{N_{ref}^2} = [\frac{1}{f^2}\frac{1}{LT}(p_{xt}) + \frac{1}{fL}p_y]h_x \tag{B.27}$$

$$\frac{f\epsilon}{H}\frac{p_{zt}}{N_{ref}^2} = [\frac{\epsilon}{fL}p_{xt} + \frac{1}{fL}p_y]h_x \tag{B.28}$$

$$= \frac{1}{fL}(\epsilon p_{xt} + p_y)h_x \tag{B.29}$$

$$p_{zt} = \frac{N^2 h_x H}{f^2 L\epsilon}(\epsilon p_{xt} + p_y) \tag{B.30}$$

$$\tag{B.31}$$

If we multiply both sides of equation 41 by H/L:

$$p_{zt} = S^2(\frac{h_x}{\frac{H}{L}})(\frac{1}{\epsilon}) \tag{B.32}$$

$$= (\frac{S^2\delta}{\epsilon})(\epsilon p_{xt} + p_y) \tag{B.33}$$

Where δ is the ratio between the topographic slope: h_x and the total aspect ratio for the entire basin: H/L. If $\epsilon << 1$, then $p_{zt} = \frac{S^2\delta}{\epsilon}p_y$. So along the boundary:

$$w = -uh_x \tag{B.34}$$

$$w = -\frac{p_{zt}}{\rho N^2} \tag{B.35}$$

$$(\frac{\partial^2}{\partial t^2} + f^2)u = -\frac{p_{xt}}{\rho} - \frac{fp_y}{\rho} \tag{B.36}$$

$$-\frac{p_{zt}}{\rho N^2} = -[\frac{1}{\frac{\partial^2}{\partial t^2} + f^2}(\frac{-p_{xt}}{\rho} - \frac{fp_y}{\rho})]h_x \tag{B.37}$$

If we make an assumption about the solution that P, u, w will take $\sim e^{i\sigma t}$, then:

$$i\sigma\frac{p_z}{N^2} = -(\frac{1}{f^2 - \sigma^2})(i\sigma p_x - fp_y)h_x \tag{B.38}$$

When $\sigma \to 0$ (long timescales), on long time scales the vertical structure is not enforced at the boundary, i.e $p_z = 0$. We can non-dimensionalize:

$$i\sigma(\sigma^2 + f^2)\frac{p_z}{N^2} = (i\sigma p_x - f p_y)h_x \tag{B.39}$$

$$\sigma = 1/T\sigma \tag{B.40}$$

$$(i\sigma)(\sigma^2 - f^2)(\frac{1}{HN_{ref}^2})(\frac{p_z}{N^2}) = (i\sigma(1/L)p_x - f/L p_y)h_x \tag{B.41}$$

$$f^2(\frac{1}{HN})i\sigma((\frac{\sigma}{f})^2 - 1)(\frac{p_z}{N^2}) = (f/L)(i(\sigma/f)p_x - p_y)h_x \tag{B.42}$$

$$\tag{B.43}$$

allowing $\omega = \sigma/f$, a non-dimensional frequency

$$\frac{f^2\omega}{HN_{ref}^2} i(\omega^2 - 1)\frac{p_z}{N^2} = \frac{1}{L}(i\omega p_x - p_y)h_x \tag{B.44}$$

$$i\omega(\omega^2 - 1)\frac{p_z}{N^2} = \frac{HN_{ref}^2 h_x}{f^2 L}(i\omega p_x - p_y) \tag{B.45}$$

$$= (\frac{H^2 N_{ref}^2}{f^2 L^2})(\frac{h_x}{\frac{H}{L}}) \tag{B.46}$$

$$i\omega(\omega^2 - 1)(\frac{p_z}{N^2}) = S^2\delta(i\omega p_x - p_y) \tag{B.47}$$

This results in the governing dynmaics for the system, where $S^2\delta$ is known a priori giving a scaling for comparison with the simpler case of straight vertical walls and no stratification.

BIBLIOGRAPHY

[Banks et al., 1995] Banks, H., Bullister, J., Bacon, S., Bryden, H., and Rennell, J. (1995). The deep western boundary current at 17°s in the pacific ocean. In *International WOCE Newsletter*, number 19.

[Boyer et al., 2013] Boyer, T. P., Antonov, J. I., Baranova, O. K., Coleman, C., Garcia, H. E., Grodsky, A., Johnson, D. R., Locarnini, R. A., Mishonov, A. V., Brien, T. D., Paver, C. R., Reagan, J. R., Seidov, D., Smolyar, I. V., Zweng, M. M., and Sullivan, K. D. (2013). *WORLD OCEAN DATABASE 2013*. NOAA Atlas NESDIS 72.

[Chapman and Malanotte-Rizzoli, 1989] Chapman, D. and Malanotte-Rizzoli, P. (1989). Wave motions in the ocean. *Notes*.

[Davis, 2005] Davis, R. E. (2005). Intermediate-Depth Circulation of the Indian and South Pacific Oceans Measured by Autonomous Floats. *Journal of Physical Oceanography*, 35:683–707.

[Fornari et al., 2012] Fornari, D., Beaulieu, S., Holden, J., Mullineaux, L., and Tolstoy, M. (2012). Introduction to the special issue: From RIDGE to Ridge 2000. *Oceanography*, 25(1):12–17.

[Ganachaud et al., 2014] Ganachaud, A., Cravatte, S., Melet, A., Schiller, A., Holbrook, N., Sloyan, B., Widlansky, M., and Bowen, M. (2014). The Southwest Pacific Ocean circulation and climate experiment (SPICE). *JGR:Oceans*.

[Gill, 1976] Gill, J. B. (1976). Compostion and age of the Lau Basin and Ridge Volcanic Rocks: Implications for Evolution of an Inter-arc Basin and Remnant Arc. *GSA Bulletin*, 87(10):1384–1395.

[Godfrey, 1989] Godfrey, J. (1989). A sverdrup model of the depth-integrated flow for the world ocean allowing for island circulations. *Geophysical and Astrophysical Fluid Dynamics*, 45:89–112.

[Gray and Riser, 2014] Gray, A. R. and Riser, S. C. (2014). A global analysis of sverdrup balance using absolute geostrophic velocities from argo. *Journal of Physical Oceanography*, 44:1213–1229.

[Ichikawa et al., 2001] Ichikawa, Y., Takatsuki, Y., Mizuno, K., Shikama, N., and Takeuchi, K. (2001). Estimation of Drifting Velocity and Error at Parking Depth for the Argo Float. *JAMSTECR*, 44:81–89.

[Katsumata and Yoshinari, 2010] Katsumata, K. and Yoshinari, H. (2010). Uncertainties in Gloabal Mapping of Argo Drift Data at the Parking Level. *Journal of Oceanography*, 66:553–569.

[Kopriva, 2009] Kopriva, D. (2009). *Implenting Spectral Methods for Partial Differential Equations*. Springer Netherlands.

[Lebdev et al., 2007] Lebdev, K. V., Yoshinari, H., Maximenko, N. A., and Hacker, P. W. (2007). YoMaHa'07: Velocity data assesed from trajectories of Argo floats at paarking level and at the sea surface. *IPRC*, (4(2)).

[Murata and Uchida, 2009] Murata, A. and Uchida, H. (2009). *Cruise Report: P21*. JAMSTEC.

[Oka, 2005] Oka, E. (2005). Long-term Sensor Drift Found in Recovered Argo Profiling Floats. *Journal of Oceanography*, 61:775–781.

[Ollitrault and Rannou, 2013] Ollitrault, M. and Rannou, J.-P. (2013). ANDRO: An Argo-Based Deep Displacement Dataset. *Journal of Atmospheric and Oceanic Technology*, 30:759–788.

[Park et al., 2005] Park, J., Kim, K., King, B., and Riser, S. (2005). An Advanced Method to Estimate Deep Currents from Profiling Floats. *Journal of Atmospheric and Oceanic Technology*, 22:1294–1304.

[Pedlosky, 1994] Pedlosky, J. (1994). Ridges and Recirculations: Gaps and Jets*. *Journal of Physical Oceanography*, 24:2703–2707.

[Pedlosky, 1996] Pedlosky, J. (1996). *Ocean Circulation Theory*.

[Pedlosky et al., 2009] Pedlosky, J., Iacono, R., Napolitano, E., and Helfrich, K. (2009). The Skirted Island: The Effect of Topography on the Flow Around Planetary Scale Islands. *Journal of Marine Research*, 67:435–478.

[Reid et al., 1968] Reid, J., Stommel, H., Stroup, E. D., and Warren, B. A. (1968). Detection of a deep boundary current in the western south pacific. *Nature*.

[Reid, 1986] Reid, J. L. (1986). On the total geostrophic circulation of the South Pacific Ocean: flow patterns, tracers, and transports. *Progress in Oceanography*, 16:1–61.

[Rhines, 1970] Rhines, P. (1970). Edge-, bottom-, and rossby waves in a rotating stratified fluid. *Geophysical Fluid Dynamics*.

[Roemmich et al., 1996] Roemmich, D., Hautala, S., and Rudnick, D. (1996). Northward abyssal transport through the Samoan passage and adjacent regions. *Journal of Geophysical Research C: Oceans*, 101(C6):14039–14055.

[Schoonover, 2018] Schoonover, J. (2018). A Geostrophic Barotropic Vorticity Solver (GeoBarS). https://schoonovernumerics.github.io/GeoBarS/.

[Schoonover et al., 2015] Schoonover, J., Zamora, Y., and Estrada, J. (2015). *Spectral Elements Library in Fortran: Technical Documentation*.

[Speer and Thurnherr, 2012] Speer, K. and Thurnherr, A. (2012). The Lau Basin Float Experiment (LAUBFLEX). *Oceanography*, 35(1):284 –285.

[Stommel et al., 1958] Stommel, H., Arons, A. B., and Faller, A. J. (1958). Some Examples of Stationary Planetary Flow Patterns in Bounded Basins. *Tellus*, 10(2):179–187.

[Sutton et al., 2012] Sutton, P., Chiswell, S., Gorman, R., Kennan, S., and Rickard, G. (2012). Physical marine environment of the Kermadec Islands regions. *Science for Conservation*, 318:1–16.

[Tivey et al., 2012] Tivey, M., Becker, E., Beinart, R., Fisher, C., Girguis, P., Langmuir, C., Michael, P., and Reysenbach, A.-L. (2012). Links from Mantle to Microbe at the Lau Integrated Study Site: In-sights from a Back-arc Spreading Center. *Oceanography*, 25(1):62–77.

[Warren, 1976] Warren, B. A. (1976). Structure of Deep Western Boundary Currents. *Deep Sea Research and Oceanographic Abstracts*, 23(2):129–142.

[Warren et al., 1994] Warren, B. A., Whitworth III, T., Moore, M. I., and Nowlin Jr., W. D. (1994). Slight Northwestward Inflow to the Deep South Fiji Basin. *Deep-Sea Research*, 41(5/6):953–956.

[Whitworth III et al., 1999] Whitworth III, T., Warren, B. A., Nowlin Jr, W. D., Rutz, S. B., Pillsbury, R. D., Moore, M. I., Nowlin, Jr, W., Rutz, S. B., Pillsbury, R. D., and Moore, M. I. (1999). On the deep western-boundary current in the Southwest Pacific Basin. *Progress in Oceanography*, 43(1):1–54.

[Wyrtki, 1961] Wyrtki, K. (1961). The Flow of Water into the Deep Sea Basins of the Western South Pacific Ocean. *Australian Journal of Marine and Freshwater Research*, 12(1):1–16.

BIOGRAPHICAL SKETCH

Elizabeth G. Simons

Education

Florida State University Ph.D., Geophysical Fluid Dynamics, Spring 2018

- Dissertation Topic: Circulation in the Lau Basin and Havre Trough
- Advisor: Kevin Speer, P.D

Florida State University B.S., Applied and Computational Mathematics, Spring 2011

Research Experience

Cruises

- CLIVAR/CO2 Repeat Hydrographic Line A10 (2011). At sea 36 days, Ronald H. Brown. CTD watch stander, primary LADCP operator.
- PE12-26 CTD and Mooring recovery (2012). At sea 4 days, The Pelican. CTD operations and Mooring Recovery.
- JR286 Bottom Drifter Deployment (2012/2013). At sea 10 days in transit to Antarctica, James Clark Ross. Testing and release of new equipment. In collaboration with the British Antarctic Survey (BAS).
- CLIVAR/CO2 Repeat Hydrographic Line P16S (2014). At sea 46 days, Nathaniel B. Palmer. CTD watch stander, primary on WDP drifter releases.
- GO-SHIP Repeat Hydrographic Line P06, leg 2 (2017). At sea 42 days, Nathaniel B. Palmer. Primary LADCP operator, primary on WDP drifters and Argo float releases.

Field Work

Apalachicola field campaign to study the physical processes effecting phytoplankton growth. Planned, organized and participated several short field experiments.

Research Fellow

Student Research Fellow, Los Alamos National Laboratory, 2016-2017

Submitted Journal Publications

E.G. Simons, K.G. Speer, A. Thurnherr (2017). Abyssal Circulation in the Lau Basin and Havre Trough. (Submitted to Journal of Marine Research)

Papers in Preperation

Geyer, N., E.G. Simons, T. B. Kelly, D. Balwada (2018). Physical processes affecting phytoplankton growth and distribution in Apalachicola Bay, Florida.

Simons, E. G., N. Geyer, K. Khazmutdinova (2018). A descriptive note on hydrographic changes in Alligator Harbor over the last 50 years.

Simons, E.G., J. Schoonover, K.G. Speer (2018). Topographic Effects in the Lau Basin and Havre Trough.

Simons, E.G., K.G. Speer (2018). Lau Basin and Havre Trough Connections to South Pacific Sub-basins.

Presentations

Talks

Simons, E.G, KG Speer, A Thurnherr, Abyssal Circulation in the Lau Basin and Havre Trough, Ocean Sciences Meeting, 2018

Simons E.G., An Overview of Observational Oceanography, LANL, 2017

Simons, E.G., A Brief Observational Occupation of Apalachicola Bay, Fl, LANL, 2016

Simons, E.G., Importance of the Gulf of Mexico in Relation to Larger Basins, Shipboard P16S, 2014

Simons, E.G. and K.G. Speer, Mixing Across Topography; Results from GLAD and SCULP, GOMRI 5minute lectures, 2013

Posters

Simons, E.G, and K.G. Speer, Abyssal Circulaiton in the Lau Basin, AGU annual meeting 2016

Simons, E.G., and KG Speer, Abyssal Circulation in Protected Lau Basin, LANL Student Sympossium (2016)

Simons, E. G. and K.G. Speer, Western Boundary Currents in the Lau Basin, Ocean Sciences (2016)

Simons, E.G. and K.G. Speer, Mixing in the Northern Gulf of Mexico, Gulf of Mexico Research Initiative (2014)

Simons, E.G., K.G. Speer, C. Hancock, N. Wienders, RAFOS Float Release in the Gulf of Mexico, Deep-C Meeting (2013)

Simons, E.G., K.G. Speer, C. Hancock, N. Wienders, RAFOS Float Release in the Gulf of Mexico, Gulf of Mexico Research Initiative (2012)

Smith, C., E.G. Simons, E. Mortenson, N. Wienders, K.G. Speer, Hydrographic Survey of the Southern Boundary of Apalachicola Bay, Gulf of Mexico Research Initiative (2011)

Public Outreach

Simons, E.G., Life at Sea, Tallahassee Community College, 2017

Simons, E.G., The Oceans, Girls in STEM, LANL, 2016

Simons, E.G., Observational Oceanography!? The What, How, and Why, Waterworks Science Nite, 2015